SIMULATION AND COMPARISON OF VAPOR-COMPRESSION DRIVEN, LIQUID- AND AIR-COUPLED COOLING SYSTEMS

A Thesis
Presented to
The Academic Faculty

by

Daniel Lee Golden

In Partial Fulfillment
of the Requirements for the Degree
Masters of Science in the
School of Mechanical Engineering

Georgia Institute of Technology
December 2010

SIMULATION AND COMPARISON OF VAPOR-COMPRESSION DRIVEN, LIQUID- AND AIR-COUPLED COOLING SYSTEMS

Approved by:

Dr. Srinivas Garimella, Advisor
School of Mechanical Engineering
Georgia Institute of Technology

Dr. Sheldon Jeter
School of Mechanical Engineering
Georgia Institute of Technology

Dr. J. Rhett Mayor
School of Mechanical Engineering
Georgia Institute of Technology

Date Approved: July 2010

ACKNOWLEDGEMENTS

I would like to thank the members of the Sustainable Thermal Systems Laboratory at the Georgia Institute of Technology for their ready assistance and encouragement. I would especially like to thank Mr. Brian Fronk for sharing insight and assistance in my review process. I am deeply grateful to Dr. Srinivas Garimella, my advisor, for his guidance, insight, and patience, and for providing some eye-opening opportunities. Lastly, I would like to thank my family for their support and encouragement, especially my brother Ensign James Golden.

TABLE OF CONTENTS

LIST OF TABLES

Page

LIST OF FIGURES

Page

LIST OF SYMBOLS

Symbols

A	area (m^2, mm^2)
B_B	Butterworth (1975) coefficient
C	thermal capacitance (W/K, kW/K), dimensionless number
c	center dimension (m, mm)
Cp	specific heat (kJ/kg-K)
Cr	coefficient of thermal capacitances
CAT	closest approach temperature (°C)
COP	coefficient of performance
D	diameter (m, mm)
f	friction factor, fin dimension (m, mm)
G	mass flux (kg/m^2-s)
h	enthalpy (kJ/kg), heat transfer coefficient (W/m2-K), height (m, mm)
j	Colburn factor
k	thermal conductivity (kW/m-K)
L	length (m, mm)
l	louver dimension (m, mm)
$LMTD$	log mean temperature difference (°)
m	mass (kg), dimensionless number
$\dot{m}$	mass flow rate (kg/s)
N	number
n	dimensionless number
NTU	number of transfer units

Nu	Nusselt number
P	pressure (kPa, Pa)
Pr	Prandtl number
Q	heat rate (kW)
q''	heat flux (W/m-, kW/m^2)
Re	Reynolds number
s	entropy (kJ/kg-K)
T	temperature (°C)
t	thickness, or other tube dimension (m)
U	overall heat transfer coefficient (W/m^2-K, kW/m^2-K)
V	velocity (m/s), volume (m^3, mm^3)
$\dot{V}$	volumetric flow rate (m^3/s)
W	power (kW)
w	width (m)
X	Martinelli parameter
x	hydronic fluid concentration (%), quality

Greek Symbols

α	void fraction, aspect ratio
Δ	amount of change
ε	effectiveness, relative roughness
η	efficiency
θ	angle (°)
μ	viscosity (kg/m-s)
ρ	density (kg/m^3)
φ	two-phase multiplier

ω	humidity ratio

Subscripts

Accel	acceleration
air	air
avg	average
boiling	boiling
c	cross-sectional, critical
CBD	convective boiling dominated
circ	circular
comp	compressor
cond	condensation, conduction
conv	convection, convective
core	pertaining to the heat exchanger core
d	direct, dead space
Darcy	Darcy friction factor
eff	effective
Fanning	Fanning friction factor
fin	fin
fric	frictional
h	height
HX	heat exchanger
i	inner, in
id	indirect
insul	insulation
l	liquid, louver

le, lo	referring to liquid only
liq., liquid	liquid
max	maximum
min	minimum
NBD	nucleate boiling dominated
nat	natural convection
o	outer, out
p	port, pitch
rad	radiation
refg	refrigerant
s	isentropic, swept
sat	saturation conditions
seg	segment
surr	surroundings
t	thickness, tube
total	total
v	vapor
w	width
web	strengthening web

SUMMARY

Industrial and military vehicles, including trucks, tanks and others, employ cooling systems that address passenger cooling and auxiliary cooling loads ranging from a few Watts to 50 kW or more. Such systems are typically powered using vapor-compression cooling systems that either directly supply cold air to the various locations, or cool an intermediate single-phase coolant closed loop, which in turn serves as the coolant for the passenger cabins and auxiliary loads such as electronics modules. Efforts are underway to enhance the performance of such systems, and also to develop more light weight and compact systems that would remove high heat fluxes. The distributed cooling configuration offers the advantage of a smaller refrigerant system package. The heat transfer between the intermediate fluid and air or with the auxiliary heat loads can be fine tuned through the control of flow rates and component sizes and controls to maintain tight tolerances on the cooling performance. Because of the additional loop involved in such a configuration, there is a temperature penalty between the refrigerant and the ultimate heat sink or source, but in some configurations, this may be counteracted through judicious design of the phase change-to-liquid coupled heat exchangers. Such heat exchangers are inherently smaller due to the high heat transfer coefficients in phase change and single-phase liquid flow compared to air flow. The additional loop also requires a pump to circulate the fluid, which adds pumping power requirements. However, a direct refrigerant-to-heat load coupling system might in fact be suboptimal if the heat loads are distributed across large distances. This is because of the significantly higher pressure drops (and saturation temperature drops) incurred in transporting vapor or two-phase fluids through refrigerant lines across long plumbing elements. An optimal

system can be developed for any candidate application by assessing the tradeoffs in cooling capacity, heat exchanger sizes and configurations, and compression, pumping and fan power. In this study, a versatile simulation platform for a wide variety of direct and indirectly coupled cooling systems was developed to enable comparison of different component geometries and system configurations based on operating requirements and applicable design constraints. Components are modeled at increasing levels of complexity ranging from specified closest approach temperatures for key components to models based on detailed heat transfer and pressure drop models. These components of varying complexity can be incorporated into the system model as desired and trade-off analyses on system configurations performed. Employing this platform as a screening, comparison, and optimization tool, a number of conventional vapor-compression and distributed cooling systems were analyzed to determine the efficacy of the distributed cooling scheme in mobile cooling applications. Four systems serving approximately a 6 kW cooling duty, two with air-coupled evaporators and two with liquid-coupled evaporators, were analyzed for ambient conditions of 37.78°C and 40% relative humidity. Though the condensers and evaporators are smaller in liquid-coupled systems, the total mass of the heat exchangers in the liquid-coupled systems is larger due to the additional air-to-liquid heat exchangers that the configuration requires. Additionally, for the cooling applications considered, the additional compressor power necessitated by the liquid-coupled configuration and the additional power consumed by the liquid-loop pumps result in the coefficient of performance being lower for liquid-coupled systems than for air-coupled systems. However, the use of liquid-coupling in a system does meet

the primary goal of decreasing the system refrigerant inventory by enabling the use of smaller condensers and evaporators and by eliminating long refrigerant carrying hoses.

CHAPTER 1

INTRODUCTION

1.1. Background

Large vehicles, including tanks and trucks, require passenger cooling and auxiliary cooling loads ranging from a few Watts to 50 kW or more. These cooling loads are typically satisfied using a vapor compression system which is either directly coupled to the compartment air or to a secondary coolant loop, which is then coupled to the passenger cabin or other auxiliary loads. Efforts are underway to enhance the performance of such systems, and also to develop more light-weight and compact systems that would remove high heat fluxes. The distributed cooling configuration is one possible way to meet these goals.

Distributed thermal management systems are capable of using a single central plant coupled to a single-phase fluid in a closed secondary loop to provide heating or cooling when there are multiple, spatially separate heating or cooling requirements. Water and hydronic fluid mixtures are widely used as heat transfer fluids in the secondary loop. Examples of distributed thermal systems include district heating systems that meet industrial and residential heating requirements by providing steam or hot water to multiple buildings and hydronic residential heating systems that provide steam or hot water from a central boiler to individual room heater units in a single-family residence. The use of hydronic coupling has also been investigated for use in residential heat pumps (Jiang 2001). Additionally, distributed chilled water systems are often used for cooling coils in central air handling units, process applications, and systems where hot water,

steam, or electric sources are used for heating. Data centers are also increasingly considering distributed liquid based cooling systems to provide essential, high performance electronics cooling. A distributed cooling configuration built around a core vapor compression system could provide an optimum thermal management system to meet the multiple, distributed cooling requirements of large vehicles with several subsystems located throughout the engine compartment, cabin, and storage space.

Distributed cooling systems offer the advantage of a smaller refrigerant system package. Conventional automotive vapor-compression systems transfer heat directly between an air stream and the refrigerant, necessitating the use of a cross-flow heat exchanger. Due to the low air-side heat transfer coefficient, the thermal resistance of the air-side dominates the substantially lower refrigerant-side resistance. This mismatch limits heat exchanger design, leading to larger heat exchangers that do not fully take advantage of the high heat transfer coefficients associated with phase-change processes. In a distributed cooling configuration, the refrigerant exchanges heat with the hydronic fluid mixture in a counter-flow manner with comparable heat transfer coefficients and hydraulic diameters. The higher heat transfer coefficients in both fluids allow the heat exchanger size to be much smaller for a given heat duty. The smaller size allows for greater flexibility in location of the refrigerant subsystem within the vehicle. Additionally, the heat transfer between the intermediate fluid and air or with the auxiliary heat loads can be maintained within close tolerances through control of coolant flow rates and accurate component modeling and design. A distributed cooling configuration with a centralized refrigerant system core can be designed to have less refrigerant tubing, reducing pressure losses and the associated drop in saturation temperature, leading to

higher system efficiency and more economically sized heat exchangers. Additionally, as shown by Jiang (2001), a hydronically coupled system can reduce the refrigerant charge, which is of increasing importance as the contribution of synthetic refrigerant to global warming and ozone depletion comes under greater scrutiny. In the event that the thermal management system was required to operate in heating mode as well as cooling mode, a hydronically coupled system can be switched more easily than a conventional vapor-compression system. The hydronically coupled system merely requires the switching of hydronic fluid valves to switch the hot and cold sides of the system, resulting in a less complicated and more reliable system.

Consider a conventional vehicular air conditioning system for comparison with the distributed cooling configuration. The conventional vehicular air conditioning system consists of a vapor-compression cooling system with an air-coupled condenser, an air-coupled evaporator, an expansion device, and a compressor. Figure 1 is a schematic of a system designed to provide passenger space cooling. The state points described here correspond to the system schematic in Figure 1 and the system pressure-enthalpy diagram in Figure 2. The representative system under consideration has a cooling duty of 6 kW with an evaporator volumetric air flow rate of 0.1416 m^3/s (300 cfm) and ambient conditions of 37.78°C (100°F) and 40% relative humidity. Beginning at the evaporator inlet, state point 1, the refrigerant is a two-phase vapor-liquid mixture. With an air delivery temperature of 15.05°C (59.1°F) and assuming a closest approach temperature of 4°C, the refrigerant saturation temperature is 11.05°C (51.9°F). For R-134a, this requires a saturation pressure of 429.7 kPa (62.32 psi). The refrigerant is vaporized and then superheated through the evaporator, exiting as a superheated vapor at state 2. Cooling the

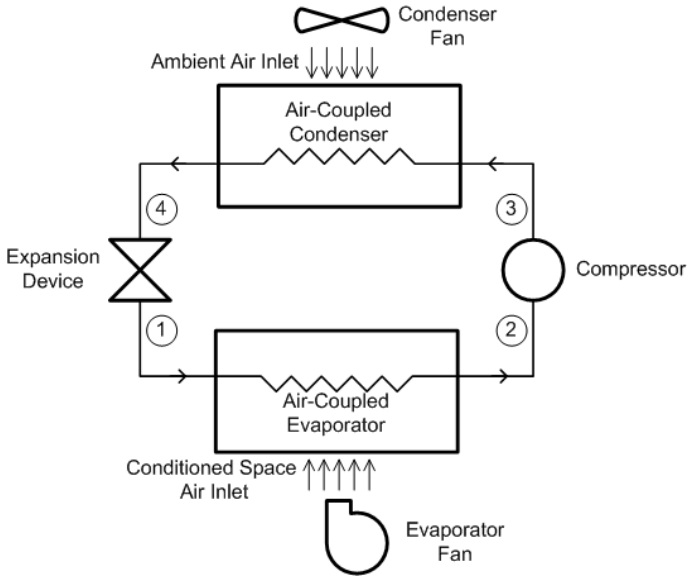

Figure 1: Schematic of a Conventional Vapor-Compression System

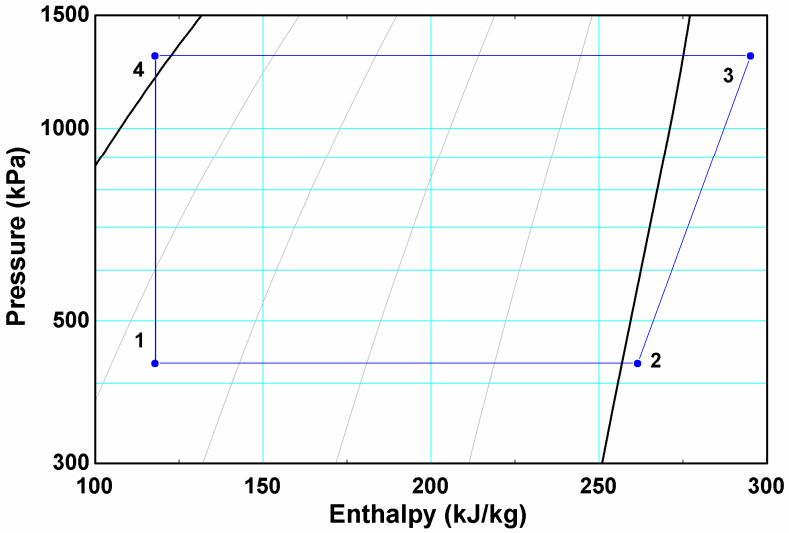

Figure 2: p-h Diagram for a Conventional Vapor-Compression System

air stream to 15.05°C results in dehumidification to a relative humidity of 100%, and a humidity ratio of 0.01069. After the refrigerant exits the evaporator, it enters the compressor. From state point 2 to 3, work is added to the system, increasing the

refrigerant pressure and temperature. To ensure that heat is rejected from the refrigerant to the condenser-side air stream, the refrigerant saturation temperature corresponding to the compressor discharge pressure must be higher than the highest air temperature in the condenser. The average air outlet-temperature for a representative 0.8495 m^3/s (1800 cfm) condenser-side air stream is 45.38°C (113.7°F); assuming a closest approach temperature of 4°C, the refrigerant saturation temperature must be 49.38°C (120.9°F). For refrigerant R-134a, the saturation pressure at 49.38°C (120.9°F) is 1298 kPa (188.3 psi). After exiting the compressor, the superheated vapor refrigerant enters the condenser, where the refrigerant rejects heat directly to the coupled ambient air stream. The refrigerant transitions from a superheated vapor to a saturated vapor, saturated liquid, and sub-cooled liquid, progressively. At the same time, the temperature of the ambient air stream increases as it gains energy from the condensing refrigerant. After the refrigerant exits the condenser at state point 4, the pressure is reduced through the expansion device to the evaporator saturated pressure, thus completing the cycle.

For comparison, a representative distributed cooling system is discussed here. The distributed cooling configuration consists of a vapor-compression core coupled to the conditioned space and the ambient environment via liquid loops. One possible system design is shown in Figure 3. It consists of a liquid-coupled condenser, liquid-coupled evaporator, expansion device, compressor, two liquid-air heat exchangers, and two liquid loop pumps. A vehicular distributed cooling system could have an air- or liquid-coupled condenser; the common characteristic of the distributed cycles investigated here is the presence of the liquid-coupled evaporator and its corresponding coolant loop. The state points described here correspond to the system illustrated in Figure 3 and the pressure-

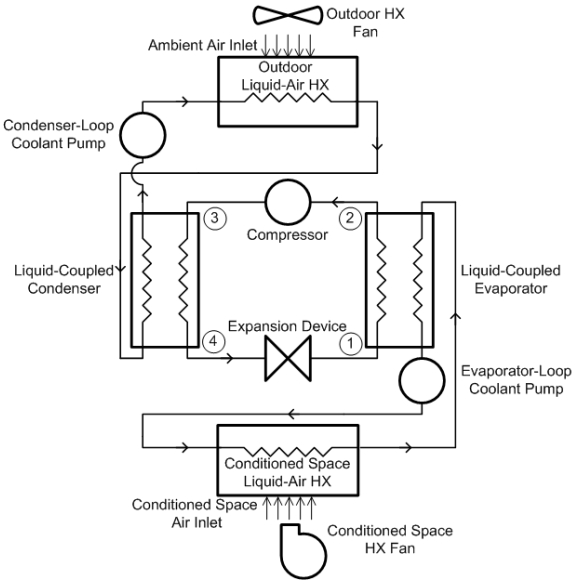

Figure 3: Schematic of a Simple Distributed Cooling System

enthalpy diagram in Figure 4. Refrigerant enters the evaporator at state point 1 as a two-phase vapor-liquid mixture. Heat is transferred from the evaporator-side liquid loop to the refrigerant across the liquid-coupled evaporator; decreasing the temperature of the coupling fluid and superheating the refrigerant. The refrigerant exit from the evaporator, state point 2, also corresponds to the refrigerant inlet to the compressor. The compression process of the refrigerant in the vapor-compression core of the distributed cooling system is the same as the process described above for the air-coupled vapor compression system. The refrigerant exits the compressor at state point 3 as a high pressure superheated vapor before it enters the liquid-coupled condenser. In the liquid-coupled condenser, heat is transferred to the coupling fluid until the refrigerant exits at a sub-cooled state. The temperature of the condenser-side liquid increases as it gains the heat rejected by the refrigerant. Downstream of the condenser exit, state point 4, the refrigerant pressure is reduced through an expansion device, completing the refrigerant

loop. Coupling liquid exits the evaporator and enters the conditioned space liquid-air heat exchanger. In this heat exchanger, the conditioned space air stream transfers heat to the low temperature liquid, reducing the air stream temperature while increasing the liquid temperature. After flowing through the evaporator-side liquid-loop pump, the liquid returns to the evaporator. The condenser-side liquid exiting the condenser flows through the liquid-air heat exchanger, where heat is rejected to the environment. The fluid then is pumped back to the condenser.

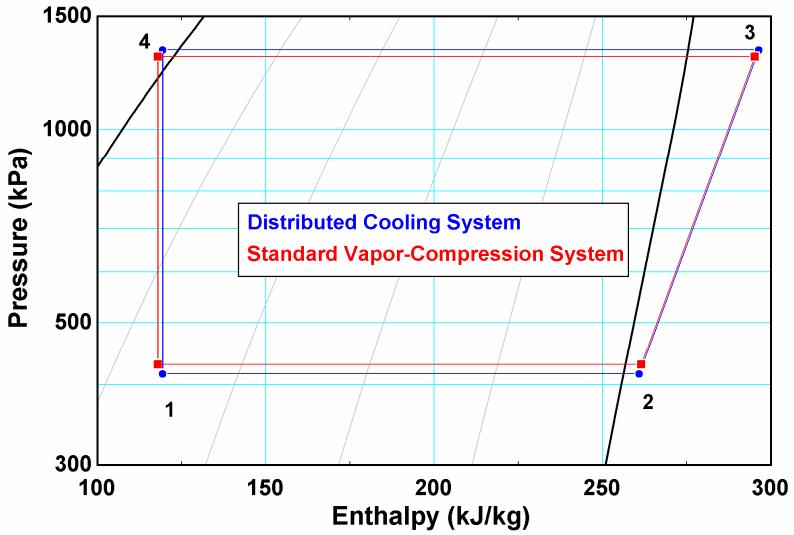

Figure 4: p-h Diagram for a Simple Distributed Cooling System

There must be a temperature difference between two fluids for heat transfer to occur. Due to the intermediate liquid loops in the distributed cooling system configuration, one must carefully consider the required temperature differences between any given fluid pair. The required temperature difference is represented by a specified closest approach temperature (*CAT*) between the coupled fluids. For the baseline air-coupled system, a *CAT* of 4°C between the refrigerant and air was assumed for most

cases. For the distributed cooling configuration, there are now two *CAT*s required on each side of the system: one between the air and the coupling fluid and one between the coupling fluid and the refrigerant. For many of the cases studied in this investigation, the air-liquid *CAT* was specified to be 3°C and the liquid-refrigerant *CAT* was specified to be 2°C. It should be noted that the *CAT*s in the two heat exchange processes represent a stack up in the required temperature difference between the refrigerant and the air. A lower *CAT* was chosen for the coupling fluid-refrigerant heat exchangers because of the lower thermal resistances anticipated in liquid-coupled heat exchange compared to air-coupled heat exchange.

This temperature penalty between the refrigerant and the ultimate heat sink or source may be compensated for through judicious design of the phase change-to-liquid coupled heat exchangers. Such heat exchangers are inherently smaller due to the high heat transfer coefficients in phase change and single-phase liquid flow compared to air flow. As noted, the additional loop also requires a pump to circulate the coolant, which adds pumping power requirements. However, a direct refrigerant-to-heat load coupling system might in fact be suboptimal if the heat loads are distributed across large distances. This is because of the significantly higher pressure drops (and saturation temperature drops) incurred in transporting vapor or two-phase fluid through refrigerant lines across long plumbing elements, which may increase the compressor power requirements and heat exchanger size.

1.2. Scope of Research

To assess tradeoffs between potential system designs in cooling capacity, heat exchanger sizes, system complexity, and compression, pumping and fan power, a

versatile simulation platform is necessary so that optimal cooling systems can be developed for each candidate application. This simulation methodology must provide a consistent framework for the performance evaluation of systems of different capacities, while also providing a screening tool for the quick selection of the most optimal system configuration for each application. The availability of such a platform will assist in the long-term implementation of modular, scalable components and systems for a wide range of cooling capacities. A simulation platform that addresses these needs was developed in this work.

The system simulation model was developed using *Engineering Equation Solver* software (Klein 2009). The central subsystem in the model is a vapor-compression system that is coupled to either air or a secondary fluid as the heat source and sink. The cycle thermodynamics are captured by modeling the evaporation, compression, condensation, and expansion processes. Several different source and sink coupling options are investigated so that tradeoff analyses between different candidate configurations can be made on the basis of heat exchanger surface area requirements, compressor and other auxiliary power, and ease of installation. The flexible modeling framework is such that either built-in, simple reduced-order models of heat exchangers, or detailed heat exchanger models developed elsewhere can be incorporated into the overall system-level simulation framework. The details of this model are described below.

The major components modeled include air-coupled condensers and evaporators, liquid-coupled condensers and evaporators, secondary fluid-to-air heat exchangers, and liquid-to-liquid heat exchangers. These heat exchangers are initially modeled using

closest approach temperatures (*CAT*) specifications to achieve model closure. The corresponding component models in varying degree of detail are designed to be integrated into the overall system in such a way that incorporation of detailed or simple component models into the overall system only requires changing a few call statements. Similarly, using simple assumptions about the physical geometry of the fluid passages, representative heat transfer coefficients for different fluids can be determined with the appropriate correlations and combined into the respective overall heat transfer coefficients to supplement the *CAT*-based models, with the resulting surface area estimates used for component and system configuration selection.

In addition to the major heat exchange components, models for minor components such as liquid, vapor and two-phase refrigerant lines, secondary fluid lines, and air ducts were also developed. The line and duct models account for the heat loss or gain due to exposure to the ambient environment through convective and radiative modes and for fluid pressure drop as a function of line length and diameter. In the case of the two-phase refrigerant, the saturation temperature drop due to pressure drop is also calculated.

Compressors, pumps, and fans are modeled using isentropic efficiency specifications. While enabling reasonable estimates of system performance, these specifications also serve as simplified representations of more complex models based on performance curves that may be incorporated by a user, if such information is available through tests or vendor specifications. Implementation of such more detailed models would only require a simple exchange of a few lines of *EES* code already provided in commented (inactivated) form in the present versions of the programs. More detailed descriptions of

the component models and of methods for integrating these components into a system are provided in subsequent chapters.

The system models developed may be used to conduct parametric analyses of system performance as a function of component sizes, plumbing diameters and lengths, compressor type, and other component specifications. The effects of plumbing bends and fittings can be determined if a detailed system orientation within a vehicle structure is known; however, these aspects are not considered in this study. Parametric analyses of the variation in performance with ambient operating conditions and desired cooling conditions may also be conducted. Most importantly, the effect of coupling to heat sinks/sources using closed-loop liquid coupling or air coupling can be studied before significant investment is made into detailed system and component design. Thus, several configurations that prove sub-optimal may be eliminated readily, and the preferred configuration for a particular application under consideration may be identified with little initial effort.

To illustrate the utility of the models developed here, different representative distributed cooling systems for large vehicular application were evaluated and compared with corresponding air-coupled options. System modeling results were used in conjunction with individual component models to yield component designs, which will be described in more detail in a subsequent chapter. System performance was evaluated on the basis of a range of operating conditions including ambient temperature, conditioned space air delivery temperature, and cooled liquid delivery temperature. System performance was also studied over a range of system configurations with

variation of such parameters as the distance of a rear cooling zone from a front cooling zone.

1.3. Thesis Organization

The remainder of this thesis is organized as follows:

- Chapter 2 reviews prior work relevant to the study of distributed cooling systems.
- Chapter 3 describes the models that were developed for the heat exchangers, compressor, pump, fan, and minor components.
- Chapter 4 presents and compares several specific cases that were investigated including parametric analyses for a representative air-coupled and a representative liquid-coupled system across a range of operating parameters.
- Chapter 5 provides a summary of the conclusions obtained from this study, and recommendations for future research.

CHAPTER 2

LITERATURE REVIEW

This chapter provides a review of existing literature on the design and modeling of vehicular cooling systems, with an emphasis on the vapor-compression system, particularly those with hydronic fluid coupling.

2.1. Vehicular Cooling Systems

2.1.1. Alternate Cooling Technologies

Some of the earliest approaches to cooling the storage compartments of large delivery trucks used blocks of ice (Birch 1995). Heat from the storage compartment was transferred to the phase change material as it melted. The evaporative cooler was used in the 1950s (Birch 1995) for passenger cooling. It achieved cooling by taking advantage of the latent heat of vaporization of water. A mist of water was blown through the passenger compartment and evaporated as heat transferred from the passengers to the water. This design, while simple, is only effective in drier climates where relative humidity is low. In the 1970s, an innovative compressed air system, the Rovac system, sought to take advantage of the decrease in temperature that accompanies a decrease in fluid pressure (Birch 1995). Air was drawn into the vehicle through fans, compressed, cooled and then rapidly expanded, removing heat as it flowed through the passenger compartment.

2.1.2. Automotive Vapor-Compression Systems

Today, vapor compression systems are the most common systems for vehicular cooling. As previously described, such a system consists of an evaporator to remove heat from the conditioned space air stream, a compressor to elevate the pressure and temperature of the working fluid, a condenser to reject heat to the ambient environment, and an expansion device to reduce the pressure and temperature of the working fluid to prepare it to take on more heat from the conditioned space. Air flow through the evaporator and into the passenger cabin or conditioned space is powered by a blower. Air flow across the condenser is either due to ram air as a result of the forward motion of the vehicle or is powered by a cooling fan, which draws the same air stream across the engine coolant heat exchanger of the vehicle.

Improvements in automotive air-conditioning systems have primarily resulted from incremental advances in component design and manufacture, and control schemes, rather than fundamental changes to the refrigeration cycle employed. Advanced heat exchangers, such as flat-tube/multi-louvered fin with mini- or micro-channels, are lighter, smaller, and require less refrigerant (Jiang 2001). Compressors have become lighter, more efficient, and quieter (Birch 1995). Advanced compressor designs allowing for variable displacement, including wobble-plate type, vane type, and scroll type compressors (Birch 1995) further increase performance. Improvements in the control of the automotive air-conditioning system allow it to be more efficient. Instead of setting the evaporator pressure to deliver 0°C air and then reheating the air to reach the desired temperature, one could allow the evaporator pressure to vary to directly deliver the desired air temperature. This would avoid unnecessary compressor power consumption

and improve cycle efficiency (Eilemann and Kampf 2001). Additionally, the use of electronic or thermostatic expansion valves instead of orifice tubes allows for more accurate matching between the vapor compression cycle and required cooling (Lou 2005).

2.2. Hydronic Fluid/Distributed Thermal Management Systems

Hansen (1985) defines a hydronic system as any in which the heat carrier, or working fluid, is neither consumed nor rejected after use but rather re-circulated in a loop. A hydronic system does not create a cooling or heating effect; it merely transports heat from a source to a sink. Hydronic systems are not a new concept; the ancient Romans made use of hydronic heating systems with copper boilers and coils (Hansen 1985). Modern applications include district heating, district cooling, heat storage, and cogeneration. Hydronic systems are also readily found in vehicles. In fact, the conventional engine coolant system, which uses a water/ glycol mixture as the transport fluid, is perhaps the most common hydronic system in use.

The concept of the distributed cooling system is an extension of the basic hydronic system. Chilled water systems, which provide low temperature water for cooling at discrete, separated locations, are an example of a distributed cooling system. Jiang (2001) investigated the suitability and impact of hydronic coupling in a residential heat pump system. An analytical model to predict the performance of a system with a core vapor compression cycle hydronically coupled at the condenser and evaporator was developed. In air conditioning mode, the cold hydronic loop was coupled to the conditioned space and the hot loop to the ambient, with the reverse true for heat pump operation. Performance of the hydronic system was compared with a conventional air-

coupled heat pump system. Both systems were designed for the same heating and cooling loads, 15.05 kW and 10.56 kW, respectively. It was found that total heat exchanger material volume required for the condenser and evaporator was much lower for the hydronically coupled system. However, the total material volume was slightly higher due to the two extra liquid-to-air heat exchangers. The total refrigerant charge required for the hydronically coupled system was less than 10% of the total refrigerant charge required for the conventional system. This can be attributed to the smaller liquid-refrigerant heat exchangers and the absence of long refrigerant carrying lines normally found in an air-coupled system.

Rogstam and Mingrino (2003) developed and tested a coolant-based automotive heat pump system. They claim that higher efficiency engines do not produce enough waste heat for use in heating the passenger compartment in cold weather conditions. They sought to decrease the warm-up time by using the engine coolant as a ready heat source by modifying the standard automotive air-conditioning system. Their solution essentially reversed the basic automotive vapor compression system and replaced the conventional condenser with an engine-coolant/refrigerant heat exchanger. This would be analogous to a liquid-coupled evaporator/air-coupled condenser distributed cooling system, except that the engine is being cooled instead of a passenger compartment. Unfortunately, there is little description of the system modeling used to develop this system.

Another example of the use of liquid-coupling in an automotive application is given by Kampf and Schmadl (2001). In addressing the need to keep truck cabins cool when stopped without idling the engine, they developed a thermal storage system which

is essentially a distributed cooling system with the ability to readily switch heat sinks. Figure 5 shows the basic system that they developed. It is readily noticeable that their system consists of an air-coupled condenser, compressor, and a liquid coupled evaporator. The liquid loop can be routed to either the cooling battery, which is a phase-change material, or to the cabin air-coupled heat exchanger, or both. The solution they suggest to the cabin cooling problem is that the cooling battery could be 'generated' while the truck engine is running and the vapor-compression system is operational. When the truck engine is shut off, the vapor compression system is shut off, and the coolant is redirected so that there is a loop between the cooling battery and the cabin heat exchanger. Liquid coupling enables the operation of this unique system. Conceptually, this system is identical to one where there are multiple heat loads that are cooled by a single coolant secondary loop.

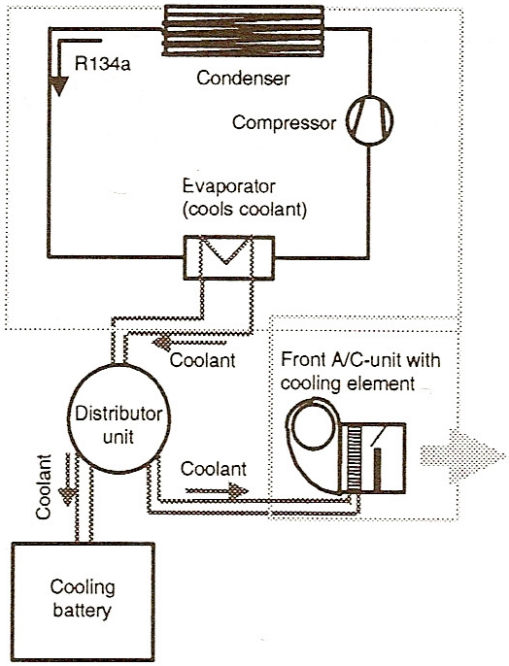

Figure 5: Cooling Battery System, from Kampf and Schmadl (2001)

2.3. Component Modeling

2.3.1. Heat Exchanger Modeling

Accurately predicting heat exchanger performance with varying inlet conditions is critical for a thermal management system model. One of the most common methods to model heat exchangers is to sub-divide the heat exchanger into a number of smaller control volumes or segments (Garimella and Wicht 1995; Rahman *et al.* 2003; Lou 2005; Schwentker *et al.* 2006). These segments may span many parallel tubes and extend a certain, predetermined length (Garimella and Wicht 1995; Lou 2005), represent an entire tube pass (Rahman *et al.* 2003); or each tube may be segmented with the results of each segment leading into the next (Schwentker *et al.* 2006). In their system model, Rahman e*t al*. (2003) represented the heat exchangers as bare tubes with empirical correction factors for length and surface area. They also employed a series of "Shape Factors" to calibrate the results of their system model with the data from their experimental setup.

Alternatively, the segment heat duty may be modeled in a more realistic manner by considering the actual heat exchanger geometries and properties of both fluid flows. Garimella and Wicht (1995) and Schwentker *et al.* (2006) do this by using specifically identified heat transfer and friction factor correlations to calculate refrigerant-side and air-side heat transfer and pressure drop. Both of these studies develop a thermal resistance network for each segment to determine a local value of *UA*, which is then used in the ε-*NTU* method to calculate fluid outlet conditions and the heat transferred in each segment. A model may employ many segments to represent variations in fluid properties (Garimella and Wicht 1995), as in a phase-change process, or there may be fewer segments, as in a single-phase heat transfer fluid where there is not much variation in

fluid properties (Rahman *et al.* 2003). For models that consider condensing or evaporator flows, it is important to capture the transition between single phase and saturated conditions at a segment level. Some models determine the exact location of the saturated-liquid or saturated-vapor by continually checking for saturation conditions and altering the segment length as needed (Garimella and Wicht 1995). Others simply maintain predetermined segment lengths and perform calculations based upon average quality (Lou 2005). The use of fewer segments may be justified to reduce computation time in a system model; however, a large number of smaller segments may be required for detailed component design (Garimella and Wicht 1995; Lou 2005).

2.3.1.1 Refrigerant Heat Transfer Coefficient and Pressure Drop

Refrigerant heat transfer coefficient and pressure drop are important parameters in any reasonably detailed heat exchanger model. The local heat transfer coefficient and pressure drop are highly dependent on fluid properties, fluid flow regime, and the channel geometry. Therefore any reasonable estimation of heat transfer coefficient or friction factor/pressure drop must account for all of these parameters.

Single-phase flow through tubes can generally be characterized as laminar or turbulent. Heat transfer coefficients in single-phase flows are easily calculated from the Nusselt number (Kays *et al.* 2005). For laminar flow, the friction factor is typically a function of Reynolds number only. In most engineering applications, the most common way to predict fluid flow and heat transfer is with empirical and semi-empirical correlations. Churchill's (1977b, a) correlations for friction factor and Nusselt number are popular due to their ease of use and applicability to the laminar, transition, and turbulent regimes.

For flow through non-circular cross sections, solutions of the laminar momentum and energy equations are available, often in tabular or graphical form (Kays *et al.* 2005). Often the hydraulic diameter concept extends well to turbulent flow; however, the simplification breaks down for passages with sharp corners. Many investigators have approached this issue by experimentally determining friction coefficients and heat transfer coefficients for non-circular geometries (Kays *et al.* 2005). Kakac *et al.* (1987) suggest a method to account for rectangular passage that agrees within 1% of the exact relations.

Two-phase heat transfer and pressure drop is of particular interest for vapor compression systems. Condensing or boiling fluids behave much differently than a single-phase liquid or vapor. This is due to the presence of both liquid and vapor in the same flow passage and the dynamics associated with the phase change of the fluid. These dynamics are highly dependent on whether the fluid is boiling or condensing, fluid properties and the geometry of the flow passage.

Early work on saturated flow boiling considered a range of fluids through conventionally sized flow passages with hydraulic diameters from 3 mm and up (Kandlikar 1990). As energy is added to the saturated liquid, the thermodynamic quality increases from 0 to 1. During this progression, a number of distinct flow regimes are observed depending on heat flux, mass flux, quality and fluid properties. In the isolated bubble regime, individual bubbles begin to appear at the tube surface. As bubbles begin to coalesce, they form gas pockets in the predominantly liquid flow: the slug flow regime. The slug flow and the isolated bubble flow represent nucleate boiling (Grosse *et al.* 2006). As the vapor quality continues to increase, wavy, chaotic flows begin to appear,

called churn flow. This can be considered a transition from nucleate boiling to convective dominated boiling. Finally, a transition to annular flow is observed. Convective boiling dominates in the annular flow regime and it is characterized by a liquid layer on the tube wall surrounding a predominately gas flow (Grosse *et al.* 2006). Many researchers have attempted to quantify the impact of flow regime and the relative contributions of nucleate and convective boiling on overall flow boiling heat transfer coefficient. Work is still ongoing in this area, particularly in small channels where surface tension effects become increasingly important. Many empirical and semi-empirical correlations provide satisfactory results for engineering design applications. A discussion of some of the more commonly used correlations follows.

Chen's (1966) widely used correlation accounts for the combined effects of nucleate and convection boiling contributions. The convective boiling contribution is determined from a modification of the Dittus-Boelter equation through the use of an effective two-phase Reynolds number, *F*. The nucleate boiling contribution is calculated from a modification of Forster and Zuber's (1955) correlation for the pool boiling Nusselt number through the use of a bubble suppression factor, *S*. The two-phase Reynolds number *F* is a function of the Martinelli parameter. The bubble suppression factor, *S*, is an empirical function of the two-phase Reynolds number. A generalized form of the correlation is given in Equation 1.1; the full equation may be found in the original paper (Chen 1966). The correlation was compared with experimental results for water and organic fluids and found to be accurate within ± 12%.

$$h = h_{\text{convective}} + h_{\text{nucleate}} \tag{1}$$

Kandlikar (1990) sought to establish a general correlation for saturated flow boiling. He postulated that the heat transfer coefficient would be the maximum of the heat transfer coefficients calculated for the convection boiling dominant and nucleate boiling dominant regimes, both of which accounted for convective boiling and nucleate boiling effects. The basic relationships in the correlation are given in Equation 1.2, and the full correlation may be found in the original paper (Kandlikar 1991). It was reported that of the data points used to develop the correlation, 66% were predicted within ±20 % error, while 86% of the values were predicted within ±30% error. The data on which the correlation is based are for tube diameters ranging from 5 mm to 32 mm and mass fluxes of 15 to 4900 kg/m^2-s. Carey (2008) suggests that, because of relatively good agreement with data for a broad range of fluids, Kandlikar's correlation may be the most reliable general correlation.

$$h_{\text{boiling}} / h_{\text{liquid}} = \text{maximum of} \left\{ \begin{matrix} h_{\text{NBD}} \\ h_{\text{CBD}} \end{matrix} \right\} \tag{2}$$

Shah (1976) proposed a correlation for the heat transfer coefficient as a function of the convection number, the boiling number and Froude number. This correlation is suitable for flow boiling in both vertical and horizontal tubes.

Heat exchangers with smaller hydraulic diameters are receiving increased attention. The flow regimes and transitions differ from those observed in larger channels due to the increased importance of surface tension as hydraulic diameter decreases. This has necessitated the development of heat transfer correlations specifically for mini-channels (Grosse *et al.* 2006). According to Grande and Kandlikar (2003), a mini-channel has a hydraulic diameter between 0.200 mm and 3 mm. At these smaller

hydraulic diameters, surface tension becomes more important, while tube orientation effects from gravity become less significant. According to Grosse *et al.* (2006), it generally appears that nucleate boiling is the dominant mechanism of the heat transfer during boiling in mini-channels and that there is a strong dependence on the heat flux. Qualitatively speaking, when bubbles form in the flow passage, instead of bubbles being intermingled in the passing liquid, they consume the entire flow area; thus leading to a true succession of liquid and vapor. Among other differences, Carey (2008) notes that data show the heat transfer coefficient in mini-/micro-channels decreasing with increasing quality, which is the opposite trend found in conventionally sized tubes.

Yen *et al.* (2003) experimentally studied the saturated flow boiling of R123 and FC72 in 0.19, 0.3, and 0.51 mm inside diameter tubes, at mass fluxes of 50-300 kg/m^2-s. They found that the heat transfer coefficient monotonically decreases with increasing vapor quality, independent of mass flux. The effect of nucleate boiling was found to be dominant, while the convection boiling effect was minor.

Lee and Mudawar (2005) studied the heat transfer characteristics of R-134a in a micro-channel heat sink that was configured as an evaporator in a refrigeration cycle. They measured heat transfer coefficient at heat fluxes from 15.9 to 93.8 W/cm^2, and vapor qualities from 0.26 to 0.87. They found that low heat fluxes produce nucleate boiling at low refrigerant qualities, while high heat fluxes at medium and high qualities are dominated by annular film evaporation. To address these observed trends, they developed a new correlation using data from the literature on water and their own R-134a data with a main dependence on the boiling number, Bo, and the liquid Weber number, We_{fo}. They found that their correlation, when compared with the data, yielded a mean

absolute error of 12.26%, with most of the data falling within ±30%, while exhibiting the expected trends.

To account for the differences in flow regimes and heat transfer mechanisms encountered in mini- and micro-channels, Kandlikar and Balasubramanian (2004) recommended modifications to Kandlikar's (1990) heat transfer coefficient for conventionally sized flow passages. These modifications include changing the liquid-only heat transfer coefficient that is used in the conventional correlations. For the turbulent liquid-only Reynolds numbers, $Re_{lo} > 3000$, the fluid-specific correlating factor is to be taken as unity as the Froude number effect, or the effect of tube orientation, is expected to be negligible due to the increasing importance of surface tension. For the laminar liquid-only Reynolds number, $Re_{lo} < 1600$, it is suggested that the liquid-only heat transfer coefficient be calculated using constant values for the liquid-only Nusselt number with a constant heat flux boundary condition, where the constants vary according to channel cross section for laminar fully developed flow ($C = 4.36$ for round tubes, C varies for rectangular aspect ratios). In the transition range of the liquid-only Reynolds number, $3000 > Re_{lo} > 1600$, they suggest an interpolation between the liquid-only heat transfer coefficient values for the laminar and turbulent regimes of liquid-only Reynolds number. When the liquid-only Reynolds number is below 100, Kandlikar and Balasubramanian argue that since the flow boiling mechanism is dominated by nucleate boiling, the two-phase heat transfer coefficient should be set equal to the heat transfer coefficient for the nucleate-boiling dominated regime.

Figure 6 shows the heat transfer coefficient plotted against refrigerant quality for R-134a using the conventional flow boiling correlations described above. Calculations

are carried out for conditions representative of those encountered in the present study (G = 95 kg/m^2-s, q'' = 10 kW/m^2, T_{sat} = 5°C). In order to determine the applicability of these correlations at representative mini-channel dimensions, the hydraulic diameter was allowed to vary from 1 mm to 0.1 mm. For all values of hydraulic diameter, the calculated heat transfer coefficients were highest for Kandlikar's (1990) correlation and lowest for Chen's (1966) correlation. Shah's (1976) correlation yielded spikes in the heat transfer coefficient at the extremes of refrigerant quality, so these were not plotted for clarity; the spikes in heat transfer coefficient do not agree with other two correlations.

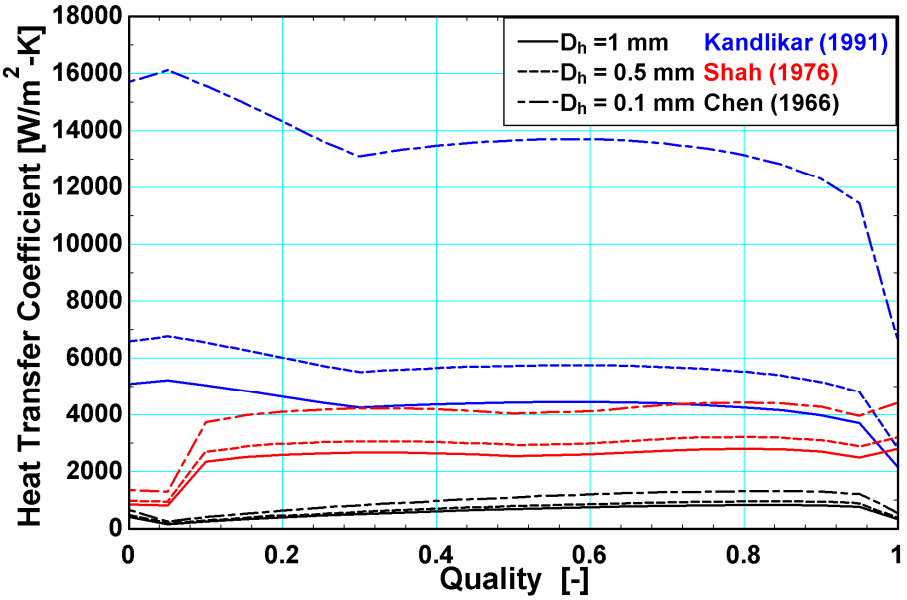

Figure 6: Boiling Heat Transfer Coefficient vs. Refrigerant Quality for Conventional Tube Size Correlations

Figure 7 shows the heat transfer coefficient plotted against refrigerant quality for R-134a and the same conditions as above, using the correlations specifically intended for use with mini- and micro-channel flow passages. At the hydraulic diameters relevant to this study, 1 mm to 0.5 mm, both Lee and Mudawars's (2005) correlation and Kandlikar and Balasubramanian's (2004) correlation yield similar values and trends for heat transfer

coefficient. Like Shah's (1976) correlation, Lee and Mudawar's (2005) correlation yielded unrealistic different spikes in heat transfer coefficient as quality approached zero, while Kandlikar and Balasubramanian's (2004) correlation yielded smoother results. It should be noted that, though most of Lee and Mudawar's (2005) correlation is based upon R-134a and water data (~0.3 < x < 1), only water data was available for the lower quality range due to their experimental setup.

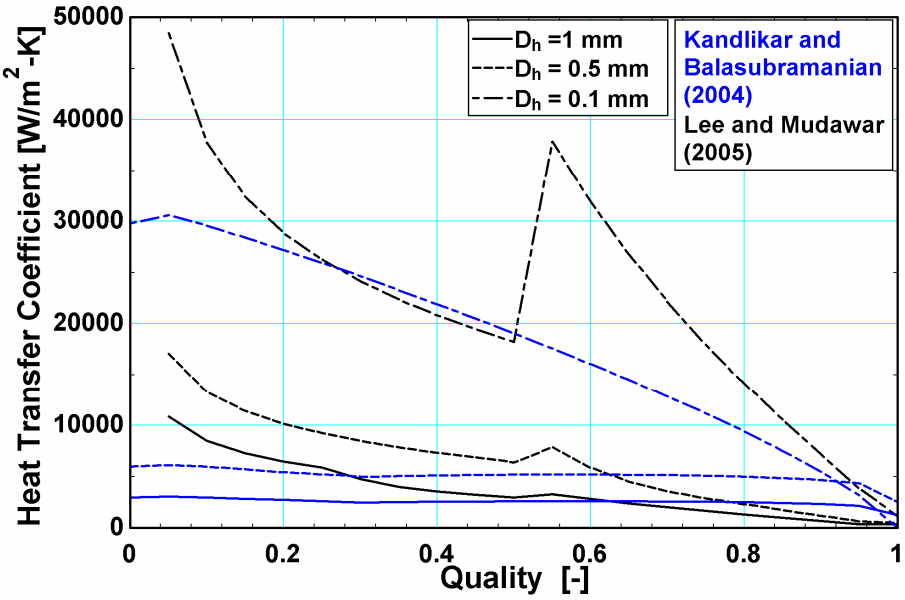

Figure 7: Boiling Heat Transfer Coefficient vs. Refrigerant Quality for Mini-/ Micro-Channel Correlations

Figure 8 shows the heat transfer coefficient plotted against refrigerant quality for R-134a using Kandlikar's (1991) conventional tube size correlation and Kandlikar and Balasubramanian's (2004) mini-/micro-channel correlation. At hydraulic diameters of 1 mm and 0.5 mm, both correlations yield almost identical trends, though the absolute value for the mini-/micro-channel correlation is lower by an average of 41% for the 1 mm diameter and 9.8% for the 0.5 mm diameter. For the 0.1 mm hydraulic diameter, the

value of the conventionally calculated heat transfer coefficient is much higher than for the other diameters, but the general trend is still exhibited. The heat transfer coefficient calculated using the mini-channel correlation exhibits a drastically different trend. At low refrigerant quality the heat transfer coefficient is very large, but it decreases rapidly with increasing quality. This is likely due to the very low calculated vapor Reynolds number, which has a large influence on the correlation at smaller diameters.

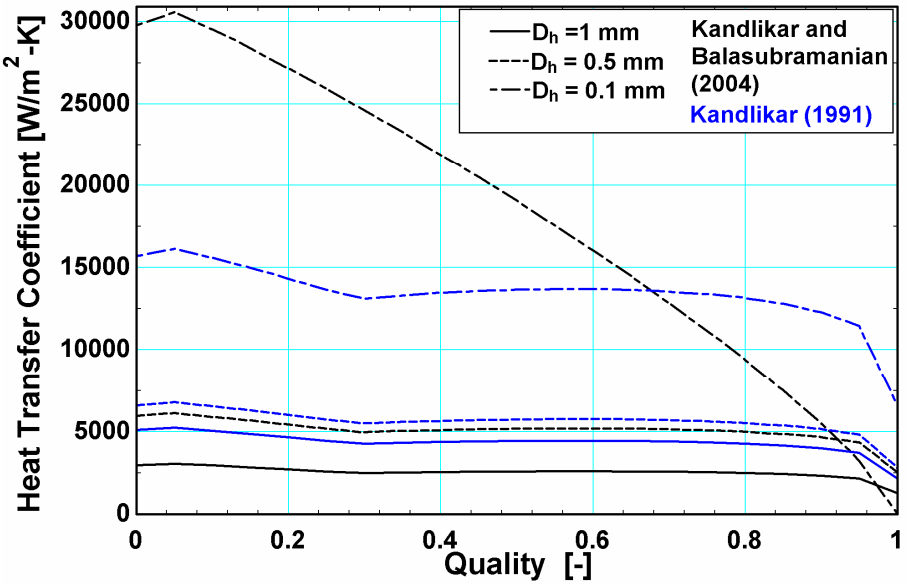

Figure 8: Boiling Heat Transfer Coefficient vs. Refrigerant Quality for a Conventional Correlation and a Mini-/ Micro-Channel Correlation

Convective condensation is the rejection of latent heat of a refrigerant as it changes phase from a saturated vapor to a saturated liquid, while flowing through a passage. As in flow boiling, various flow regimes are observed as the fluid transitions from a quality of 1 to 0. Flow regime in convective condensation progresses from annular flow with a liquid layer around a vapor core to stratified wavy flows, and slug flow and plug flow with larger, discrete vapor bubbles to bubbly flow with smaller bubbles distributed throughout the fluid with overlaps between these regions. However, most of

the heat transfer in the condensation process occurs under annular flow conditions (Carey 2008).

Soliman *et al.*'s (1967) correlation is a convective condensation correlation for annular flow developed for conventionally sized flow passages. Soliman *et al.*'s (1967) correlation directly considers shear at the interface of the vapor and liquid and at the tube wall. Traviss *et al.* (1973) proposed a relation for the local heat transfer coefficient for annual flow convective condensation, which considered the Martinelli parameter and the liquid-only Reynolds number and Prandtl number. Shah (1979) proposed a completely empirical correlation to fit the available convective condensation data for round tubes ranging in diameter from 7 to 40 mm. The data for this correlation were from water, R-11, R-12, R-22, R-113, and various organic working fluids. The mean deviation from data was found to be 15.4%.

As in saturated flow boiling, the processes involved in convective condensation in mini- and micro-channels vary from flow in conventionally sized channels. Through a simplified separate-cylinders model in small channels, Carey (2008) demonstrates that the film thickness should decrease and heat transfer coefficient increase as the tube diameter is diminished. It is noted that these trends are observed in high-performance heat exchangers. Carey (2008) and Kandlikar *et al.* (2006) provide a very detailed description of the recent research into convective condensation in small channels. There is a slight difference in flow regime as noted by Wu and Cheng (2005) and Chen and Peterson (2006). At high vapor qualities, there is initially core vapor flow with droplet flow at the tube walls, which soon transitions to annular flow. As quality decreases the injection flow regime, consisting of a series of bubble growth and detachment activities

(Wu and Cheng 2005), develops where the thickness of the liquid film increases until the vapor-liquid interface becomes unstable, pinching off bubbles. This is followed by slug-bubbly flow. Wang and Rose (2005) note that as the hydraulic diameter decreases, the annular flow regime persists over a larger quality range.

Wang *et al.* (2002) conducted heat transfer and flow visualization and measurement for R-134a condensing inside a horizontal, multiport, micro-finned tube with a hydraulic diameter of 1.46 mm over a range of parameters. They varied mass flux from 75 – 750 kg/m^{2}s and found that existing correlations over-predict heat transfer coefficient. They developed a correlation to represent the heat transfer coefficient for all of their data for use in condenser design. The reported mean deviation is ±6%, while 79.2% of the data were within ±10%.

Agarwal *et al.* (2010) measured heat transfer coefficients in six non-circular horizontal micro-channel tubes during condensation of R-134a. They considered various tube shapes including square, barrel, triangular, rectangular, and N-shaped, and also tubes with W-shaped inserts. The hydraulic diameter of the flow passages ranged from 0.424 – 0.839 mm, while the mass flux ranged from 150 – 750 kg/m^2-s. A modified version of an annular-flow-based shear driven heat transfer model for circular micro-channels (Bandhauer *et al.* 2006) was developed. It makes use of the interfacial shear stress between the liquid and vapor phases, developed in a previous investigation of condensation pressure drop in circular and non-circular micro-channels (Agarwal and Garimella 2009), and a 2-region turbulent dimensionless temperature to calculate the condensation heat transfer coefficient. The average absolute deviation for the overall model, including a mist-flow based correlation for use with triangular, N-shaped, and W-

insert channels, is 16% with 77% of the data predicted to within 25%. The average deviations for square and rectangular cross sections, which are relevant to the present investigation, are +13% and +15%, respectively.

Figure 9 is a plot of condensation heat transfer coefficient versus quality for the three conventional convective condensation correlations (Soliman *et al.* 1967; Traviss *et al.* 1973; Shah 1979) and the mini-/micro-channel convective condensation correlations (Wang *et al.* 2002; Agarwal *et al.* 2010) assuming a tube with hydraulic diameter of 1 mm and fluid R-134a. Flow conditions were assumed to be typical of those found in the condensers in the present study (G = 150 kg/m^2-s, T_{sat} = 40°C, P_{sat} = 1017 kPa). It can be seen in Figure 9 that Shah's (1979) and Soliman *et al.*'s (1967) correlations exhibit similar trends, with heat transfer coefficient initially increasing with decreasing quality and then decreasing as quality continues to decrease. Heat transfer coefficients calculated using Traviss *et al.*'s (1973) and Wang *et al.*'s (2002) correlations are much higher for high vapor quality but decrease as quality decreases, eventually reaching values comparable to the other two correlations. Agarwal *et al.*'s (2010) correlation yields heat transfer coefficient values that are in general agreement with the other correlations at low to mid-range qualities, but the heat transfer coefficient values begin to increase very rapidly for qualities greater than 0.7. Calculations were not able to be carried out for qualities higher than 0.85; this is attributed to the fact that the mass flux investigated here is at the lower limit of applicability for this correlation. Figure 10 is a plot of condensation heat transfer coefficient versus quality for a hydraulic diameter of 0.5 mm, while Figure 11 is the same plot for a hydraulic diameter of 0.1 mm. The trends

found for the 1 mm case are also found in the 0.5 mm and 0.1 mm case; however, the predicted values of the heat transfer coefficient from each correlation are much higher.

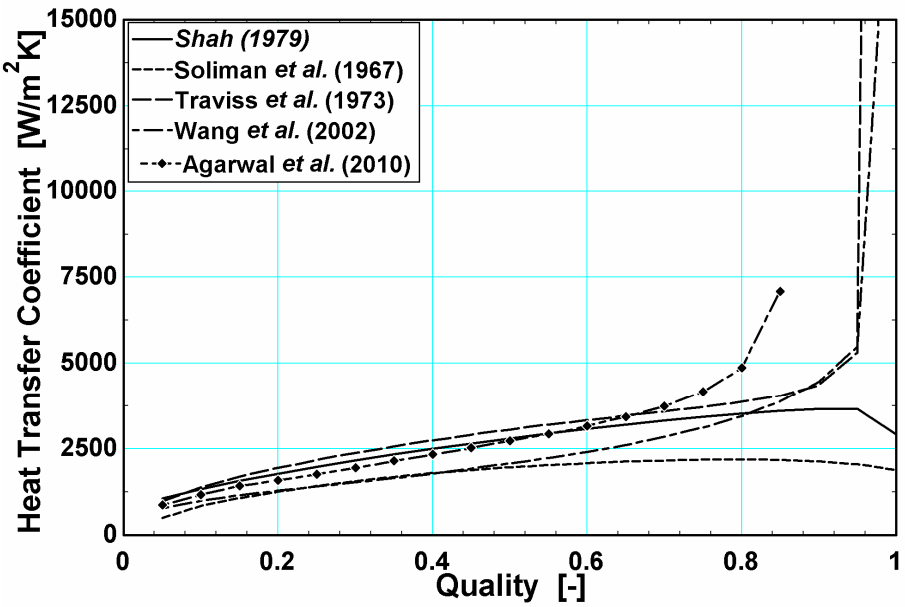

Figure 9: Condensation Heat Transfer Coefficient vs. Refrigerant Quality, D_h = 1 mm

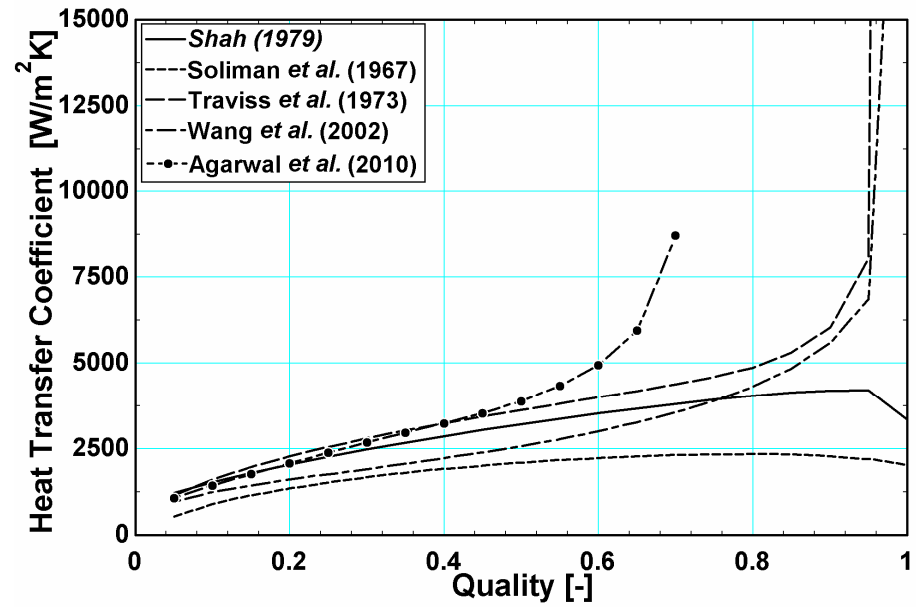

Figure 10: Condensation Heat Transfer Coefficient vs. Refrigerant Quality, D_h = 0.5 mm

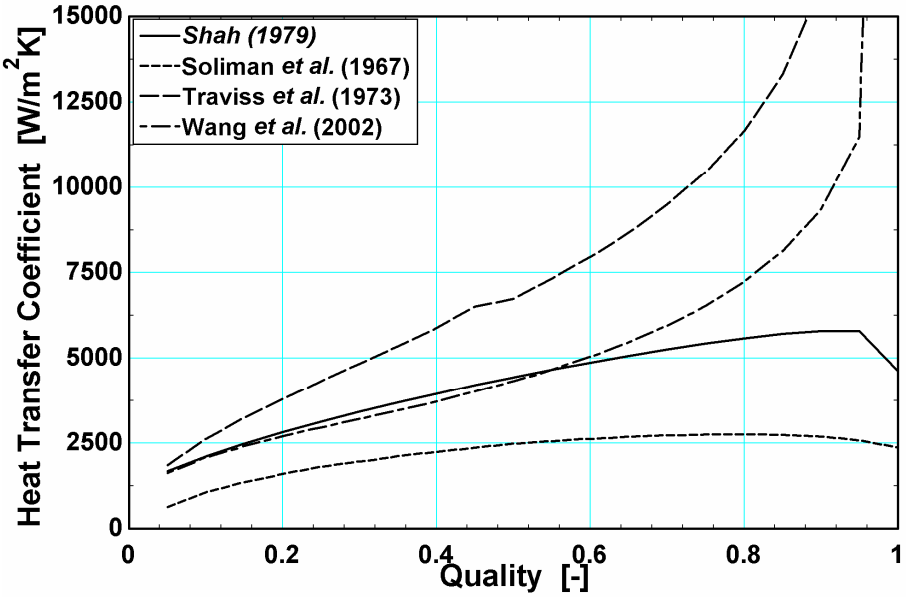

Figure 11: Condensation Heat Transfer Coefficient vs. Refrigerant Quality, D_h = 0.1 mm

Pressure drop of a two-phase fluid flow can be determined by considering the liquid and vapor as existing as two separate, distinct volumes which flow concurrently. This is the so called separated flow model. The frictional two-phase pressure drop is generally considered to be proportional to the frictional pressure drop for the liquid phase or vapor phase if it were flowing alone. The proportionality factor is known as the two-phase multiplier. Lockhart and Martinelli (1949) originally proposed a method for determining either the liquid or vapor two-phase multiplier for adiabatic gas-liquid flow in a round tube. They assumed that the multiplier was only a function of the Martinelli parameter, the square root of the ratio of liquid-phase pressure drop to vapor-phase pressure drop. Chisholm and Laird (1957) re-formulated Lockhart and Martinelli's correlation accounting for the flow regime (turbulent or laminar) of the liquid-only or vapor-only flow through the use of tabulated constants. Butterworth (1975) developed a

single form for the many correlations of the void fraction to be used when calculating the acceleration component of the two-phase pressure drop, including Lockhart and Martinelli's (1949). Carey (2008) notes that the Lockhart-Martinelli methodology yields accurate results over a wide range of conditions. Carey (2008) also notes that surface tension and viscous forces tend to dominate gravitational forces in mini-/micro-channels. Kandlikar *et al.* (2006) provides a very detailed discussion of pressure drop of boiling and condensing fluids in mini-/micro-channels. The approaches to account for the change in channel size are modifications of the methods for conventional tube sizes to achieve better agreement with data. Ohtake *et al.* (2006) found that two-phase multiplier data from their experiments on small circular tubes agreed well with the conventional Lockhart-Martinelli correlation.

2.3.1.2 Air-Side Heat Transfer Coefficient and Pressure Drop

As with the refrigerant, one must be able to adequately represent the heat transfer and pressure drop occurring on the air-side of the heat exchanger. Air-side heat transfer in the present study is assumed to be enhanced by the use of corrugated, multi-louvered fins. This is a common enhancement found in many applications, including automotive air conditioners (Birch 1995). This is the same air-side enhancement method used by Garimella and Wicht (1995) when they modeled a flat-tube ammonia condenser. They employed the Stanton number and friction factor correlations developed by Sunden and Svantesson (1992). When Schwentker *et al.* (2006) modeled flat-tube, louvered-fin heat exchangers, they utilized the Chang and Wang (1997) and the Chang *et al.* (2000) correlations to represent the air-side heat transfer.

Sunden and Svantesson (1992) determined that the existing correlations for the *j*- (Colburn) and *f*- factors, though they sometimes gave acceptable results, were not generally accurate when compared with available data. They provided adjustments to Davenport's (1983) dimensional correlation and Achaichia and Cowell's (1988) non-dimensional correlation; however, they also developed new correlations using multiple regression analysis, which they determined matched their measured data very well, though it was only for six samples (as noted by Chang and Wang (1997)). Chang and Wang (1997) developed a generalized heat transfer correlation for the louver fin geometry from available data. The 91 analyzed samples came from heat exchangers with different geometric parameters, such as louver angle, louver length, louver pitch, tube width, fin length, and fin pitch. They found that 89.3% of their data were correlated within ±15% with a mean deviation of 7.55%, which they report as being much better than the results for other correlations. In a continuation of Chang and Wang's (1997) work, Chang *et al.* (2000) considered the same 1109 data points in 91 samples to develop a friction factor correlation for flow across a louver fin geometry. They found that their proposed equation correlated 83.14% of the data within ±15% with a mean deviation of 9.21%. More recently, Chang *et al.* (2006) proposed an amendment to the Chang *et al.* (2000) correlation to smooth a discontinuity between Reynolds number regions.

2.3.2. Compressor Modeling

There are two general methods for modeling compressors: detailed mechanical models that capture the effect of the various compressor components on performance (Kim and Bullard 2002; Perez-Segarra *et al.* 2005; Duprez *et al.* 2007; Navarro *et al.* 2007; Castaing-Lasvignottes and Gibout 2010) and empirical equations/data sets that

correlate certain variables with isentropic efficiency, volumetric efficiency, and compressor power (Cullimore and Hendricks 2001; Goodman 2008). Goodman (2008) used data for a reciprocating CO_2 compressor to develop, through regression analysis, a biquadratic equation with suction pressure, discharge pressure and suction superheat as variables to predict isentropic efficiency, volumetric efficiency, and compressor power. Performance data for a compressor, such as isentropic and volumetric efficiency and compressor power, can be tabulated as a function of compressor speed and suction and discharge pressures and can be provided in graphical or tabular form or as a set of equations.

Detailed, thermo-mechanical models of compressors can either be very general or very specific, depending on the desired level of complexity and available data. Duprez *et al.* (2007) developed a simple, thermodynamically realistic model of reciprocating and scroll compressors that calculated working fluid mass flow rate and power consumption based upon operating conditions, including suction line diameter, compressor speed, swept volume, dead space, and desired suction and discharge pressures. They claim that all of the data required for successful modeling are available in a typical technical data sheet or from simple matching of model results with stated power consumption values. They report model discrepancies from calculated data of 3% on average for the reciprocating compressor model and 3.5% for the scroll compressor model.

Perez-Segarra *et al.* (2005), Navarro *et al.* (2007), and Castaing-Lasvignottes and Gibout (2010) present very detailed compressor models. Each sought to study the effects of the smallest parameters and sources of losses, including valve dimensions, activity, and leakages; fluid heating due to interactions with the body of the compressor and

nearby high-pressure fluid; and detailed mechanical interactions of various compressor components. They characterize not only the overall performance of the compressor, but the detailed thermodynamic compression process. The models developed by these investigators require detailed compressor design information including geometries and configurations.

2.4. System Modeling

The goal of modeling a thermal management system is to predict how well a certain design will meet stated performance requirements including desired heating or cooling duty and *COP*. There are many papers that develop automotive air-conditioning system models. The best encountered source for these types of studies has been the Proceedings of the Vehicle Thermal Management Systems Conference sponsored by The Institution of Mechanical Engineers and the Society of Automotive Engineers. Most of the papers seem to fall into two main categories represented by the following investigations. Detailed, often transient, system models seek to fully characterize the operation of the system in response to changing conditions, including transient heat loads (Cullimore and Hendricks 2001; El Bakkali *et al.* 2003; Hendricks 2003; Thelen and Zoz 2003; Lou 2005). The second type of study seeks to integrate a detailed model of a single component into a system model (Laboe and Gondusky 1995; Preissner *et al.* 2001; Mann and Nies 2003; Rahman *et al.* 2003). Some models are provided by corporations to support their products (Carlyle 2010).

The first category of system models is well represented by the work of Lou (2005). Lou (2005) sought to develop a dynamic system model that would allow for the integration of a 3-D dynamic model that captures the mechanical aspects of the

compressor with 1-D heat transfer, fluid flow and control valves. It included a detailed variable displacement compressor model, transient models for the control valve and thermostatic expansion valve (TXV), and simplified heat exchanger, receiver, and hose models. Some of the potential detail of the heat exchanger models was sacrificed so that the cooling system model could be incorporated in to an electronic, automatic temperature control model of the passenger cabin.

Rahman *et al.*'s (2003) work represents the second category of system modeling. Rahman *et al.* (2003) designed a 1-D model to simulate the performance of an automotive air-conditioning system. The component models were simplified to achieve model convergence. However, the component models were modified with empirical calibration constants to match up system model prediction and actual system performance. The authors found that their model results matched well with experimental performance at typical vehicle speeds and at idle conditions.

Jiang (2001) modeled a hydronically coupled, residential heat pump suitable for heating and cooling. An ideal cycle to meet both heating and cooling requirements was determined; the results of this cycle were supplied to detailed compressor and heat exchanger models to determine the necessary geometries and configurations. Heat exchanger modeling was carried out in segmental detail, much as in Garimella and Wicht (1995), to develop a design that yielded a minimum heat exchanger mass.

2.5. Need for Further Research

Hydronically coupled systems have been used extensively in thermal management solutions. Their use in large-scale city or campus district heating and cooling is well documented. On a smaller scale, hydronically coupled distributed cooling systems have

been proposed for residential use. Unique liquid-coupled heating and cooling systems have been proposed for niche automotive thermal management challenges. Experimental investigations and system modeling have supported these developments.

The specific automotive thermal management challenges investigated for use of liquid-coupled systems include truck cabin cooling in non-idle, parked conditions and rapid warm-up of passenger spaces in cold climates. Little has been stated on the applicability of hydronically coupled systems to general automotive air-conditioning, much less automotive distributed cooling. Additionally, the system modeling in previous investigations has either not been described well or it is simplified to accommodate its incorporation into higher level models.

Therefore, this work focuses on extending the limited previous work on the automotive application of hydronically coupled, vapor-compression based systems. Four system configurations are modeled. Two of the systems model the cooling of one conditioned space air stream to determine the applicability of liquid-coupling to general automotive air-conditioning. The other two systems model the cooling of two, spatially distributed conditioned space air streams to determine the applicability of liquid-coupling to automotive distributed cooling. The objectives of this work are:

- Develop detailed heat exchanger component models that account for the influence of design geometry and variations in fluid properties, especially during phase-change processes.
- Use the component models to design appropriate heat exchangers for the four system configurations.

- Incorporate the component models into system models to investigate the applicability of liquid-coupled systems to general automotive air-conditioning and distributed cooling.

The methods used for developing these system- and component-level models are described in Chapter 3.

CHAPTER 3

DESCRIPTION OF COMPONENT MODELS

This chapter describes the heat exchanger, pump, fan, and compressor models developed in the present work. The heat exchanger models are used both for component design and as a part of the system models. To accommodate both needs, the heat exchanger modeling is very adaptable. This flexibility is achieved through the segmental nature of the model and the use of *EES* procedures and functions. In the component models, accuracy is increased by increasing the number of single-phase or phase-change segments is merely increased to achieve the desired level of detail. To capture the variation of the working fluids with respect to temperature and pressure, established correlations are used to model the single-phase and the phase-change heat transfer and pressure drop processes, coupled with the *EES* fluid property functions. Models of the compressor, pumps, and fans are also included. However, the level of detail in these models is comparatively less than that provided in the heat exchanger models because they are mainly intended for incorporation into the system models. The single- and two-phase fluid lines that connect the various components are also modeled to determine their effect on system operation. These line models are applicable to the refrigerant, the coupling liquid, or for the evaporator-side air stream.

3.1. Liquid-Coupled Condenser

A liquid-coupled condenser would be used in a system where the refrigerant containing portion of the cooling system is centrally located or isolated from the other parts of the vehicle. The liquid-coupled condenser model developed here calculates the heat rejected from the refrigerant to the high temperature coupling liquid loop. The model

also predicts the outlet temperature, pressure and enthalpy of the refrigerant and coupling liquid. The liquid-coupled condenser under investigation is assumed to be a counterflow micro-channel heat exchanger. A schematic of a representative heat exchanger is shown in Figure 12. To account for the spatially varying properties of the two-phase refrigerant flow, the liquid-coupled condenser was modeled using a segmental approach. The conditions at each segment were used as the input values for the subsequent segment. For a given heat exchanger geometry, the local heat transfer coefficients, pressure drops, and heat transfer areas are calculated. To aid in the discussion of this model, a

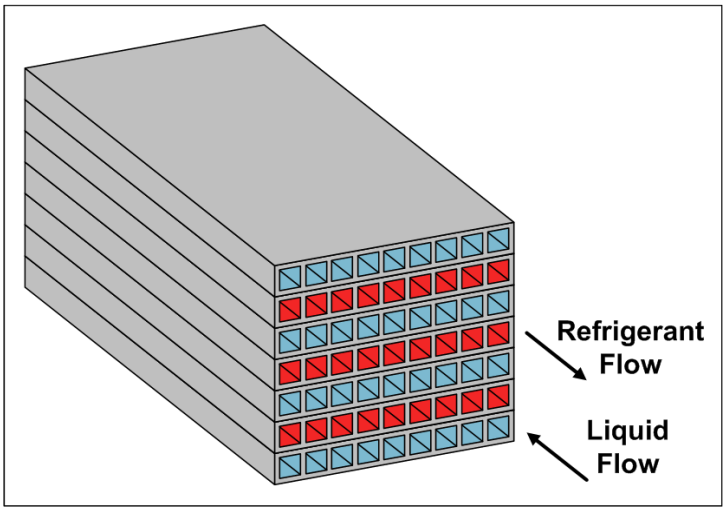

Figure 12: An Example Micro-Channel/Micro-Channel Counter-flow Heat Exchanger

representative liquid-coupled condenser is considered. The values presented are for one of the six segments used in this heat exchanger model. This condenser would be present in a system that has liquid-coupling on the ambient air-stream side. Table 1 provides the input parameters for this heat exchanger, including the number of tubes N_t, tube port width w_p, tube wall thickness t_t, tube outer width $t_{w,o}$, tube outer height $t_{h,o}$ and heat exchanger length L_{HX}. The length of the segment for the values that are presented is 0.088 m, while the total length of the heat exchanger is 0.415 m. The total heat

exchanger length is not an integer multiple of the reported segment length. This is due to the method employed in the segmental analysis, and is described later in detail. The refrigerant and liquid inlet temperatures, pressures, and mass flow rates are also specified.

Table 1: Liquid-Coupled Condenser Model Inputs

$t_{w,o,\ refg}$	76.2 mm	$w_{p,\ refg}$	0.7 mm	$N_{t,\ refg}$	23
$t_{h,o,\ refg}$	1 mm	$N_{p,\ refg}$	84	$t_{t,\ refg}$	0.15 mm
$t_{w,o,\ liq.}$	76.2 mm	$w_{p,\ liq.}$	0.7 mm	$N_{t,\ liq.}$	24
$t_{h,o,\ liq.}$	1 mm	$t_{t,\ liq.}$	0.15 mm	$N_{p,\ liq.}$	84
L_{HX}	0.415 m	$x_{liq.}$	30%	$\dot{m}_{refg.}$	0.04559 kg/s
$\dot{V}_{liq.}$	2.839 x 10^{-4} m^3/s (4.5 gpm)				

3.1.1 Basic Geometry and Area Calculations

Figure 13 shows the basic geometry of a representative tube, which, excepting dimensional differences, is the same for the refrigerant and the coolant. The tube inner width $t_{w,i}$ and inner height $t_{h,i}$ are calculated by Eqs. 3 and 4, respectively, where $t_{w,o}$ is the tube outer width, $t_{h,o}$ is the tube outer height, and t_t is the tube thickness.

$$t_{w,i} = t_{w,o} - 2t_t \tag{3}$$

$$t_{h,i} = t_{h,o} - 2t_t \tag{4}$$

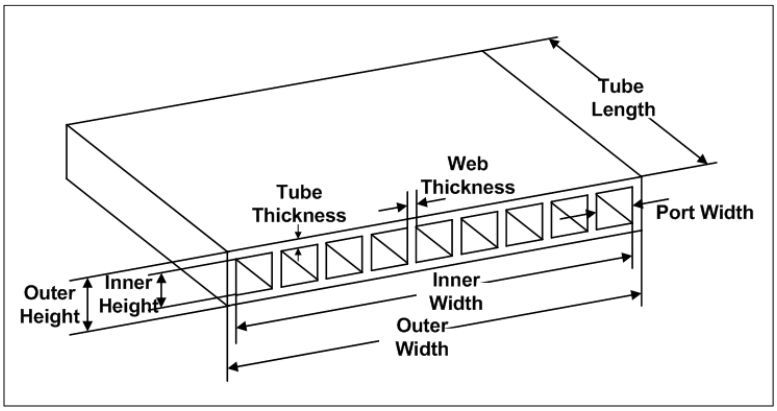

Figure 13: Tube Geometry Details for a representative 9 port tube ($N_p = 9$)

With $t_{w,\,o,\,refg}$ = 76.2 mm, $t_{h,\,o,\,refg}$ = 1 mm, and $t_{t,refg}$ = 0.15 mm, the refrigerant inner width and height are 75.9 mm and 0.7 mm, respectively. For this condenser, the dimensions are the same for the liquid tubes and the refrigerant tubes. The thickness of the strengthening web between each port t_{web} is calculated using Eq. 5, where N_p is the designated number of ports in the tube and w_p is the port width.

$$t_{web} = \frac{t_{w,i} - N_p w_p}{N_p - 1} \tag{5}$$

With $N_{p,\,refg}$ = 84 and $w_{p,\,refg.}$ = 0.7 mm, $t_{web,\,refg}$ = 0.206 mm. The value is the same for the liquid tube. The cross-sectional flow area of each tube $A_{c,flow}$ is calculated using Eq. 6 to be 41.16 mm^2 for both the refrigerant and liquid tubes.

$$A_{c,flow} = N_p w_p t_{h,i} \tag{6}$$

The hydraulic diameter of a single port $D_{h,port}$ is calculated using Eq. 7 to be 0.7 mm.

$$D_{h,port} = \frac{4 w_p t_{h,i}}{2\left(w_p + t_{h,i}\right)} \tag{7}$$

The inner direct surface area of a single tube $A_{d,i}$ is calculated using Eq. 8, where $L_{t,\,seg}$, the length of the tube segment, is 87.66 mm. This represents the top and bottom of each

port for the entire tube length. The calculated value for the refrigerant and liquid tube segment is 10,308 mm^2.

$$A_{\mathrm{d,i}} = 2N_{\mathrm{p}} w_{\mathrm{p}} L_{\mathrm{t}} \tag{8}$$

The outer direct surface area of the tube segment $A_{\mathrm{d,o}}$ is calculated using Eq. 9. This represents the top and bottom surface of the tube. The calculated value for the refrigerant and liquid tube segment is 13,359 mm^2.

$$A_{\mathrm{d,o}} = 2t_{\mathrm{w,o}} L_{\mathrm{t}} \tag{9}$$

The inner indirect surface area of the tube segment $A_{\mathrm{id,i}}$ is calculated using Eq. 10. This represents the sides of the ports and accounts for the side wall contributions on either side of the tube width. The refrigerant and liquid tube segment value is 10,308 mm^2.

$$A_{\mathrm{id,i}} = \left(2\left(N_{\mathrm{p}} - 1\right)t_{\mathrm{h,i}} + 2t_{\mathrm{h,i}}\right) L_{\mathrm{t}} \tag{10}$$

The total inner direct surface area in the heat exchanger segment $A_{\mathrm{d,i,tot}}$ is calculated using Eq. 11, where N_{t} is the total number of tubes, either for the refrigerant or for the liquid. With 23 refrigerant tubes, $A_{\mathrm{d,i,tot,refg.}}$ = 237,084 mm^2; 24 liquid tubes yield $A_{\mathrm{d,i,tot,liq.}}$ = 247,392 mm^2.

$$A_{\mathrm{d,i,tot}} = N_{\mathrm{t}} A_{\mathrm{d,i}} \tag{11}$$

The total outer direct surface area in the heat exchanger segment $A_{\mathrm{d,o,tot}}$ is calculated by Eq. 12 with 23 refrigerant tubes, $A_{\mathrm{d,o,tot,refg}}$ = 307,266 mm^2; 24 liquid tubes yield $A_{\mathrm{d,o,tot,liq}}$ = 320,625 mm^2.

$$A_{\mathrm{d,o,tot}} = N_{\mathrm{t}} A_{\mathrm{d,o}} \tag{12}$$

The total inner indirect surface area for the heat exchanger segment $A_{id,i,tot}$ is calculated by Eq. 13 with 23 refrigerant tubes, $A_{id,i,tot,refg}$ = 237,103 mm^2; 24 liquid tubes yield $A_{id,i,tot,liq}$ = 247,412 mm^2.

$$A_{id,i,tot} = N_t A_{id,i} \tag{13}$$

The fluid port aspect ratio, α^*, the ratio of the port height to the port width, is calculated by Eq. 14. The value is the same for refrigerant ports and liquid ports: $\alpha^* = 1$.

$$\alpha^* = t_{h,i} / w_p \tag{14}$$

The general design of the heat exchanger consists of one tube for refrigerant flow stacked on top of a tube for liquid flow. There is one extra liquid tube on top of the final refrigerant tube to maximize the heat transfer from the refrigerant to the liquid. Therefore, the total number of liquid tubes $N_{t,liq}$ is dependent upon the number of refrigerant tubes $N_{t,refg}$, as calculated by Eq. 15. As mentioned, there are 23 refrigerant tubes and 24 liquid tubes.

$$N_{t,liq} = N_{t,refg} + 1 \tag{15}$$

3.1.2 Liquid-Side Modeling

The liquid is a single-phase liquid at all times in the condenser. Therefore, the same calculations for heat transfer coefficient and pressure drop are applicable in each portion of the condenser. Hydronic-liquid properties are calculated at the segment average temperature and pressure using the 'BRINEPROP2' function, including density ρ_{liq}, specific heat Cp_{liq}, thermal conductivity k_{liq}, viscosity μ_{liq}, and Prandtl number Pr_{liq}. 'BRINEPROP2' is a function in EES for mixtures of water and a hydronic fluid (such as propylene-glycol), which allows the determination of properties such density, specific heat, thermal conductivity, and dynamic viscosity given the secondary refrigerant

concentration and temperature. The 'BRINEPROP2' function equations, properties and coefficients used in this procedure are based on data from the IIR/IIF handbook on secondary refrigerants (Melinder 1997). For an average liquid temperature $T_{liq.,\,avg}$ = 48.83°C and a propylene-glycol concentration of x = 30% by mass, ρ_{liq} = 1009 kg/m^3, Cp_{liq} = 3.955 kJ/kg-K, k_{liq} = 0.4668 W/m-K, $\mu_{liq} = 1.23 \times 10^{-3}$ kg/m-s, and Pr_{liq} = 10.38.

The liquid mass flux G_{cool} is calculated using Eq. 16, where $\dot{m}_{liq}$ is the total mass flow rate of the liquid through the condenser, 0.2857 kg/s, and $A_{c,liq}$ is the total cross-sectional area of a single tube, 41.16 mm^2. The liquid mass flow rate is specified in order to achieve a desired liquid change in temperature across the condenser, which directly affects the total temperature difference between the air and the refrigerant. With 24 liquid tubes, the mass flux is 289.2 kg/m^2-s.

$$G_{liq} = \frac{\dot{m}_{liq}}{A_{c,liq} N_{t,liq}} \tag{16}$$

The average velocity of the liquid through the condenser v_{liq} is calculated using Eq. 17 resulting in $v_{liq.}$ = 0.287 m/s.

$$v_{cool} = \frac{G_{cool}}{\rho_{cool}} \tag{17}$$

The Reynolds number Re_{liq} of the liquid flowing through the condenser is calculated using Eq. 18: Re_{liq} = 165.3.

$$Re_{cool} = G_{cool} D_{h,cool} / \mu_{cool} \tag{18}$$

The critical Reynolds number Re_{Crit} for internal flow through ducts with rectangular cross-section (Kakac *et al.* 1987) is calculated by the sequence given as Eq. 19, where α^* is the ratio of the channel width to height.

$$
\begin{aligned}
&n = 2, \text{if } \alpha^* < 1/3 \\
&n = 2 + 0.3\left(\alpha^* - 1/3\right), \text{if } \alpha^* > 1/3 \\
&m = 1.7 + 0.5\alpha^{*-1.4} \\
&u_{\text{ratio}} = \left(\frac{m+1}{m}\right)\frac{n+1}{n} \\
&Re_{\text{Crit}} = 4650/u_{\text{ratio}}
\end{aligned}
\tag{19}
$$

Since α^* = 1, n = 2.2, and m = 2.2, the u_{ratio} = 2.1157, Re_{Crit} = 2198. If the calculated liquid Reynolds number is less than the critical Reynolds number, then the liquid Darcy friction factor f_{liq} is calculated by Eq. 20, and the liquid Nusselt number Nu_{liq} is calculated by Eq. 21 (Kakac *et al.* 1987).

$$
f_{\text{liq}} = 96\left(\frac{1 - 0.8765\alpha^* + 1.2753\alpha^{*2} - 1.3086\alpha^{*3} + 0.5765\alpha^{*4}}{Re_{\text{liq}}}\right) \tag{20}
$$

$$
Nu_{\text{liq}} = 8.235\begin{pmatrix} 1 - 2.0421\alpha^* + 3.0853\alpha^{*2} - 2.4765\alpha^{*3} \\ +1.0578\alpha^{*4} - 0.1861\alpha^{*5} \end{pmatrix} \tag{21}
$$

Since this is the case, the resulting values are f_{liq} = 0.3872 and Nu_{liq} = 3.61. If the calculated coolant Reynolds number is greater than the critical Reynolds number, then the Darcy form of the friction factor is calculated using Eq. 22, and the Nusselt number is calculated using Eq. 23, Churchill's (1977a) correlation as a function of the circular friction factor (Kakac *et al.* 1987). The circular friction factor mentioned is the Darcy form of Churchill's (1977b) friction factor correlation for turbulent flow in circular cross-section pipes, in which $\varepsilon_{\text{pipe}}$ is the relative roughness of the tube, the ratio of the mean height of roughness of the tube to the tube diameter. A representative value of the relative roughness is chosen as 0.0005 for this study, as recommended for new aluminum piping (Munson *et al.* 2006).

$$f_{\text{liq}} = \left(1.0875 - 0.1125\alpha^{*}\right) f_{\text{circ}}$$

$$f_{\text{circ}} = 8\left(\left(\frac{8}{\text{Re}_{\text{liq}}}\right)^{12} + \frac{1}{\left(\left(2.457\ln\left(\frac{1}{\left(\left(7/\text{Re}_{\text{liq}}\right)^{0.9}\right) + 0.27\varepsilon_{\text{pipe}}}\right)\right)^{16} + \left(\frac{37530}{\text{Re}_{\text{liq}}}\right)^{16}\right)^{1.5}}\right)^{\frac{1}{12}} \tag{22}$$

$$\varepsilon_{\text{pipe}} = 0.0005$$

$$Nu_{\text{liq}} = \left(4.364^{10} + \left(\frac{e^{\left(\left(2200 - \text{Re}_{\text{liq}}\right)/365\right)}}{4.364^{2}} + \frac{1}{\left(6.3 + 0.079\left(\frac{f_{\text{circ}}}{8}\right)^{0.5}\text{Re}_{\text{liq}}\frac{\text{Pr}_{\text{liq}}}{\left(1+\text{Pr}_{\text{liq}}^{0.8}\right)^{\frac{5}{6}}}\right)^{2}}\right)^{-5}\right)^{1/10} \tag{23}$$

(For illustrative purposes, if the liquid Reynolds number were 4000 with α^{*} =1, f_{circ} = 0.2362, f_{liq} = 0.2303 and Nu_{liq} = 46.66.)

The pressure drop of the liquid across the given segment of the condenser ΔP_{liq} is calculated using Eq. 24, where L_{seg} is the length of the segment 87.66 mm. With f_{liq} = 0.3872, G_{liq} = 289.2 kg/m^2-s, $D_{\text{h,liq}}$ = 0.7 mm, and ρ_{liq} = 1009 kg/m^3, the segmental pressure drop is 2.06 kPa.

$$\Delta P_{\text{liq}} = \frac{f_{\text{liq}} G_{\text{liq}}{}^{2} L_{\text{seg}}}{2 D_{\text{h,liq}} \rho_{\text{liq}}} \cdot \left| 0.001 \ \ \frac{\text{kPa}}{\text{Pa}} \right| \tag{24}$$

The total pressure drop for the example liquid-coupled condenser is 12.5 kPa. The liquid outlet pressure for the given segment of the condenser is calculated using Eq. 25. With an inlet pressure of 547.7 kPa, the outlet pressure is 545.6 kPa.

$$P_{\text{liq,o}} = P_{\text{liq,i}} - \Delta P_{\text{liq}} \tag{25}$$

The local liquid heat transfer coefficient h_{liq} is calculated using Eq. 26. With $Nu_{\text{liq}} = 3.61$, $k_{\text{liq}} = 0.4668$ W/m-K, and $D_{\text{h,liq}} = 0.7$ mm, $h_{\text{liq}} = 2407$ W/m^2-K.

$$h_{\text{liq}} = Nu_{\text{liq}} k_{\text{liq}} / D_{\text{h,liq}} \tag{26}$$

3.1.3 Refrigerant-Side Modeling

3.1.3.1 Single-phase Pressure Drop and Heat Transfer Coefficient Calculations

As the refrigerant flows through the condenser, it transitions from a superheated vapor to a two-phase mixture to a subcooled liquid at the outlet. The methodology for calculating the single-phase refrigerant pressure drop and heat transfer coefficient is nearly the same as that for the coolant detailed in the previous section. The primary difference is that the fluid properties including density ρ_{refg}, specific heat Cp_{refg}, thermal conductivity k_{refg}, viscosity μ_{refg}, and Prandtl number Pr_{refg} are calculated at the average refrigerant temperature and pressure in each heat exchanger segment. Refrigerant properties are determined using the fundamental equation of state developed by Tillner-Roth and Baehr (1994). The local refrigerant pressure drop ΔP_{refg} and heat transfer coefficient h_{refg} are calculated by Eqs. 27 and 28, respectively.

$$\Delta P_{\text{refg}} = \frac{f_{\text{refg}} G_{\text{refg}}{}^2 L_{\text{seg}}}{2 D_{\text{h,refg}} \rho_{\text{refg}}} \cdot \left| 0.001 \ \frac{\text{kPa}}{\text{Pa}} \right| \tag{27}$$

$$h_{\text{refg}} = Nu_{\text{refg}} k_{\text{refg}} / D_{\text{h,refg}} \tag{28}$$

At an average temperature and pressure of 62.5°C and 1492 kPa, a condition that is found in the de-superheating section of the condenser, the fluid properties are: $\rho_{\text{refg}} = 76.17$ kg/m^3, $Cp_{\text{refg}} = 1.608$ kJ/kg-K, $k_{\text{refg}} = 0.01778$ W/m-K, $\mu_{\text{refg}} = 1.355 \times 10^{-5}$ kg/m-s, $Pr_{\text{refg}} =$

0.9809. With Re_{refg} = 2487, f_{refg} = 0.03997, G_{refg} = 48.16 kg/m^2-s, $D_{h,refg}$ = 0.7 mm, $L_{t,seg}$ = 0.415 m, and Nu_{refg} = 5.863, ΔP_{refg} = 0.04758 kPa and h_{refg} = 148.9 W/m^2-K.

3.1.3.2 Two-phase Pressure Drop and Heat Transfer Coefficient Calculations

The contributions of the superheated and subcooled regions to the total condenser heat duty are small compared to the two-phase heat transfer region. Therefore, it is important to accurately model the phase-change fluid dynamic and heat transfer phenomena associated with the condensation process. The sample values in this discussion are for a condensing segment at the following conditions: x_{in} = 0.5816, x_{out} = 0.2521, T_{in} = 54.99°C, P_{in} = 1492 kPa. Fluid properties are calculated at the given temperature and pressure for saturated liquid and saturated vapor conditions: ρ_l = 1078 kg/m^3, ρ_v = 76.16 kg/m^3, μ_l = 1.325 × 10^{-4} kg/m-s, μ_v = 1.355 × 10^{-5} kg/m-s, and k_l = 0.06761 W/m-K.

The two-phase pressure drop consists of a frictional component and an acceleration, or deceleration, component. The refrigerant mass flux is calculated using Eq. 29; with $\dot{m}_{refg}$ = 0.04559 kg/s, $A_{c,refg}$ = 41.16 mm^2, and $N_{t,refg}$ = 23, G_{refg} = 48.16 kg/m^2-s.

$$G_{refg} = \frac{\dot{m}_{refg}}{A_{c,refg} N_{t,refg}} \tag{29}$$

The Reynolds numbers for the liquid Re_l and vapor components Re_v of the two-phase mixture are calculated by Eqs. 30 and 31, respectively, where μ_l is the saturated liquid viscosity and μ_v is the saturated vapor viscosity, and x_{avg} is the average segment quality.

$$Re_l = G_{refg}\left(1 - x_{avg}\right) D_{h,refg} \big/ \mu_l \tag{30}$$

$$Re_v = G_{refg} x_{avg} D_{h,refg} \big/ \mu_v \tag{31}$$

With x_{avg} = 0.417 and $D_{h,refg}$ = 0.7 mm, Re_l = 148.33 and Re_v = 1037. The Darcy friction factors for the liquid f_l and vapor f_v components are calculated based on the appropriate Reynolds number using the Churchill (1977b) correlation shown in Eq. 22. A relative roughness (ε) of 0.0005 is assumed: f_l = 0.6001; f_v = 0.04424.

The frictional pressure gradients for the liquid $(dP/dx)_l$ and vapor $(dP/dx)_v$ phases flowing alone in the tube are calculated using Eqs. 32 and 33, respectively, where ρ_l and ρ_v are the saturated liquid and vapor densities: $(dP/dx)_l$ = 0.1616 kPa/m; $(dP/dx)_v$ = 0.3256 kPa/m.

$$\left(dP/dx\right)_l = f_l G_{refg}{}^2 \left(1-x_{avg}\right)^2 \Big/ 2\rho_l D_{h,refg} \tag{32}$$

$$\left(dP/dx\right)_v = f_v G_{refg}{}^2 x_{avg}^2 \Big/ 2\rho_v D_{h,refg} \tag{33}$$

The Martinelli parameter X_M is calculated using Eq. 34: X_m = 0.7045.

$$X_M = \sqrt{\left(dP/dx\right)_l \Big/ \left(dP/dx\right)_v} \tag{34}$$

Lockhart and Martinelli (1949) suggest Eq. 35 as a correlation for determining the liquid two-phase multiplier ϕ_l for two-phase flow in horizontal tubes.

$$\phi_l = \left(1 + C/X_M + 1/X_M^2\right)^{1/2} \tag{35}$$

The constant C is dependent on the flow regime associated with the flow of the vapor and liquid alone in the tube. Chisholm and Laird (1963) recommend certain constants for each flow regime combination using the Reynolds numbers for the liquid and vapor alone in the tube as transition criteria. A Reynolds number of 2300 is deemed the turbulent transition point. For turbulent vapor-turbulent liquid C = 20; for turbulent vapor-laminar liquid C = 12; for laminar vapor-turbulent liquid C = 10; and for laminar vapor-laminar liquid C = 5. The frictional pressure drop across the given segment is calculated using

Eq. 36, where $L_{t,seg}$ is the segment length. Since both the vapor and liquid Reynolds numbers are laminar, C = 5, leading to a value of φ_l = 3.18; therefore, with $L_{t,seg}$ = 0.08766 m, $\Delta P_{refg,fric}$ = 0.1432 kPa.

$$\Delta P_{refg,fric} = \phi_l^2 \left(dP/dx\right)_l L_{seg} \tag{36}$$

The void fraction is needed to calculate the acceleration component of the two-phase pressure gradient. Void fraction is the ratio of volume occupied by the vapor to the total volume of the tube, or in flow situations, it can be considered the ratio of the flow vapor flow area to the total flow area. Butterworth (1975) proposed the following form for the many void fraction correlations.

$$\alpha = \left[1 + B_B \left(1 - x/x\right)^{n_1} \left(\rho_v/\rho_l\right)^{n_2} \left(\mu_l/\mu_v\right)^{n_3}\right]^{-1} \tag{37}$$

The constants for the Lockhart and Martinelli correlation are: B_B = 0.28, n_1 = 0.64, n_2 = 0.36, and n_3 = 0.07 (Butterworth 1975). The acceleration pressure drop is associated with the change in the void fraction; therefore, the acceleration pressure drop is dependent upon the change in quality from the inlet of the segment to the outlet of the segment. Thus, the acceleration pressure drop is evaluated using the inlet void fraction α_{in} and the outlet void fraction α_{out}, which are themselves evaluated using the inlet and outlet quality, x_{in} and x_{out} respectively. The inlet and outlet void fractions, at x_{in} = 0.5816 and x_{out} = 0.2521, are α_{in} = 0.9071 and α_{out} = 0.7976. The acceleration pressure drop across the segment is calculated using Eq. 39: ΔP_{Accel} = -0.007038 kPa (with the negative sign indicating deceleration due to condensation).

$$\Delta P_{Accel} = G_{refg}^2 \left(\left(\frac{x_{out}^{\,2}}{\alpha_{out}\rho_v} + \frac{\left(1 - x_{out}\right)^2}{\left(1 - \alpha_{out}\right)\rho_l} \right) - \left(\frac{x_{in}^{\,2}}{\alpha_{in}\rho_v} + \frac{\left(1 - x_{in}\right)^2}{\left(1 - \alpha_{in}\right)\rho_l} \right) \right) \cdot \left| 0.001 \ \ \frac{\text{kPa}}{\text{Pa}} \right| \tag{38}$$

The total pressure drop of the two-phase refrigerant across the segment is the sum of the frictional and acceleration components; it is calculated using Eq. 39: $\Delta P_{refg} = 0.1362$ kPa.

$$\Delta P_{refg} = \Delta P_{fric} + \Delta P_{Accel} \tag{39}$$

The two-phase heat transfer coefficient for convective condensation h_{cond} is calculated using Shah's (1979) correlation and Wang *et al.*'s (2002) correlation. Heat exchanger designs using each of these correlations are compared to determine if the difference between them has a significant impact. Shah's (1979) correlation is given as Eq. 40. It is applicable for mass fluxes from 11 to 211 kg/m^2-s and liquid Prandtl numbers less than 13. It is evaluated at the average segment pressure P_{avg} = 1492 kPa, the average segment quality $x_{avg} = 0.417$, and the fluid critical pressure $P_c = 4059$ kPa.

$$h_{cond} \Big/ h_{lo} = \left(1 - x_{avg}\right)^{0.8} + \left[3.8 x_{avg}^{\ 0.76} \left(1 - x_{avg}\right)^{0.04}\right] \Big/ \left(P_{avg} / P_c\right)^{0.38} \tag{40}$$

The liquid only heat transfer coefficient (h_{lo}) is found by assuming the total flow is a liquid at the saturation temperature. It is calculated using the Dittus-Boelter equation shown in Eq. 41, where k_l is the saturated liquid thermal conductivity and Pr_l is the liquid Prandtl number. With k_l = 0.06761 W/m-K, $\mu_l = 1.325 \times 10^{-4}$ kg/m-s and $Pr_l = 3.151$, $h_{lo} = 295.5$ W/m^2-K, and h_{cond} = 1018.6 W/m^2-K.

$$h_{lo} = 0.023 \left(k_l / D_{h,refg}\right) \left(G_{refg} D_{h,refg} / \mu_l\right)^{0.8} \mathrm{Pr}_l^{0.4} \tag{41}$$

Wang *et al.* (2002) postulate that the overall Nusselt Number for condensing refrigerant in rectangular millimeter-sized channels, Nu_{all}, can be represented by considering the possibility of both annular flow and stratified flow, as in Eq. 42; however this assumes that there is a transition from annular flow to stratified flow within a given length of tube. This assumption may be useful if longer tube lengths are employed, but

for this segmental analysis, this aspect is not used. Since Wang *et al.* (2002) suggest its use for all qualities, only the annular flow Nusselt number is used in this work.

$$Nu_{\text{all}} = f_{\text{anul}} Nu_{\text{anul}} + \left(1 - f_{\text{anul}}\right) Nu_{\text{strat}} \tag{42}$$

The Nusselt number for condensation in the annular regime is calculated by Eq. 43, where the liquid-only Reynolds number Re_l = 148.3, the local quality × = 0.417, the liquid Prandtl number Pr_l = 3.151, and the turbulent-turbulent Martinelli parameter X_{tt} = 0.4513. Nu_{anul} = 8.828.

$$Nu_{\text{anul}} = 0.0274 Pr_l Re_l^{0.6792} x^{0.2208} \left(1.376 + 8 X_{tt}^{1.655} / X_{tt}^{2}\right)^{0.5} \tag{43}$$

The heat transfer coefficient is then calculated using Eq. 27 given above: $h_{\text{Wang } et\ al.}$ = 852.7 W/m^2-K.

Two liquid-coupled condenser models were developed, one using Shah's (1979) correlation and one using Wang et al.'s (2002) correlation. Identical geometric parameters were specified for each model. The average condensing refrigerant heat transfer coefficient for the Shah based model is 1111 W/m^2-K, while the average condensing heat transfer coefficient in the Wang *et al.* based model is 1091 W/m^2-K. With identical inlet liquid and refrigerant temperatures and pressures, the Shah based model transfers 7.715 kW and yields a refrigerant outlet temperature of 51.97°C, while the Wang *et al.* based model transfers 7.624 kW and yields a refrigerant outlet temperature of 53.23°C. Extending the length of the heat exchanger in the Wang *et al.* based model by 0.01 m from 0.415 m to 0.425 m results in a 7.715 kW heat duty and a refrigerant outlet temperature of 51.97°. It appears that either correlation can be used for design purposes without significant impact on component size.

3.1.4 Overall Heat Exchanger Modeling

3.1.4.1 Segmental Approach

The overall heat exchanger calculations are carried out by considering the heat exchanger as a series of segments. The liquid-coupled condenser generally consists of three sections: the de-superheating section, the condensing section, and the sub-cooling section. There is little variation of the refrigerant or liquid properties in the single phase de-superheating or sub-cooling sections. Thus, each of these is assumed to be one segment. The condensing section, where the refrigerant is a two-phase mixture, is divided into an arbitrary number of segments by length. The number of segments varies from as few as 6 for a heat exchanger model that is incorporated into a system model to as many as 60 for a model intended for detailed component design. A schematic example of this segmental approach is presented in Figure 14. The variation of calculated heat duty and calculated level of sub-cooling for the given system is shown in Figure 15. For a condenser at a refrigerant inlet pressure of 1492 kPa and designed to reject 7.715 kW, a 6 segment model calculates a heat duty of 7.715 kW, while a 60 segment model calculates 7.53 kW, a 2.5% difference. The 6 segment model calculates a refrigerant pressure drop of 0.4581 kPa, while the 60 segment model calculates 0.5224 kPa, a 12.3% difference. The 6 segment model calculates a refrigerant outlet temperature of 51.97°C, while the 60 segment model calculates 54.53°C, a 4.7% difference.

In each heat exchanger model, the total length is specified. The length of the de-superheating segment is calculated be defining its refrigerant outlet state as being a saturated vapor. The segmental heat transfer calculations are then carried out in *EES*, matching the thermodynamically calculated segment heat duty with that calculated for the given geometry. Each of the two-phase segments, from the first to the penultimate, is

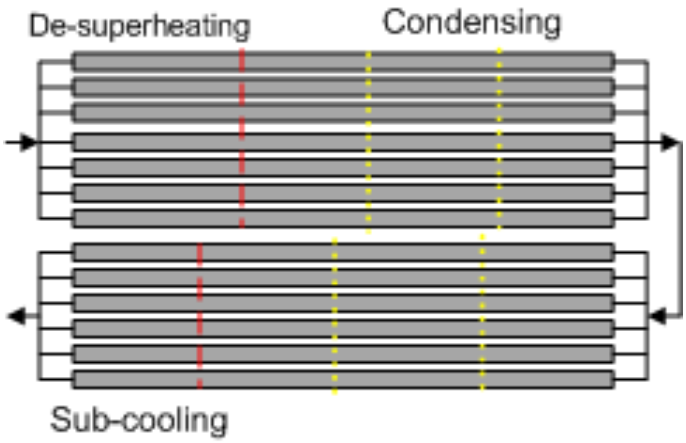

Figure 14: Example of the Segmental Approach in a Liquid-Coupled Condenser

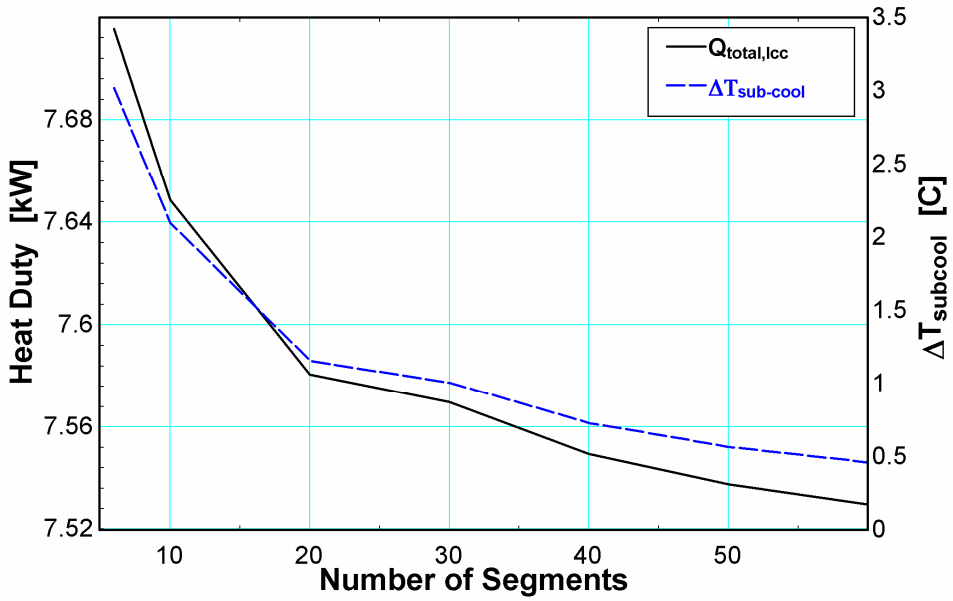

Figure 15: Liquid-Coupled Condenser Output Variation with respect to the Number of Model Segments

assigned a segment length by dividing the remaining heat exchanger length by the desired number of segments. The length of the final two-phase segment is determined by fixing its refrigerant outlet state as being a saturated liquid. The calculation is carried out in the same manner as for the de-superheating segment. Finally, any remaining segment length

belongs to the sub-cooling segment, allowing for the calculation of the refrigerant sub-cooling. The outlet of each segment is the inlet to the next.

3.1.4.2 Segment Heat Duty Calculations: ε-*NTU* Method

The segment heat duty is calculated using the effectiveness-*NTU* method. The segment *UA* is calculated using a thermal resistance network, which accounts for the effects of the various components of the heat transfer pathway. Heat is convected from the high temperature refrigerant to the refrigerant tube wall. This convection acts on both the direct and indirect internal refrigerant tube area. The heat is then conducted across the refrigerant tube wall and the liquid tube wall serially. Finally, the heat is convected from the liquid tube wall to the liquid across both the direct and indirect internal liquid tube area. Each of these processes can be represented as a thermal resistance, which when considered serially, constitute the total thermal resistance between the refrigerant and the liquid. This basic thermal resistance network is presented in Figure 16. Contact resistance is not included in this network as it is assumed that it would be negligible in this application. Longitudinal conduction along the tube length is also considered negligible. Lastly, the actual configuration of the tubes has a liquid tube on each side of a single refrigerant tube, leading to different boundary conditions for the refrigerant tubes near the edge of the heat exchanger; however, the difference between the unit cell depicted in Figure 16 and the actual boundary condition is assumed to be small due to the large number of tubes per pass in the heat exchanger designs employed, on the order of 40.

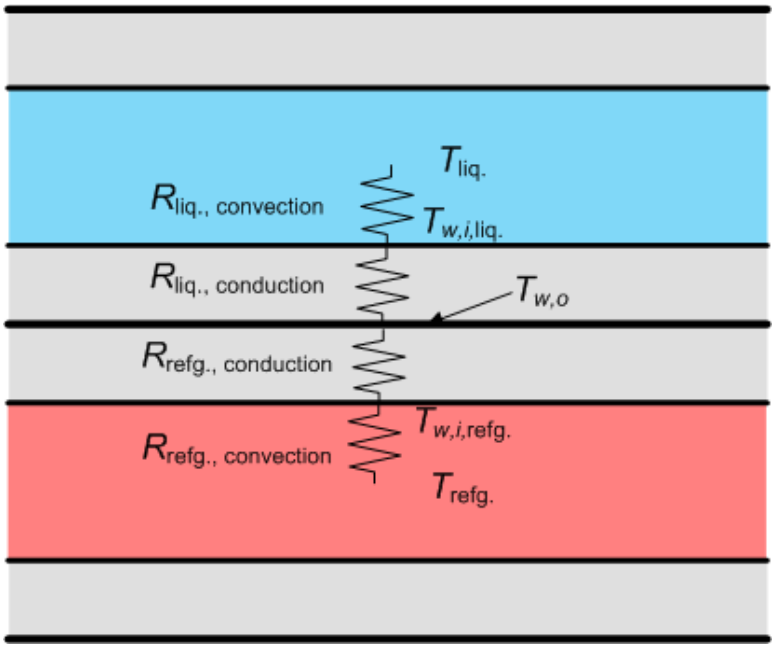

Figure 16: Schematic of the Liquid-Coupled Condenser Thermal Resistance Network

The total convective heat transfer area, both for the refrigerant tubes and the liquid tubes, is determined by combining the direct heat transfer area with the indirect heat transfer area by considering the tube port side walls as fins using a fin efficiency expression. The fin efficiency η_{fin} is calculated using Eq. 44, assuming the fin length is half the tube inner height $t_{h,i}$ with an adiabatic fin tip. Here h_{fluid} is the heat transfer coefficient of either the liquid or refrigerant, L_i is the length of the given segment, and k_{HX} is the thermal conductivity of the heat exchanger material evaluated at the wall temperature. For the refrigerant tube, $h_{refg.}$ = 1198 W/m^2-K, $t_{web,refg.}$ = 0.206 mm, L_i = 0.08766 m, k_{HX} = 237.1 W/m-K, $t_{h,i,refg.}$ = 0.0007 m yielding $m_{refg.}$ = 221.7 m^{-1}, and $\eta_{fin,refg.}$ = 0.998. For the liquid tube, $h_{liq.}$ = 2407 W/m^2-K, $t_{web,liq.}$ = 0.206 mm, L_i = 0.08766 m, k_{HX} = 237.1 W/m-K, $t_{h,i,liq.}$ = 0.0007 m yielding $m_{liq.}$ = 314.3 m^{-1}, and $\eta_{fin,liq.}$ = 0.996.

$$\eta_{\text{fin}} = \frac{\tanh\left(m t_{\text{h,i}}/2\right)}{\left(m t_{\text{h,i}}/2\right)}, \qquad m = \sqrt{\frac{h_{\text{fluid}}\left(2t_{\text{web}} + 2L_{\text{i}}\right)}{k_{\text{HX}} t_{\text{web}} L_{\text{i}}}} \tag{44}$$

The total effective convective heat transfer area of an array of tubes $A_{\text{i,tot,eff}}$ is calculated by combining the direct and indirect areas using Eq. 45. This calculation is carried out for both the refrigerant and the coolant separately. For the refrigerant tube, with $A_{\text{d,i,tot,refg.}}$ = 0.2371 m^2, $A_{\text{id,i,tot,refg.}}$ = 0.2371 m^2, $A_{\text{i,tot,eff,refg.}}$ = 0.4737 m^2. For the liquid tube, with $A_{\text{d,i,tot,liq.}}$ = 0.2474 m^2, $A_{\text{id,i,tot,liq.}}$ = 0.2474 m^2, $A_{\text{i,tot,eff,liq.}}$ = 0.4938 m^2.

$$A_{\text{i,tot,eff}} = A_{\text{d,i,tot}} + \eta_{\text{fin}} A_{\text{id,i,tot}} \tag{45}$$

The convective thermal resistance, of both the refrigerant $R_{\text{conv,refg}}$ and coolant $R_{\text{conv,cool}}$, is calculated using Eq. 46, where h_{fluid} is the heat transfer coefficient for the particular fluid. $R_{\text{conv,refg.}}$ = 0.00176 K/W; $R_{\text{conv, liq.}}$ = 0.00084 K/W.

$$R_{\text{conv}} = 1/A_{\text{i,tot,eff}} h_{\text{fluid}} \tag{46}$$

The area associated with the conduction heat transfer across the tube walls $A_{\text{conduction}}$ is calculated using Eq. 47. This area is calculated for both the refrigerant and liquid tubes. $A_{\text{conduction,refg.}}$ = 0.0066 m^2; $A_{\text{conduction,liq.}}$ = 0.0066 m^2.

$$A_{\text{conduction}} = \left(w_{\text{p}} N_{\text{p}} + t_{\text{web}}\left(N_{\text{p}} - 1\right)\right) L_{\text{i}} \tag{47}$$

The conduction resistance across the tube wall, for both the refrigerant $R_{\text{conduction,refg}}$ and liquid $R_{\text{conduction,liq.}}$, is calculated using Eq. 48, where t_{t} is the tube thickness. With t_{t} = 0.15 mm for both refrigerant and liquid tubes, $R_{\text{conduction,refg.}} = 9.508 \times 10^{-5}$ K/W; $R_{\text{conduction,liq.}} = 9.516 \times 10^{-5}$ K/W.

$$R_{\text{conduction}} = t_{\text{t}} / A_{\text{conduction}} k_{\text{HX}} \tag{48}$$

The total thermal resistance between the refrigerant and the liquid R_{total} for a given segment is the sum of the contributing resistances: $R_{\text{total}} = 0.00279$ K/W.

$$R_{\text{total}} = R_{\text{conv,refg}} + R_{\text{conduction,refg}} + R_{\text{conduction,cool}} + R_{\text{conv,cool}} \tag{49}$$

The value of UA for a given segment is calculated using Eq. 50: $UA_{\text{seg}} = 358.4$ W/K.

$$UA_{\text{seg}} = 1 / R_{\text{total}} \tag{50}$$

The thermal capacitances of the refrigerant and liquid for each portion of the condenser are calculated using Eqs. 51 and 52, respectively.

$$C_{\text{refrigerant}} = c_{\text{p refrigerant,avg}} \dot{m}_{\text{refrigerant}} \tag{51}$$

$$C_{\text{coolant}} = c_{\text{p coolant,avg}} \dot{m}_{\text{coolant}} \tag{52}$$

By definition, the capacitance for the two-phase refrigerant is infinite (Janna 1998). For the segment under consideration, a condensing section, the refrigerant capacitance is infinite, and $c_{\text{p,liq.}} = 3.955$ kJ/kg-K and $\dot{m}_{\text{liq.}} = 0.2857$ kg/s, yielding $C_{\text{liq.}} = 1.13$ kW/K. As an example, the refrigerant capacitance calculation in the de-superheating section is presented: $c_{\text{p,refg.}} = 1.608$ kJ/kg-K and $\dot{m}_{\text{refg.}} = 0.04559$ kg/s yielding $C_{\text{refg.}} = 0.0733$ kW/K while $C_{\text{liq.}} = 1.13$ kW/K. For each portion of the condenser, the minimum capacitance is determined. For the refrigerant and liquid mass flow rates in this study, in the de-superheating and sub-cooling portions, the refrigerant capacitance is the minimum. For the condensation portion, the liquid capacitance is the minimum. The capacitance ratio is calculated for each portion using Eq. 53. For the de-superheating section referenced earlier, $C_{\text{r}} = 0.0649$.

$$C_{\text{r}} = C_{\min} / C_{\max} \tag{53}$$

The number of transfer units, *NTU*, for each segment is calculated using Eq. 54. For the condensing section presented above, NTU = 0.3172.

$$NTU = UA/C_{\min} \tag{54}$$

The effectiveness as a function of the heat capacitance ratio and the number of transfer units (*NTU*) for a counterflow heat exchanger is calculated for each segment. Equation 55 is used when the refrigerant is single-phase; Eq. 56 is used when the refrigerant is two-phase. For the de-superheating segment briefly mentioned above, where $C_r = 0.0649$ and $NTU = 0.0427$, $\varepsilon_{\text{single-phase}} = 0.0418$. For the condensing segment under consideration, $\varepsilon_{\text{two-phase}} = 0.2715$.

$$\varepsilon_{\text{single-phase}} = 2 \cdot \left(1 + C_r + \frac{1 + exp\left(-NTU \cdot \left(1 + C_r^{\,2}\right)^{1/2}\right)}{1 - exp\left(-NTU \cdot \left(1 + C_r^{\,2}\right)^{1/2}\right)} \cdot \left(1 + C_r^{\,2}\right)^{1/2} \right)^{-1} \tag{55}$$

$$\varepsilon_{\text{two-phase}} = 1 - exp\left(-NTU\right) \tag{56}$$

The maximum possible heat duty for a segment is calculated using Eq. 57. With $T_{\text{refg.,in}} = 54.99°\text{C}$, $T_{\text{liq.,in}} = 47.86°\text{C}$, $C_{\min} = 1.13$ kW/K, $Q_{\max} = 8.061$ kW.

$$Q_{\max} = C_{\min}\left(T_{\text{refg.,in}} - T_{\text{liq.,in}}\right) \tag{57}$$

The actual segment heat duty is determined using the calculated values of $Q_{\max}$ and ε. For the condensing segment $Q_{\text{seg}} = 2.189$ kW, while the total heat exchanger duty $Q_{\text{LCC}} = 8.35$ kW. This segment duty is the largest with other condensing segments having duties of between 1.3 and 2.0 kW.

$$Q_{\text{seg}} = \varepsilon Q_{\max} \tag{58}$$

3.1.4.3 Segment Property Change Calculations

Heat transfer and pressure drop calculations for each segment are carried out using the average segment properties. The refrigerant and liquid pressure drops are calculated as described above, and the segment outlet pressure for the refrigerant and liquid are calculated by Eq. 59. For the condensing segment, $P_{\text{refg,in}}$ = 1492 kPa, $\Delta P_{\text{refg.}}$ = 0.136 kPa yielding $P_{\text{refg.,out}}$ = 1491.86 kPa; $P_{\text{liq.,in}}$ = 547.7 kPa, $\Delta P_{\text{liq.}}$ = 2.01 kPa yielding $P_{\text{liq.,out}}$ = 545.69.

$$P_{\text{out}} = P_{\text{in}} - \Delta P \tag{59}$$

The segment refrigerant outlet temperature is a function of the calculated outlet pressure and enthalpy as shown in Eq. 60.

$$T_{\text{out}} = T\left(P_{\text{out}}, h_{\text{out}}\right) \tag{60}$$

The refrigerant outlet enthalpy is calculated based upon the known inlet conditions, the known mass flow rate, and the calculated segment heat duty. With $h_{\text{refg.,in}} = f(x_{\text{in}} = 0.5816,$ P_{in} = 1492 kPa) = 216 kJ/kg, Q_{seg} = 2.189 kW, $\dot{m}_{\text{refg.}}$ = 0.04559 kg/s, $h_{\text{refg.,out}}$ = 168.0 kJ/kg. The refrigerant outlet temperature is then calculated as $T_{\text{refg.,out}}$ = 54.99°C.

$$h_{\text{out}} = h_{\text{in}} - Q_{\text{seg}} / \dot{m}_{\text{refg}} \tag{61}$$

The liquid outlet temperature is calculated by Eq. 62 with the assumption that all heat rejected from the refrigerant in the segment is transferred to the liquid. With $T_{\text{liq.,in}}$ = 47.86°C, $T_{\text{liq.,out}}$ = 49.79°C.

$$T_{\text{out,liquid}} = T_{\text{in,liquid}} + Q_{\text{seg}} / \left(\dot{m}_{\text{liquid}} c_{\text{p,liquid}}\right) \tag{62}$$

3.1.5 Other Heat Exchanger Calculations

There are many other important heat exchanger characteristics that are required for a complete description of the liquid-coupled condenser. These include physical dimensions, heat exchanger mass, and total heat transferred, each of which may be a design constraint or goal. The total length of the liquid-coupled condenser L_{LCC} is the sum of the lengths of the individual segments. Additionally, the condensing portion may have been considered as consisting of many segments, in which case its length would be the sum of the segment lengths. This relationship is shown in Eq. 63. The total length of the example liquid-coupled condenser is 0.415 m.

$$\begin{aligned} &L_{\mathrm{LCC}} = L_{\text{de-superheating}} + \sum_{i=1}^{n-1} L_{\text{condensing,i}} + L_{\text{condensing,n}} + L_{\text{sub-cooling}}, \\ &L_{\mathrm{LCC}} = 0.066m + 0.252m + 0.074m + 0.023m \\ &n = \text{number of condensing portion segments} \end{aligned} \tag{63}$$

Likewise, the total heat transferred from the refrigerant to the liquid in the condenser $Q_{\mathrm{LCC,total}}$ is the sum of the local heat duty of each segment. The total heat duty for the example liquid-coupled condenser is 8.35 kW.

$$\begin{aligned} &Q_{\mathrm{LCC}} = Q_{\text{de-superheating}} + \sum_{i=1}^{n} Q_{\text{condensing,i}} + Q_{\text{sub-cooling}}, \\ &Q_{\mathrm{LCC}} = 1.21kW + 5.33kW + 1.59kW + 0.23kW \\ &n = \text{number of condensing portion segments} \end{aligned} \tag{64}$$

The height of the heat exchanger h_{HX} is calculated using Eq. 65, accounting for each refrigerant and liquid tube. With $t_{\mathrm{h,o,refg.}} = t_{\mathrm{h,o,liq.}} = 1$ mm, and $N_{\mathrm{t,refg}} = 23$ and $N_{\mathrm{t,liq.}} = 24$, $h_{\mathrm{HX}} = 0.047$ m.

$$h_{\mathrm{HX}} = N_{\mathrm{t,refg}} t_{\mathrm{h,o,refg}} + N_{\mathrm{t,cool}} t_{\mathrm{h,o,cool}} \tag{65}$$

The mass of the liquid-coupled condenser m_{LCC} is determined by considering the density of the heat exchanger construction material ρ_{HX} and the volume occupied by the heat exchanger material V_{LCC}. The heat exchanger is assumed to be constructed of aluminum with material properties determined using the *EES* material properties functions. With the given tube dimensions and number of tubes, $V_{LCC} = 6.84 \times 10^{-4}$ m^3, and with $\rho_{HX} = 2702$ kg/m^3, $m_{HX} = 1.847$ kg.

$$\begin{aligned} V_{LCC} &= \left(t_{refg,h,o} t_{refg,w,o} - t_{refg,h,i} w_{p,refg} N_{p,refg}\right) L_{LCC} N_{t,refg} \\ &+ \left(t_{cool,h,o} t_{cool,w,o} - t_{cool,h,i} w_{p,cool} N_{p,cool}\right) L_{LCC} N_{t,cool} \end{aligned} \tag{66}$$

$$m_{LCC} = V_{LCC} \rho_{HX} \tag{67}$$

The internal volume of each segment of the refrigerant tubes is required to calculate the total refrigerant charge for the condenser, as shown by Eq. 68. For the condensing segment mentioned earlier, $Vol_{refg,\,seg} = \times 9.58 \times 10^{-5}$ m^3.

$$Vol_{refg,seg} = t_{h,i} w_p L_{seg} N_p N_t \tag{68}$$

The volume occupied by refrigerant vapor in each segment is calculated using Eq. 69, while the volume of refrigerant liquid in each segment is calculated using Eq. 70. The void fraction employed in this calculation is calculated using Eq. 37 given above. For the condensing segment with an average void fraction of 0.856, $Vol_{refg,vapor} = 8.2 \times 10^{-5}$ m^3 and $Vol_{refg,liq.} = 1.37 \times 10^{-5}$ m^3.

$$Vol_{refg.,vapor} = \alpha Vol_{refg.,seg} \tag{69}$$

$$Vol_{refg,liq.} = (1-\alpha) Vol_{refg.,seg} \tag{70}$$

The total mass of the refrigerant contained in each segment is calculated using Eq. 71.

$$m_{\text{refg.,seg}} = \rho_{\text{v}} Vol_{\text{refg.,vapor}} + \rho_{\text{l}} Vol_{\text{refg.,liq.}} \tag{71}$$

The total mass of refrigerant contained in the segment is $m_{\text{refg,seg}} = 0.022$ kg. The same method is used to calculate the refrigerant charge in the single-phase segments, with the knowledge that void fraction is 1 for saturated vapor and 0 for saturated liquid. The total refrigerant charge for the liquid-coupled condenser is calculated by summing the refrigerant charge in each segment, as shown in Eq. 72. The total refrigerant charge for the example LCC is $m_{\text{refg.,LCC}} = 0.1034$ kg.

$$\begin{aligned} m_{\text{refg,LCC}} &= m_{\text{refg,de-superheating}} + \sum_{i=1}^{n} m_{\text{refg,condensing,i}} + m_{\text{refg,sub-cooling}} \\ m_{\text{refg,LCC}} &= 0.0050kg + 0.0739kg + 0.0245kg \end{aligned} \tag{72}$$

3.2. Liquid-Coupled Evaporator

The liquid-coupled evaporator model calculates the heat transferred from the evaporator-side liquid loop to the refrigerant. The liquid in the evaporator-side loop would gain heat from a source such as conditioned space via a liquid-air heat exchanger, or a liquid-coupled electronics cooling module. A liquid-coupled evaporator would be found in a system where it is desired that the refrigerant containing portion of the cooling system be centrally located or isolated from the other parts of the vehicle. Like the liquid-coupled condenser, the liquid-coupled evaporator is assumed to be a micro-channel/micro-channel heat exchanger, where the refrigerant and coolant proceed in counter-flow through an array of micro-channel tubes. This is the same basic configuration that is shown in Figure 12. The liquid-coupled evaporator is also modeled using a segmental approach, with the outlet fluid property values of one segment serving as the input values for the subsequent segment. Detailed geometrical information of the heat exchanger is again required to calculate the appropriate heat transfer coefficients,

pressure drops, and surface areas. This includes the number of refrigerant and liquid tubes, the tube port width, the tube wall thicknesses, the tube width, and the heat exchanger length. The values of these parameters for an example liquid-coupled evaporator are given in Table 2.

Table 2: Liquid-Coupled Evaporator Model Inputs

$t_{w,o,\ refg}$	50.8 mm	$w_{p,\ refg}$	0.7 mm	$N_{t,\ refg}$	20
$t_{h,o,\ refg}$	1 mm	$N_{p,\ refg}$	56	$t_{t,\ refg}$	0.15 mm
$t_{w,o,\ liq.}$	50.8 mm	$w_{p,\ liq.}$	0.7 mm	$N_{t,\ liq.}$	21
$t_{h,o,\ liq.}$	1 mm	$t_{t,\ liq.}$	0.15 mm	$N_{p,\ liq.}$	56
L_{HX}	0.4 m	$x_{liq.}$	30%	$\dot{m}_{refg.}$	0.04559 kg/s
$\dot{V}_{liq.}$	2.839×10^{-4} m^3/s (4.5 gpm)				

Due to the similarity between the liquid-coupled evaporator and the liquid-coupled condenser, the modeling approach and the calculations are very similar. The basic geometry and area calculations are the same for both. Likewise, the liquid-side heat transfer and pressure drop modeling is identical between the two models. The refrigerant pressure drop calculations employed are the same for the evaporating two-phase mixture as for the condensing two-phase mixture; however, the calculations for the flow-boiling heat transfer coefficients are decidedly different. The overall heat exchanger modeling is essentially the same, consisting of a segmental approach using the effectiveness-*NTU* method for calculating the segment heat duty.

3.2.1 Refrigerant-Side Flow-Boiling Modeling

Both Kandlikar's (1990) correlation and Kandlikar and Balasubramanian's (2004) correlation are presented here because evaporators designed using each correlation are compared. Kandlikar's (1990) conventional tube size correlation is used to calculate the heat transfer coefficient for saturated flow boiling in the evaporation segments of the

liquid-coupled evaporator. The correlation is applicable across both convective boiling dominant and nucleate boiling dominant regimes. A modified version of the correlation (Kandlikar 1991) takes the heat transfer coefficient to be the maximum of the heat transfer coefficient from the convective boiling dominant regime or nucleate boiling dominant regime. The values presented here are from a phase-change segment in the example liquid-coupled evaporator model. The inlet refrigerant temperature, pressure, and quality are 5.896°C, 360.9 kPa, and 0.532, respectively. The liquid inlet temperature and pressure are 10.76°C and 412 kPa.

$$h_{\text{refg, flow boiling}} = \text{maximum of} \left\{ \begin{matrix} h_{\text{NBD}} \\ h_{\text{CBD}} \end{matrix} \right\} \tag{73}$$

Several preliminary calculations are necessary to calculate the heat transfer coefficients. The Boiling number *Bo* is calculated using Eq. 74,

$$Bo = q'' / G h_{\text{lv}} \tag{74}$$

where q'' is the heat flux determined from Eq. 75, where Q is the heat duty for the given segment, and A_{ht} is the sum of the direct and indirect heat transfer area, in the same manner as described for liquid-coupled condenser.

$$q'' = Q / A_{\text{ht}} \tag{75}$$

The latent heat of vaporization per unit mass h_{lv} is calculated using Eq. 76. The enthalpy of the saturated liquid and the enthalpy of the saturated vapor are calculated at the average temperature and the appropriate qualities. With h_{l} = 59.83 kJ/kg and h_{v} = 253.9 kJ/kg, h_{lv} = 194.07 kJ/kg.

$$h_{\text{lv}} = h_{\text{v}} \left(T_{\text{avg}}, x = 1 \right) - h_{\text{l}} \left(T_{\text{avg}}, x = 0 \right) \tag{76}$$

With Q_{seg} = 1.121 kW, $A_{ht,refg}$ = 0.1906 m^2, q'' = 5.88 kW/m^2; with G_{refg} = 83.07 kg/m^2-s Bo = 0.000364. The liquid only Froude number Fr_{le} is calculated using Eq. 77,

$$Fr_{le} = G_{refg}^2 \big/ \rho_l^2 g D_{h,refg} \tag{77}$$

where g is the acceleration due to gravity. With $D_{h,refg}$ = 0.7 mm, and ρ_l = 1275 kg/m^3, Fr_{le} = 0.618. The function $f_2(Fr_{le})$ is evaluated using Eq. 78 (Kandlikar 1991); due to the value of Fr_{le}, $f_2(Fr_{le})$ = 1.

$$f_2\left(Fr_{le}\right) = \begin{Bmatrix} \left(25Fr_{le}\right)^{0.3} & \text{for } Fr_{le} < 0.04 \text{ for horizontal tubes} \\ 1 & \text{for } Fr_{le} > 0.04 \text{ for horizontal tubes and vertical tubes} \end{Bmatrix} \tag{78}$$

The fluid-dependent parameter F_K is tabulated by Kandlikar (1991). For R134a, F_K = 1.63 as reported by Carey (2008). The Reynolds number for all of the flow as liquid Re_{le} is calculated using Eq. 79. With $\mu_l = 2.46 \times 10^{-4}$ kg/m-s, Re_{le} = 236

$$Re_{le} = G_{refg} D_{h,refg} \big/ \mu_l \tag{79}$$

In the Kandlikar correlation, the single-phase heat transfer coefficient for the liquid phase flowing alone h_{le} is required. Kandlikar (1991) recommends either the Gnielinski (1976) correlation shown in Eq. 80 or the Petukhov-Popov correlation (1963) shown as Eq. 81, depending on the local Reynolds number.

$$h_{le} = \left(k_l / d_i\right) \frac{\left[\left(Re_{le} - 1000\right) \mathrm{Pr}_l \left(f/2\right)_l\right]}{\left[1 + 12.7\left(\mathrm{Pr}_l^{2/3} - 1\right)\left(f/2\right)^{0.5}\right]} \tag{80}$$

$$\text{for } 0.5 \le Pr_l \le 2000 \text{ and } 2{,}300 \le Re_{le} \le 10^4$$

$$h_{le} = \left(k_l / d_i\right) \frac{\left[Re_{le} \mathrm{Pr}_l \left(f/2\right)_l\right]}{\left[1.07 + 12.7\left(\mathrm{Pr}_l^{2/3} - 1\right)\left(f/2\right)^{0.5}\right]} \tag{81}$$

$$\text{for } 0.5 \le Pr_l \le 2000 \text{ and } 10^4 \le Re_{le} \le 5 \times 10^6$$

In the above correlations the friction factor f is calculated using Eq. 82 (Kandlikar 1991).

$$f = \left[1.58\ln\left(Re_{le}\right) - 3.28\right]^{-2} \tag{82}$$

With f = 0.0349, Pr_l = 3.634, and k_l = 0.092 W/m-K, h_{le} = 598.6 W/m^2-K. The two-phase heat transfer coefficient for the nucleate-boiling-dominant regime is calculated using Eq. 83 (Kandlikar 1991). With x_{avg} = 0.596 and ρv = 17.67 kg/m^3, h_{NBD} = 2276.5 W/m^2-K.

$$\begin{aligned} h_{NBD} &= 0.6683\left(\rho_l/\rho_v\right)^{0.1} x_{avg}^{0.16}\left(1-x_{avg}\right)^{0.64} f_2\left(Fr_{le}\right) h_{le} \\ &+1058.0 Bo^{0.7} F_K \left(1-x_{avg}\right)^{0.8} h_{le} \end{aligned} \tag{83}$$

The two-phase heat transfer coefficient for the convective-boiling-dominant regime is calculated using Eq. 84 (Kandlikar 1991): h_{CBD} = 4222.34.

$$\begin{aligned} h_{CBD} &= 1.1360\left(\rho_l/\rho_v\right)^{0.45} x_{avg}^{0.72}\left(1-x_{avg}\right)^{0.08} f_2\left(Fr_{le}\right) h_{le} \\ &+667.2 Bo^{0.7} F_K \left(1-x_{avg}\right)^{0.8} h_{le} \end{aligned} \tag{84}$$

The Kandlikar and Balasubramanian (2004) flow-boiling heat transfer coefficient for flow in mini- and micro-channel passages is also used to model the flow-boiling in the liquid-coupled evaporator. To account for the differences in flow regimes and heat transfer mechanisms encountered in mini- and micro-channels, Kandlikar and Balasubramanian (2004) recommended certain modifications to Kandlikar's (1990) original correlation. These modifications include modifying the liquid-only heat transfer coefficient that is used in the conventional correlations. For turbulent liquid-only Reynolds numbers, Re_{le} > 3000, the fluid specific correlating factor, shown in Eq. 78, is to be taken as unity as the Froude number effect is expected to be negligible, as shown in Eq. 85.

$$f_2\left(Fr_{le}\right) = 1 \tag{85}$$

For the laminar liquid-only Reynolds number, Re_{le} <1600, it is suggested that the liquid-only heat transfer coefficient be calculated using constant values for liquid-only Nusselt number, where the constants vary according to channel cross section for laminar fully developed flow (C = 4.36 for round tubes with constant heat flux, C = 3.61 for square passage with constant heat flux, and C varies for rectangular aspect ratios).

$$h_{le} = Nu\, k_l / D_h \,, Nu = C \tag{86}$$

In the transitional range of the liquid-only Reynolds number, 3000 > Re_{le} > 1600, they suggest an interpolation between the liquid-only heat transfer coefficient values for the laminar and turbulent regimes of liquid-only Reynolds number. When the liquid-only Reynolds number is less than 100, Kandlikar and Balasubramanian argue that since the flow boiling mechanism is dominated by nucleate boiling, the two-phase heat transfer coefficient should be set equal to the heat transfer coefficient for the nucleate boiling dominated regime, which is given by Eq. 83.

$$h = h_{NBD} \tag{87}$$

Since Re_{le} = 236, h_{le} is calculated using Eq. 86 with C = 3.61: h_{le} = 474.7 W/m^2-K. This value is used in Eqs. 83 and 84 to calculate h_{NBD} and h_{CBD}, respectively: h_{NBD} = 1808 W/m^2-K, h_{CBD} = 3350 W/m^2-K.

Two models were developed to determine the effect of the choice of saturated flow-boiling heat transfer coefficient correlation. One used the Kandlikar (1990) correlation, and one used the Kandlikar and Balasubramanian (2004) correlation. The same refrigerant inlet conditions ($x_{refg,in}$ = 0.3023 and $P_{refg,in}$ = 362.2 kPa) and geometric parameters ($N_{t,refg}$ = 20, $N_{t,liq}$ = 21, $t_{w,o,refg}$ = $t_{w,o,liq.}$ = 50.8 mm, $t_{h,o,refg}$ = $t_{h,o,liq}$ = 1 mm, $N_{p,refg}$ = $N_{p,liq}$ = 56, $w_{p,refg}$ = $w_{p,liq}$ = 0.7 mm) were used for each model; only the length of the heat exchanger L_{HX} was allowed to vary. The model using the Kandlikar (1990)

correlation with L_{HX} = 0.366 m transfers 6.376 kW, with a refrigerant outlet temperature of 10.8°C, accounting for the superheating, while the model using the Kandlikar and Balasubramanian (2004) correlation requires L_{HX} = 0.4 m to transfer 6.375 kW with a resultant refrigerant outlet temperature of 10.75°C. This is an increase in length of 9.3%, which leads to an increase in mass of 9.4% from 0.947 kg to 1.04 kg and an increase in refrigerant pressure drop of 8.54% from 5.22 kPa to 5.66 kPa. Based on these results, the Kandlikar and Balasubramanian (2004) correlation is used to model the saturated flow-boiling in the subsequent component and system models.

3.2.2 Overall Heat Exchanger Modeling

The overall heat exchanger calculations for the liquid-coupled evaporator are essentially the same as for the liquid-coupled condenser. The liquid-coupled evaporator is considered as consisting of two main portions: the evaporating portion and the superheating portion. Multiple segments are used to accurately represent the change in refrigerant properties in the evaporating portion of the heat exchanger, while one segment is employed in the superheating portion. The lengths of all but the last evaporation portion segments are predetermined as a fraction of the total heat exchanger length; however, the length of the final evaporating segment is calculated by setting the last refrigerant outlet properties to be saturated vapor. Whatever length remains in the heat exchanger is assigned to the superheating segment. The effectiveness-NTU calculations are the same as in the liquid-coupled condenser except that it is recognized that the liquid is at a higher temperature than the refrigerant: UA_{seg} = 257.4 W/K, ε_{seg} = 0.2019, $Q_{max,seg}$ = 5.512 kW, Q_{seg} = 1.113 kW. The changes in refrigerant and liquid enthalpy, temperature and pressure are calculated in the exact same manner as in the liquid-coupled condenser with the assumption that all heat rejected from the liquid is transferred to the

refrigerant: $\Delta P_{refg,seg}$ = 1.30 kPa, $P_{refg,out}$ = 359.5 kPa, $h_{refg,out}$ = 186.6 kJ/kg, $T_{refg,out}$ = 5.78°C, $\Delta P_{liq.,seg}$ = 9.19 kPa, $P_{liq.,out}$ = 406.2 kPa, $T_{liq.,out}$ = 9.74°C. Likewise, the liquid-coupled evaporator heat exchanger mass (m_{LCE} = 1.036 kg), total length (L_{HX} = 0.4 m), total heat duty (Q_{LCE} = 6.375 kW), and refrigerant charge ($m_{refg,LCE}$ = 1.352 × 10^{-3} kg) are calculated in exactly the same manner as described for the liquid-coupled condenser.

3.3. Air-Coupled Condenser

The air-coupled condenser model calculates the heat rejected from the refrigerant to the ambient air, the changes in temperature of the air and refrigerant, and the air and refrigerant pressure drops across the condenser. The air-coupled condenser is assumed to consist of micro-channel flat tubes oriented parallel to one another, separated by multi-louvered fin structures that serve to enhance the air-side heat transfer. The refrigerant and air are oriented in cross-flow. A schematic of a representative heat exchanger is shown in Figure 17. As before, the heat exchanger is modeled in a segmented fashion to capture the effects of the condensing refrigerant. The following model description is illustrated by the use of the geometry and conditions for a representative air-coupled condenser. The geometric parameters required for this model are given in Table 3, including tube outer width $t_{w,o}$, tube port width w_p, tube thickness t_t, tube length L_t, fin thickness f_t, fin pitch f_p, fin depth c_w, and louver angle θ. The condenser refrigerant inlet temperature and pressure are 66°C and 1301 kPa, and the air inlet temperature is 37.78°C with 40% relative humidity. The refrigerant mass flow rate is 0.0411 kg/s and the air volumetric flow rate is 0.850 m^3/s (1800 cfm). The segment used to describe the following calculations is a condensing segment with an inlet refrigerant quality of 0.76 and pressure of 1299 kPa.

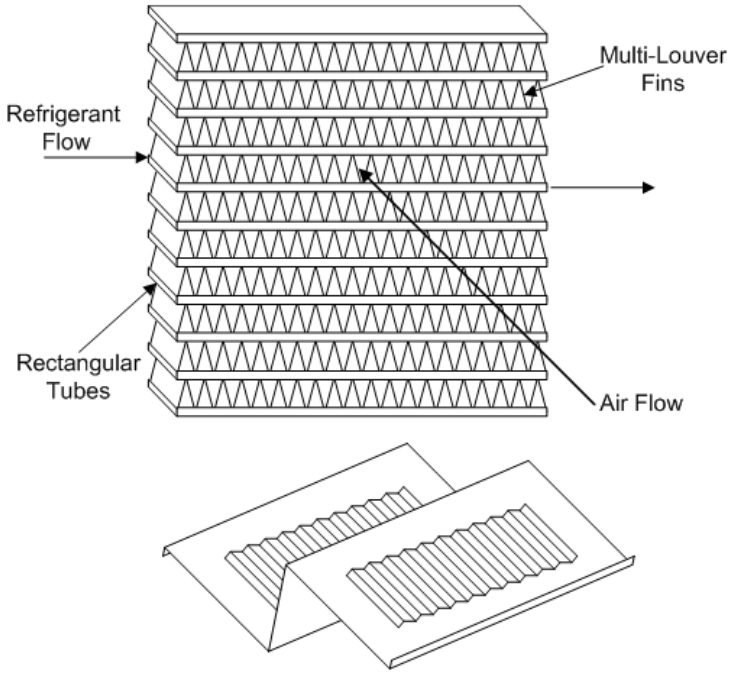

Figure 17: An Example Micro-Channel, Multi-Louverd Fin Heat Exchanger (Garimella and Wicht 1995)

The refrigerant flow passages in the air-coupled condenser are similar to those of the liquid-coupled condenser. Thus, the methodology for predicting the local refrigerant-side heat transfer coefficient and pressure drop is the same as in the liquid-coupled condenser, detailed in the previous section.

Table 3: Air-Coupled Condenser Geometric Parameters

$t_{w,o}$	25.4 mm	L_t	0.442 m	l_w	1.14 mm
$t_{h,o}$	1 mm	c_h	12.7 mm	l_l	11.43 mm
t_t	0.15 mm	c_w	25.4 mm	l_i	22.86 mm
N_p	28	f_t	0.127 mm	θ	30°
w_p	0.7 mm	f_p	1.27 mm		
$N_{t,pass}$	20	N_{pass}	2		

3.3.1 Basic Geometry and Area Calculations

The air-coupled condenser under investigation consists of three main sections: the de-superheating portion, the condensing portion, and the sub-cooling portion. Both the de-superheating and the sub-cooling portions are treated as one segment. The condensing

portion is subdivided into multiple segments to capture the effects of changing refrigerant quality.

Garimella and Wicht (1995) investigated various refrigerant routing options for air-coupled condensers and found that the mass of the heat exchanger was minimized when the refrigerant was conducted through multiple parallel passes consisting of varying numbers of tubes. This same refrigerant routing is employed in this investigation. A schematic of this orientation is shown in Figure 18. The number of tubes per pass and the number passes specified for each section of the condenser are design parameters that vary in heat exchanger optimization. Though the single-phase sections are treated using one

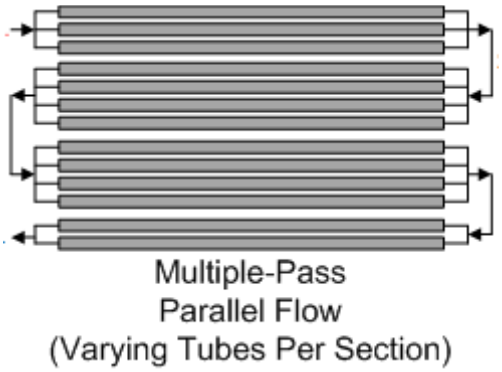

Figure 18: Condenser Refrigerant-side Pass Arrangement

segment, they may contain any number of tubes. Likewise, the two-phase section may consist of any number of passes of any number of tubes; however, each pass is always subdivided into smaller segments. The calculations presented here are for a single segment from a single pass. The results of one pass are the inputs of the subsequent pass. The basic geometry of a single tube is identical to that shown in Figure 13. Figure 19 shows the basic geometry of the multi-louvered fins that extend between each adjacent tube as seen in Figure 17.

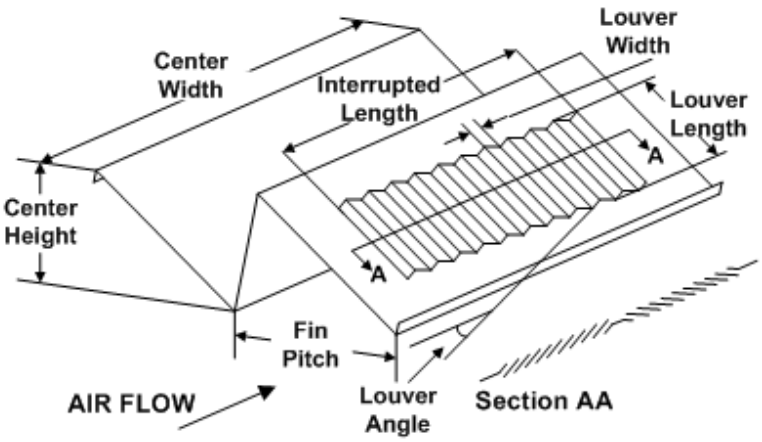

Figure 19: Fin Geometry Details
(Garimella and Wicht 1995)

The number of centers N_c is calculated using Eq. 88, where N_t is the number of tubes for a given pass. With 20 tubes per pass, there are 19 centers per pass. A total of two passes are used in this design, for a total of 40 tubes.

$$N_c = N_t - 1 \tag{88}$$

The height of the heat exchanger segment is calculated using Eq. 89, where c_h is the height of the center, which is the height of the multi-louvered fin structure. With $t_{h,o}$ = 1 mm and c_h = 12.7 mm, $h_{HX,pass}$ = 0.2613 m.

$$h_{HX,pass} = N_t t_{h,o} + N_c c_h \tag{89}$$

The total air-side cross-sectional area of a segment $A_{c,total}$ is calculated by Eq. 90, where L_{seg} is the length of the given segment. With L_{seg} = 0.1819 m, $A_{c,total}$ = 0.0475 m^2.

$$A_{c,total} = h_{HX,pass} L_{seg} \tag{90}$$

The face area of the segment blocked by the multi-louvered fins $A_{blocked,fin}$ is calculated by Eq. 91, where f_t is the fin thickness and f_p is the fin pitch. With f_t = 0.127 mm and f_p = 1.27 mm, $A_{blocked,fin}$ = 0.00439 m^2.

$$A_{\text{blocked,fin}} = N_c f_t c_h \left(L_{\text{seg}} / f_p \right) \tag{91}$$

The face area blocked by the tubes $A_{\text{blocked,tube}}$ is calculated using Eq. 92: $A_{\text{blocked,tube}}$ = 0.00364 m^2.

$$A_{\text{blocked,tube}} = N_t t_{h,o} L_{\text{seg}} \tag{92}$$

The free flow area for the condenser segment $A_{c,\text{free}}$ is calculated using Eq. 93: $A_{c,\text{free}}$ = 0.0395 m^2.

$$A_{c,\text{free}} = A_{c,\text{total}} - A_{\text{blocked,fin}} - A_{\text{blocked,tube}} \tag{93}$$

The perimeter of the air flow passage a_{per} for is calculated using Eq. 94. This length includes both vertical edges of each fin, the both edges of each tube minus the space occupied by fins, and both outside edges of each center structure. a_{per} = 75.81 m.

$$a_{\text{per}} = 2N_c \left(\left(L_{\text{seg}} / f_p \right) c_h + \left(L_{\text{seg}} - \left(L_{\text{seg}} / f_p \right) f_t \right) \right) + 2N_c c_h \tag{94}$$

The hydraulic diameter for the air flow $D_{h,\text{air}}$ is calculated using Eq. 95: $D_{h,\text{air}}$ = 2.084 mm.

$$D_{h,\text{air}} = 4 A_{c,\text{free}} / a_{\text{per}} \tag{95}$$

The direct air-side heat transfer area $A_{a,d}$ is the outside area of each tube minus the area blocked by fins plus the open area of each outer tube. It is calculated using Eq. 96, where $t_{w,o}$, the tube width and c_w the center width are the same dimension, 25.4 mm. $A_{a,d}$ = 0.1672 m^2.

$$A_{a,d} = 2\left(N_t - 1 \right)\left(t_{w,o} L_{\text{seg}} - \left(L_{\text{seg}} / f_p \right) f_t c_w \right) + 2 L_{\text{seg}} t_{w,o} \tag{96}$$

The indirect air-side heat transfer area $A_{a,id}$ is calculated by Eq. 97. It is the sum of the surfaces of the fin structure that are parallel to the air flow direction: $A_{a,id}$ = 1.755 m^2.

$$A_{\mathrm{a,id}} = 2c_{\mathrm{h}}c_{\mathrm{w}}\left(L_{\mathrm{seg}}/f_{\mathrm{p}}\right) \tag{97}$$

3.3.2 Air-Side Modeling

In the present geometry, the air flows in a cross-flow manner across the width of the tube stack, which is shown in Figure 17. It is assumed that the incident air flow is uniform. Thus, the fraction of the total air flow through a given section of the condenser $\dot{V}_{\mathrm{seg}}$ is equivalent to the ratio of the cross-sectional area of the section to the total cross-sectional area of the condenser, as calculated using Eq. 98, where $\dot{V}_{\mathrm{total}}$ is the total volumetric flow rate of air that flows through the condenser and L_{t} is the total length of the condenser. With $h_{\mathrm{HX,total}}$ = 0.5353 m, L_{t} = 0.442 m, $h_{\mathrm{HX,pass}}$ = 0.2613 m, L_{seg} = 0.1819 m, and 2 passes, $\dot{V}_{\mathrm{total}}$ = 0.8495 m^3/s and $\dot{V}_{\mathrm{seg}}$ = 0.1706 m^3/s.

$$\begin{aligned}
\dot{V}_{\mathrm{seg}} &= \dot{V}_{\mathrm{total}}\left(h_{\mathrm{HX,pass}}L_{\mathrm{seg}}/h_{\mathrm{HX,total}}L_{\mathrm{t}}\right) \\
h_{\mathrm{HX,total}} &= \sum_{n=1}^{i} h_{\mathrm{HX,pass},i} \\
\dot{V}_{\mathrm{seg}} &= 0.171\,\mathrm{m}^3/\mathrm{s}
\end{aligned} \tag{98}$$

All air properties are evaluated at the given inlet temperature, pressure, and humidity ratio. The air properties, viscosity $\mu_{\mathrm{a,in}}$, density $\rho_{\mathrm{a,in}}$, and constant pressure specific heat $c_{\mathrm{P,a,in}}$, are evaluated in EES, using the psychrometric property relations from Hyland and Wexler (1983). At $T_{\mathrm{air,in}}$ = 37.78°C, $P_{\mathrm{air,in}}$ =101.3 kPa, and 40% relative humidity, $\mu_{\mathrm{a,in}}$ = 1.904 × 10^{-5} kg/m-s, $\rho_{\mathrm{a,in}}$ = 1.106 kg/m^3, $c_{\mathrm{P,a,in}}$ = 1.038 kJ/kg-K.

The core air velocity $V_{\mathrm{air,core}}$ is calculated from the segmental volumetric flow rate and the free flow area of a given portion of the condenser using Eq. 99: $V_{\mathrm{air,core}}$ = 4.32 m/s.

$$V_{\mathrm{air,core}} = \frac{\dot{V}_{\mathrm{air,seg}}}{A_{\mathrm{c,free}}} \tag{99}$$

The average inlet air mass flow rate $\dot{m}_{air,in}$ for a portion of the condenser is calculated using Eq. 100: $\dot{m}_{air,in} = 0.1887$ kg/s.

$$\dot{m}_{air,in} = \dot{V}_{air,seg}\rho_{a,in} \tag{100}$$

The Reynolds number based on the louver width $Re_{air,core}$ is calculated using Eq. 101, where l_w is the louver width: $Re_{air,core}$ 286.

$$Re_{air,core} = \rho_{a,in}V_{air,core}l_w / \mu_{a,in} \tag{101}$$

Chang, Wang, and associates (Chang and Wang 1997; Chang *et al.* 2000) have correlated much of the available air-side, pressure drop and heat transfer coefficient data for multi-louvered fin geometries accounting for the louver geometry effects. Chang and Wang's (1997) j-factor correlation to model the heat transfer coefficient is given as Eq. 102. With $f_p = 1.27$ mm, $l_w = 1.14$ mm, $c_h = 12.7$ mm, $t_{w,o} = 25.4$ mm, $t_{h,o} = 1$ mm, and $f_t = 0.127$ mm, $j = 0.0328$.

$$\begin{aligned} j = \mathrm{Re}_{air,core}^{-0.49} &\left(\frac{\theta}{90\ [\mathrm{deg}]}\right)^{0.27}\left(\frac{f_p}{L_w}\right)^{-0.14}\left(\frac{c_h}{L_w}\right)^{-0.29} \times \\ &\left(\frac{t_{w,o}}{L_w}\right)^{-0.23}\left(\frac{L_l}{L_w}\right)^{0.68}\left(\frac{\left(c_h + t_{h,o}\right)}{L_w}\right)^{-0.28}\left(\frac{f_t}{L_w}\right)^{-0.05} \end{aligned} \tag{102}$$

The air-side heat transfer coefficient h_{air} is calculated using Eq. 103. With $c_{p,air} = 1.038$ kJ/kg-K, $Pr_{air} = 0.7446$, and $\rho_{air} = 1.106$ kg/m^3, $G_{air,core} = 4.78$ kg/m^2-s and $h_{air} = 197.8$ W/m^2-K.

$$\begin{aligned} h_{air} &= jc_{p,air}\frac{G_{air,core}}{Pr^{2/3}}; \\ G_{air,core} &= \rho_{air}V_{air,core} \end{aligned} \tag{103}$$

The Chang *et al.* (2000) correlation procedure employed in this study is given as Eq. 104. The basic correlation Chang *et al.* present is for the Fanning form of the friction factor; therefore, it is adjusted to Darcy form. With the multi-louvered fin geometric parameters presented in Table 1.3, $f_{\text{air,Darcy}} = 0.1045$.

$$
\begin{aligned}
&\text{For} Re_{\text{air,core}} < 150, \\
&f_1 = 14.39 Re_{\text{air,core}}^{-0.805\left(\frac{F_\text{p}}{c_\text{h}}\right)} \left(\ln\left(1.0 + \left(F_\text{p}/L_\text{w}\right)\right)\right)^{3.04} \\
&f_2 = \left(\ln\left(\left(\frac{f_\text{t}}{F_\text{p}}\right)^{0.48} + 0.9\right)\right)^{-1.435} \left(\frac{D_\text{h}}{L_\text{w}}\right)^{-3.01} \left(\ln\left(0.5 Re_{\text{air,core}}\right)\right)^{-3.01} \\
&f_3 = \left(F_\text{p}/L_1\right)^{-0.308} \left(t_{\text{w,o}}/L_1\right)^{-0.308} \left(\text{e}^{\left(-0.1167\frac{\left(t_{\text{h,o}}+c_\text{h}\right)}{t_{\text{h,o}}}\right)}\right) (\theta)^{0.35} \\
&\text{For} Re_{\text{air,core}} > 150, \\
&f_1 = 4.97\,\text{Re}_{\text{air,core}}^{\left(0.6049 - \frac{1.064}{\theta^{0.2}}\right)} \left(\ln\left(\left(\frac{f_\text{t}}{f_\text{p}}\right)^{0.5} + 0.9\right)\right)^{-0.527} \\
&f_2 = \left(\left(D_\text{h}/L_\text{w}\right)\ln\left(0.3 Re_{\text{air,core}}\right)\right)^{-2.966} \left(F_\text{p}/L_1\right)^{-0.7931\left(\frac{t_{\text{h,o}}+c_\text{h}}{c_\text{h}}\right)} \\
&f_3 = \left(\left(t_{\text{h,o}} + c_\text{h}\right)/t_{\text{h,o}}\right)^{-0.0446} \left(\ln\left(1.2 + \left(L_\text{w}/F_\text{p}\right)^{1.4}\right)\right)^{-3.553} (\theta)^{-0.477} \\
&f_{\text{Fanning}} = f_1 f_2 f_3 \\
&f_{\text{air,Darcy}} = 4 f_{\text{Fanning}}
\end{aligned}
\tag{104}
$$

The air-side pressure drop, ΔP_{air}, for each condenser segment is calculated using Eq. 105. The air-side pressure drop for the segment under consideration is 13.14 Pa.

$$\Delta P_{\text{air}} = \left(f_{\text{air}} c_\text{w} \rho_{\text{a,in}} V_{\text{air,in}}^2\right)/\left(2 D_{\text{h,air}}\right) \tag{105}$$

3.3.3 Overall Heat Exchanger Modeling

A segmental approach is used to model the three portions of the air-coupled condenser: the de-superheating, condensing, and sub-cooling sections. As in the other heat exchanger models, each single-phase section is treated as one segment, while

multiple segments are used for the phase-change portion. One heat exchanger segment consists of the specified length of tube and the multi-louvered fin structure directly adjacent to the tube segment. Similar to the liquid-coupled models, the refrigerant outlet of one segment is used as the input to the next segment. However, because the air-coupled condenser is a cross-flow heat exchanger, the air that flows across a given segment does not proceed to another segment; it exits the heat exchanger. The inlet air conditions are identical for all segments. As in the liquid-coupled condenser, the length of the de-superheating segment is calculated by setting the outlet conditions as being saturated vapor, and the final phase-change segment length is calculated by setting the outlet conditions as being saturated liquid.

3.3.3.1 Segment Heat Duty Calculations: *ε-NTU* Method

The effectiveness-*NTU* method is used to calculate the segment heat duties in the air-coupled condenser. A thermal resistance network is employed to calculate the value of *UA* for each segment. The specific heat of the air-water mixture $c_{p,air}$ is calculated using the 'Air-H2O' function. The effectiveness in unmixed-unmixed cross-flow heat exchange is given as Eq. 106 and is used in the case when the refrigerant is single-phase (Incropera *et al.* 2007). The effectiveness in the de-superheating segment with NTU = 0.7772 and C_r = 0.7615 is calculated as ε = 0.4389.

$$\varepsilon_{\text{single-phase}} = 1 - \exp\left[\left(1/C_{\text{R}}\right) NTU^{0.22} \left\{ \exp\left(-C_{\text{R}} NTU^{0.78}\right) - 1 \right\} \right] \qquad (106)$$

The remaining calculations are the same as for the liquid-coupled condenser (Eqs. 50-58) except that the air stream replaces the liquid flow. For the condensing segment under consideration: UA = 238.5 W/K and $C_{\min}$ = 198.5 W/K yielding NTU = 1.218; ε = 0.704 and $Q_{\max}$ = 2.276 kW yielding Q_{seg} = 1.603 kW.

3.3.3.2 Segment Property Change Calculations

Heat transfer and pressure drop calculations for each segment are carried out assuming the average segment properties. The refrigerant and air pressure drops are calculated as described above, and the outlet pressure for the refrigerant and air in each segment are calculated by Eq. 107. With $P_{refg,in}$ = 1299 kPa and ΔP_{refg} = 3.61 kPa, $P_{refg,out}$ = 1296.39 kPa; with $P_{air,in}$ = 101.313 kPa and ΔP_{air} = 0.013 kPa, $P_{air,out}$ = 101.3 kPa.

$$P_{out} = P_{in} - \Delta P \tag{107}$$

The refrigerant outlet enthalpy is calculated based upon the known inlet conditions, the known mass flow rate, and the calculated segment heat duty, as was shown in Eq. 61: $h_{refg,in}$ = 237.3 kJ/kg, $\dot{m}_{refg}$ = 0.0411 kg/s, Q_{seg} = 1.603 kW yielding $h_{refg,out}$ = 198.3 kW. The segment refrigerant outlet temperature is calculated as a function of the outlet pressure and enthalpy: $T_{refg,out} = f(P_{refg,out}, h_{refg,out})$ = 49.29°C. It is assumed that there is no de-humidification of the air across the condenser as energy is being transferred to the ambient air stream, not removed from it; therefore the humidity ratio of the air at the outlet is the same as at the inlet. Any change in enthalpy is therefore reflected in a change in air temperature. The air outlet enthalpy is calculated by Eq. 108. With $h_{air,in}$ = 80.49 kJ/kg, $\dot{m}_{air}$ = 0.1887 kg/s, and Q_{seg} = 1.603 kW, $h_{air,out}$ = 88.99 kJ/kg.

$$h_{air,out} = h_{air,in} + Q_{seg} / \dot{m}_{air} \tag{108}$$

The air outlet temperature is calculated using the 'Air-H_2O' function in EES from the known enthalpy, pressure, and humidity ratio. The 'Air-H_2O' function is based on the psychrometric property relations from Hyland and Wexler (1983). With ω = 0.01652, $T_{air,out}$ = 45.96°C.

$$T_{air,out} = T\left(h_{out}, P_{out}, \omega_{out}\right) \tag{109}$$

3.3.4 Other Heat Exchanger Calculations

The total heat duty of the air-coupled condenser is calculated using Eq. 64: Q_{ACC} = 7.360 kW. The total height of the heat exchanger is calculated using Eq. 110: with 2 passes of heights $h_{pass\ 1}$ = 0.2613 m and h_{pass2} = 0.274 m, h_{HX} = 0.5353 m.

$$h_{HX} = \sum_{i=1}^{n} \left(N_{t,refg} t_{h,o,refg} \right)_i + \left(N_c c_h \right)_i, \qquad n = \text{number of passes} \tag{110}$$

The mass of the air-coupled condenser m_{ACC} is determined by considering the density of the heat exchanger construction material, which in this investigation is aluminum, ρ_{HX} = 2702 kg/m^3 and the volume of the heat exchanger material V_{ACC} = 7.63 × 10^{-4} m^3: m_{ACC} = 2.061 kg. The total volume of the heat exchanger consists of the total volume of the tubes minus the space occupied by the refrigerant plus the total volume occupied by the fin structure.

$$V_{ACC} = \left(t_{refg,h,o} t_{refg,w,o} - t_{refg,h,i} w_{p,refg} N_{p,refg} \right) L_t N_{t,refg} + N_c \left(f_t c_h c_w L_t / f_p \right) \tag{111}$$

$$m_{ACC} = V_{ACC} \rho_{HX} \tag{112}$$

The mass of refrigerant contained in the air-coupled condenser is calculated using the same procedure described in Eqs. 68-72. The total refrigerant charge for the air-coupled condenser is $m_{refg,ACC}$ = 0.0643 kg, whereas in the liquid-coupled condenser, it was 0.022 kg.

3.4. Air-Coupled Evaporator

The air-coupled evaporator model calculates the heat rejected from a conditioned space air stream to the refrigerant and the outlet conditions for the air and refrigerant. The air-coupled evaporator is similar in construction to the air-coupled condenser. It

consists of micro-channel flat tubes oriented parallel to one another, separated by multi-louvered fin structures that serve to enhance the air-side heat transfer. Like the air-coupled condenser, the refrigerant and air are oriented in cross-flow. The basic layout of the air-coupled evaporator is shown in Figure 17. The air-coupled evaporator model, like the other heat exchanger models, is segmental. The heat exchanger consists of two main sections: the evaporating section and the superheating section. As before, the evaporating section is divided into multiple segments and the single-phase superheating section is modeled as one segment. The various aspects of the air-coupled evaporator model have already been described in the sections for the other heat exchangers. The basic geometry and area calculations are identical to those in the air-coupled condenser model. The refrigerant pressure drop and heat transfer coefficient calculations are identical to those in the liquid-coupled evaporator model. The air-side pressure drop and heat transfer coefficient calculations are identical to those given in the air-coupled condenser description. As in the other models, a thermal resistance network is used to calculate a value of UA for each segment, which is then used in the ε-NTU method to calculate the heat duty for the given segment. The change in property calculations are the same as described for the air-coupled condenser with one exception.

There is the possibility that in cooling the conditioned space air stream, there would be condensation of water vapor out of the humid air. Since the desired air delivery temperature for every system investigated in this study is below the dew point of the air stream (21.85°C given an air inlet temperature of 37.78°C and 40% relative humidity) condensation occurs. Thus, the outlet air-water mixture will be saturated; it will have a relative humidity of unity. The outlet temperature of the conditioned space air stream is

then calculated using the 'AirH2O' function based on the known outlet temperature, pressure, and relative humidity. To implement the *ε-NTU* method while accounting for the heat transfer required to condense water vapor out of the humid air stream in addition to the sensible cooling, an effective specific heat for the air stream is calculated using Eq. 113, assuming that the maximum heat transfer possible would occur if the air outlet temperature were equal to the refrigerant inlet temperature, resulting in the lowest possible air enthalpy. The values provided for the example calculations are for a phase-change segment from a representative air-coupled evaporator model.

$$\begin{aligned} h_{\text{air,in}} &= f\left(T_{\text{air,in}}, P_{\text{air,in}}, rh_{\text{in}}\right) = f\left(37.78^{\circ}\text{C, 101.3 kPa, 40\%}\right) = 80.49\,\text{kJ/kg} \\ h_{\text{air,out,min}} &= f\left(T_{\text{refg,in}}, P_{\text{air,in}}, rh_{\text{out}}\right) = f\left(8.006^{\circ}\text{C, 101.3 kPa, 100\%}\right) = 24.81\,\text{kJ/kg} \\ C_{\text{p,air,effective}} &= \left(h_{\text{air,in}} - h_{\text{air,out,min}}\right) \Big/ \left(T_{\text{air,in}} - T_{\text{refg,in}}\right) = 1.87\,\text{kJ/kg-K} \end{aligned} \tag{113}$$

3.5. Liquid-Air Heat Exchanger

Liquid-air heat exchangers are used either for cooling air using evaporator-side liquid coupling or to reject heat from condenser-side coupling liquid to the ambient air stream. The secondary fluid-air heat exchanger is also modeled as a micro-channel tube, multi-louvered fin cross-flow heat exchanger. In a distributed cooling system, liquid flows from the evaporator to the liquid-air heat exchanger, through the pump, and finally back to the evaporator to reject the heat transferred to the liquid from the air. Conversely, liquid could flow from the condenser, through a pump, through a high-temperature air-coupled heat exchanger to reject heat to the ambient environment, then back to the condenser. The required inputs for this component model are liquid mass flow rate, inlet temperature and pressure, fluid concentration (by mass % for ethylene-glycol), air-stream volumetric flow rate, humidity ratio (assuming humidified air), inlet temperature and pressure. As in the other heat exchanger models, detailed geometric information is

required. The basic orientation is the same as that given for the other air-coupled heat exchangers, shown in Figure 17. The liquid routing through the heat exchanger is either multiple parallel tubes in a single pass, multiple parallel tubes with many passes, or serpentine tube routing. The model in this study considers multiple parallel tubes in a single pass. The liquid-side modeling is the same as described for the other liquid-coupled heat exchangers. Likewise, the air-side modeling is the same as described for the other air-coupled heat exchangers. Because the liquid is single phase throughout the entire heat exchanger, there is little change in the liquid properties. Therefore, only a single segment is employed in this model. The heat duty for the segment is calculated using the effectiveness-*NTU* method previously described, making use of a thermal resistance network. All of the calculations described for the other heat exchangers, including mass, total surface area, total heat duty, and fluid outlet temperatures and pressures, are calculated in this model.

3.6. Compressor

The compressor's role in the vapor-compression system is to increase the pressure of the refrigerant, thereby increasing its saturation temperature, which allows the refrigerant to reject heat to the ambient cooling stream through condensation. The function of the compressor model in this study is to calculate realistic values for the power consumed by the compressor and the refrigerant outlet state properties, especially temperature. Two models are considered in this study. The first is a purely thermodynamic model, which assumes a value for the isentropic efficiency of the compressor. This is the model that is used in the system models. It is used for simplicity as the primary focus of the present study is to determine the effect the different system

configurations. The second is a thermo-physical model from Duprez *et al.* (2007), which utilizes information available in a manufacturer's technical data sheet to calculate consumed power, mass flow rate, and outlet refrigerant conditions. Discussion of this model is included here because it could possibly be incorporated into a system model if desired. The model seeks to represent the internal processes of the refrigerant compression. Use of this model would allow one to account for the effect of a particular compressor design if detailed operational data were not available. Additionally, this model would allow one to consider the effects of changing such parameters as shaft speed.

3.6.1 Basic Isentropic Efficiency Model

In the isentropic efficiency model, an isentropic efficiency for the compressor is assumed. This is a value that is determined empirically for a given compressor operating at certain conditions. Isentropic efficiency data are often available in tabular or graphic form as a function of compressor pressure ratio, fluid volumetric flow rate, and compressor speed. No experimental analysis of compressors was carried out in this study; therefore, either assumed representative values or values calculated from the Duprez *et al.* (2007) model are used. The calculations for the basic model are given below with example values from a compressor that serves a representative system with evaporator temperature of 8°C (with a saturation pressure of 387.9 kPa), a superheating value of 5°C, and a condenser refrigerant saturation temperature of 50°C (with a saturation pressure of 1319 kPa).

The enthalpy and entropy of the refrigerant at the compressor inlet are calculated as a function of the inlet temperature and pressure. It is known that for an isentropic

compressor, Eq. 114 holds. With $s_{in} = s(T_{in}, P_{in}) = s(13°C, 387.9\ kPa) = 0.9437$ kJ/kg-K, $s_{out,isentropic} = 0.9437$ kJ/kg-K; $h_{in} = h(T_{in}, P_{in}) = h(13°C, 387.9\ kPa) = 259.7$ kJ/kg.

$$s_{out,isentropic} = s_{in} \tag{114}$$

The desired system high-side pressure, P_{high}, is already known; this is assumed to be the compressor outlet temperature, P_{out}. The refrigerant outlet enthalpy in the isentropic case is calculated then from the outlet pressure and isentropic entropy: $h_{out,isentropic} = 285.8$ kJ/kg.

$$h_{out,isentropic} = h\left(P_{out}, s_{out,isentropic}\right) \tag{115}$$

The actual refrigerant outlet enthalpy is calculated by Eq. 116 assuming a value for the isentropic efficiency, η_s. Setting $\eta_s = 0.7$, $h_{in} = 259.7$ kJ/kg, $h_{out,actual} = 297$ kJ/kg.

$$h_{out,actual} = h_{in} + \frac{\left(h_{out,isentropic} - h_{in}\right)}{\eta_s} \tag{116}$$

The actual outlet temperature and entropy are then calculated as a function of the discharge pressure and actual discharge enthalpy. $T_{out} = 68.61°C$, $s_{out} = 0.977$ kJ/kg-K.

$$\begin{aligned} T_{out} &= T\left(h_{out,actual}, P_{out}\right) \\ s_{out} &= s\left(h_{out,actual}, P_{out}\right) \end{aligned} \tag{117}$$

The power consumed by the compressor is calculated by Eq. 118, with the value of the refrigerant mass flow rate $\dot{m}$ dictated by the system requirements. With $\dot{m} = 0.0411$ kg/s, $W_{comp} = 1.534$ kW.

$$W_{comp} = \dot{m}\left(h_{out,actual} - h_{in}\right) \tag{118}$$

3.6.2 Thermo-physical Compressor Model

Dupez *et al.* (2007) sought to develop a reciprocating compressor model that was simple yet representative of the internal compression processes to be used in global heat pump models. The model uses parameters that appear in technical data sheets to

calculate the refrigerant mass flow rate and consumed power. Slight modifications have been made for clarity and for extension to the current study. The compression process is divided into three parts, which are illustrated in Figure 20: (i-1) isenthalpic pressure drop in the suction valve; (1-2) isobaric heating from a fictitious wall at wall temperature T_w; and (2-3) isentropic compression. The heat transfer from the fictitious wall to the refrigerant serves

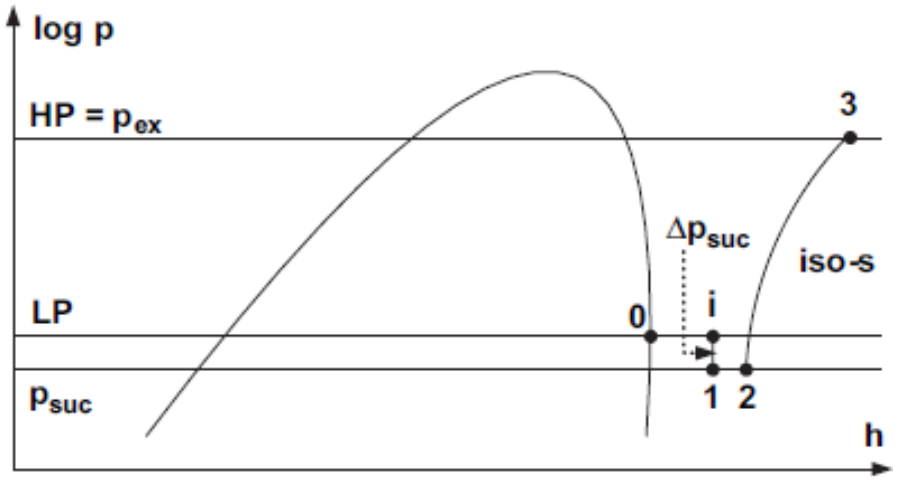

Figure 20: Diagram of the Three Part Compression Process, from Dupez *et al.* (2007)

to account for the deviation of the compression process from the ideal, isentropic case. The parameters required in the model are the suction line diameter d_{suc}, the value of UA for the isobaric heating process, the compressor rotation speed N, the swept volume V_s, the ratio between the dead space and the swept volume ε, and the fictitious wall temperature T_w. The unknown variables d_{suc}, ε, and UA are determined by comparing model output with known performance results from a technical data sheet. The solution of this model is carried out by solving the given equations simultaneously in EES. The model description is aided with values from a representative compressor, a Carlyle Model

06DR109, a semi-hermitic reciprocating compressor. Performance data are taken from Carlyle technical data (Carlyle Compressor Company 2009).

Assuming known refrigerant compressor inlet conditions T_i (7.23°C) and P_i (377.7 kPa), the inlet enthalpy h_i (254.6 kJ/kg), entropy s_i (0.9277 kJ/kg-K), and density ρ_i (18.47 kg/m^3) can be determined for R-134a as previously described. The inlet valve coefficient d_{suc} is calculated using Eq. 119 assuming a known value for the pressure drop in the suction valve Δp_{suc}. A nominal value of 5 kPa is used, as suggested by Duprez *et al.* if the value is unknown. With $\dot{m}$ = 0.05972 kg/s, d_{suc} = 0.0133 m.

$$\dot{m} = \pi d_{suc}^2 / 4\sqrt{2\Delta p_{suc}\rho_i} \tag{119}$$

Assuming the expansion across the suction valve is isenthalpic, the thermodynamic properties at point 1 can be calculated from the enthalpy and pressure. P_1 = 372.7 kPa, h_1 = 254.6 kJ/kg, T_1 = 7.08°C, and s_1 = 0.9287 kJ/kg-K.

$$\begin{aligned} h_1 &= h_i \\ T_1 &= T\left(h_1, P_1\right) \\ P_1 &= P_i - \Delta p_{suc} \end{aligned} \tag{120}$$

The temperature after the isobaric heating process (1-2) is determined by considering Eq. 121. As suggested by Duprez *et al.*, T_w = 50°C. With T_2 = 20.71°C and P_2 = 372.7 kPa, h_2 = 267.1 kJ/kg, $\Delta T_{log,suc}$ = 35.67°C, and UA_{suc} = 20.97 W/K.

$$\begin{aligned} UA_{suc}\Delta T_{log\,suc} &= \dot{m}\left(h_2 - h_1\right) \\ h_2 &= h\left(T_2, P_2\right) \\ \Delta T_{log\,suc} &= \left(T_w - T_1\right) - \left(T_w - T_2\right) / \ln\left(T_w - T / T_w - T_2\right) \end{aligned} \tag{121}$$

The mass flow rate $\dot{m}$ is calculated using Eq. 122, where ρ_2 is the density at state point 2 calculated as a function of the temperature and pressure. With ρ_2 = 17 kg/m^3 and $\dot{V}_{vc}$ = 3.51 × 10^{-3} m^3/s, $\dot{m}$ is calculated as 0.05972 kg/s.

$$\dot{m} = \rho_2 \dot{V}_{vc} \tag{122}$$

The circulated volume flow rate $\dot{V}_{vc}$ is calculated using Eq. 123, where V_c is the circulated volume as illustrated in Figure 21 and N is the rotational speed of the compressor. V_c = 1.204 × 10^{-4} m^3 and N = 1750 rpm, yielding $\dot{V}_{vc}$ = 3.51 × 10^{-3} m^3/s.

$$\dot{V}_{vc} = V_c N/60 \tag{123}$$

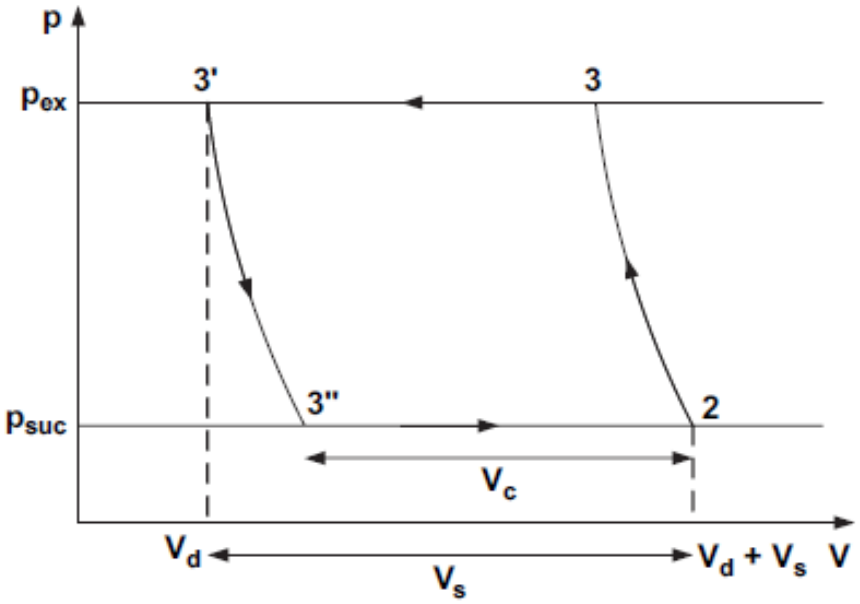

Figure 21: Crank Diagram for the Compression Process, from Dupez *et al.* (2007)

The circulated volume is calculated by Eq. 124, where V_d is the volume of the dead space and V_s is the swept volume of the compressor, and ε is the ratio between the dead volume and the swept volume. V_s = 1.415 × 10^{-4} m^3 and i$_d$ = 8.95 × 10^{-6} m^3 leading to V_2 = 1.504 × 10^{-4} m^3. With $V_{3''}$ = 2.99 × 10^{-5} m^3, V_c = 1.204 × 10^{-4} m^3 and ε = 0.06325.

$$V_c = V_2 - V_{3''}$$
$$V_2 = V_d + V_s = \varepsilon V_s + V_s \tag{124}$$

The swept volume is calculated from known compressor geometry: the number of cylinders $N_{cylinders}$ (2), the stroke length l_{stroke} (34.9 mm) and the bore diameter d_{Bore} (50.8 mm). $V_s = 1.415 \times 10^{-4}$ m^3.

$$V_s = N_{cylinders} l_{stroke} \pi {d_{Bore}}^2 / 4 \tag{125}$$

The volume at point 3'' is calculated from the known mass of refrigerant $m_{3''}$ and the known density of the refrigerant. $m_{3''} = 5.099 \times 10^{-4}$ kg, $\rho_{3''} = 17.001$ kg/m^3 yielding $V_{3''} = 2.99 \times 10^{-5}$ m^3.

$$V_{3''} = m_{3''} / \rho_{3''} \tag{126}$$

The expansion process from point 3' to 3'' is considered isentropic; therefore the density at point 3'' is calculated as a function of pressure and entropy. $P_{3''} = P_{suc} = 372.7$ kPa, $s_{3''} = s_{3'} = 0.9723$ kJ/kg-K, $\rho_{3''} = 17.001$ kg/m^3.

$$\begin{aligned} P_{3''} &= P_{suc} \\ s_{3''} &= s_{3'} \\ \rho_{3''} &= \rho\left(P_{3''}, s_{3''}\right) \end{aligned} \tag{127}$$

The entropy at point 3' is calculated as a function of the known pressure and density. $P_{3'} = P_{high\text{-}side} = 1282$ kPa, $\rho_{3'} = \rho_3 = 56.98$ kg/m^3, $s_{3'} = 0.9723$ kJ/kg-K.

$$\begin{aligned} P_{3'} &= P_{high\text{-}side} \\ \rho_{3'} &= \rho_3 \\ s_{3'} &= s\left(P_{3'}, \rho_{3'}\right) \end{aligned} \tag{128}$$

The density at point 3 is calculated by assuming the overall compression process (2-3) as isentropic. With $s_3 = s_2 = 0.9723$ kJ/kg-K, $P_3 = 1282$ kPa, $\rho_3 = 56.98$ kg/m^3.

$$\begin{aligned} P_3 &= P_{\text{high-side}} \\ s_3 &= s_2 \\ \rho_3 &= \rho\left(P_3, s_3\right) \end{aligned} \tag{129}$$

The mass at point 3'' is calculated using Eq. 130. With V_d = 8.95 × 10^{-6} m^3 and $\rho_{3'}$ = 56.98 kg/m^3, $m_{3''}$ = 5.099 × 10^{-4} kg.

$$m_{3''} = \rho_{3'} V_d \tag{130}$$

The refrigerant outlet temperature T_3 and enthalpy h_3 are obtained from the calculated outlet pressure and entropy. The power consumed by the compressor is calculated using Eq. 131. With s_3 = 0.9723 kJ/kg-K and P_3 = 1282 kPa, h_3 = 294.8 kJ/kg and T_3 = 66.03°C. $W_{\text{compressor}}$ = 2.40 kW.

$$W_{\text{compressor}} = \dot{m}\left(h_3 - h_i\right) \tag{131}$$

The values of the ratio of the dead space to swept volume ε and the temperature at point 2 T_2 are calculated by equating the calculated values of mass flow rate and consumed power with the values reported in the technical data sheet of the actual compressor, which are given in Table 4. The isentropic efficiency of the total compression process η_s is calculated by Eq. 132. $s_{s,3}$ = 0.9277 kJ/kg-K, $h_{s,3}$ = 280 kJ/kg yielding η_s = 0.6307.

$$\begin{aligned} s_{s,3} &= s_i \\ h_{s,3} &= h\left(s_{s,3}, P_3\right) \\ \eta_s &= \left(h_{s,3} - h_i\right) / \left(h_3 - h_i\right) \end{aligned} \tag{132}$$

Table 4: 06DR109 Compressor Data (2009)

Saturated Suction Temperature	7.232° (45°F)	Flow Rate	0.05972 kg/s (474 lb/hr)	*N*	1750
Saturated Delivery Temperature	48.89° C (120°F)	Stroke	34.9 mm	Bore	50.8 mm
Power	2.4 kW				

3.7. Pump and Fan

The pump and fan models calculate the required power to overcome the pressure losses in the liquid loops and air streams, respectively. As the goal of this study is primarily to evaluate high-level system performance, the models for the pump and fan are simplistic. As mentioned, the pump does work on the liquid, an ethylene-glycol/water mixture. Hydronic fluid properties are determined using the 'BRINEPROP2' function in EES, which is based on equations and data from the IIR/IIF handbook on secondary refrigerants (Melinder 1997). The fan does work on the air streams, both ambient-side and conditioned space-side. As in the other models, the air properties are calculated using the 'AirH_2O' function in EES.

The pressure drops in the various stream or loops are known from the heat exchanger and line-loss models. Therefore, this value is treated as an input for the pump/ fan model. The volumetric flow rate of the working fluid is calculated using Eq. 133 with the density calculated using the appropriate function. For a liquid pump with $\dot{m}$ = 0.2922 kg/s and ρ = 1029 kg/m^3, $\dot{V}$ = 2.84 × 10^{-4} m^3/s.

$$\dot{V} = \dot{m}/\rho \tag{133}$$

The ideal pumping power required to overcome the pressure loss ΔP is calculated using Eq. 134. With ΔP = 83.6 kPa, W_{ideal} = 0.0237 kW.

$$W_{ideal} = \dot{V}\Delta P \tag{134}$$

Using an assumed value for the pump/ fan efficiency, the actual power consumed by the pump/fan is calculated by Eq. 135. With η = 0.6, W_{actual} = 0.0396 kW.

$$W_{actual} = W_{ideal}/\eta \tag{135}$$

The change in temperature of the working fluid due to the power input is calculated using Eq. 136 for the air stream and Eq. 137 for the liquid loop. For the liquid stream with W_{actual} = 0.0396 kW, $\dot{m}$ = 0.2922 kg/s, c_p = 3.905 kJ/kg-K, and T_{in} = 8°C, T_{out} = 8.035°C.

$$\begin{aligned} h_{air,out} &= h_{air,in} + W_{actual} / \dot{m}_{air} \\ T_{air,out} &= T\left(P_{air,out}, h_{air,out}\right) \end{aligned} \tag{136}$$

$$T_{liq.,out} = T_{liq.,in} + \dot{W}_{actual} \Big/ \left(\dot{m}_{liq.} c_{p,liq.}\right) \tag{137}$$

3.8. Single Phase Line

The single-phase line model calculates the change in temperature and pressure, and heat loss or gain associated with a line that transports a single-phase fluid between components within the system. The required inputs for the model are fluid inlet temperature and pressure, ambient air temperature, the position of the line in relation to other system components, the geometry and physical properties of the line, and any insulation employed. Figure 22 shows a diagram of the basic line design showing the fluid, tube, insulation, and ambient environment. Like the heat exchanger models, a thermal resistance network is used to determine a *UA* value for the line; this network is also shown in Figure 22. The effectiveness-*NTU* method is then used to calculate the heat gain/loss and subsequent working fluid property changes. The single-phase working fluid pressure drop and heat transfer coefficient modeling are the same as those described for the heat exchanger models.

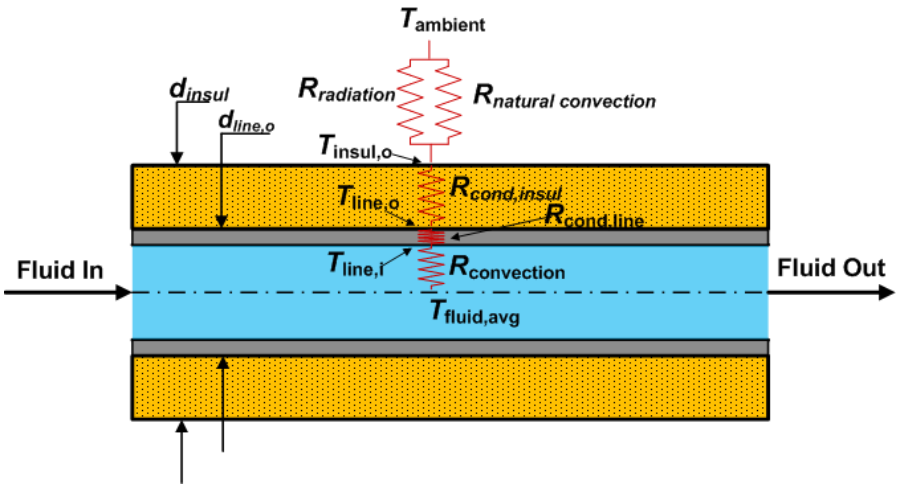

Fig 22: Schematic of the Line Model

The change in temperature across the length of the line is obtained by representing the line as a system of thermal resistances. There are resistances dues to: forced convection from the fluid to the line wall, conduction across the line wall and the insulation, and natural convection and radiation from the external surface of the insulation. It should be noted that in these calculations, the line is assumed to be located in an environment that may be approximated as quiescent air. The model description is illustrated by considering a representative 0.5 m line located between the evaporator outlet and the compressor inlet. The refrigerant inlet temperature and pressure are 10.06°C and 349 kPa, and the refrigerant mass flow rate is 0.0875 kg/s. The ambient air temperature is 35°C, and the tube outer diameter is 12.7 mm with a wall thickness of 0.812 mm and insulation thickness of 6.35 mm.

3.8.1 Forced Convection Heat Transfer

Forced-convection heat transfer occurs between the internally flowing fluid and the tube wall. The Prandtl number, Pr_{fluid}, and thermal conductivity for the fluid, k_{fluid}, are calculated at the average temperature and pressure. Churchill's (1977a) Nusselt number correlation is used to determine the fluid heat transfer coefficient, where d_i is the

inside diameter of the line. With Re = 889,153, f = 0.01736, Pr = 0.7894, k = 0.01299 W/m-K, and d_i = 0.01107 m, Nu = 1570 and h_{forced} = 1841 W/m^2-K.

$$Nu = \left(4.364^{10} + \left(\frac{e^{((2200-\mathrm{Re})/365)}}{4.364^2} + \frac{1}{\left(6.3 + 0.079\left(\frac{f}{8}\right)^{0.5} \mathrm{Re}\frac{\mathrm{Pr}}{\left(1+\mathrm{Pr}^{0.8}\right)^{\frac{5}{6}}} \right)^2} \right)^{-5} \right)^{1/10} \tag{138}$$

$$h_{\text{forced}} = \frac{Nu_{\text{forced}} k}{d_i} \tag{139}$$

The thermal resistance for the internal forced convection is calculated using Eq. 140. $R_{internal}$ = 0.0312 K/W.

$$R_{\text{internal}} = 1/\left(\pi h_{\text{forced}} d_i L\right) \tag{140}$$

3.8.2 Conduction Heat Transfer

The conduction thermal resistance takes into account the conduction heat transfer across the line material and the insulation. The diameter of the pipe and the insulation is calculated using Eq. 141. With d_o = 12.7 mm and t_{insul} = 6.35 mm, d_{insul} = 25.4 mm.

$$d_{\text{insul}} = \left(d_o + 2t_{\text{insul}}\right) \tag{141}$$

The temperature of the line is required to calculate the thermal conductivity of the line. The thermal conductivity of the line is determined from the EES function 'k' for the line material. Due to the iterative nature of the necessary calculations, the temperature of the line is determined simultaneously with the rest of the calculations. The thermal resistance due to conduction across the line is calculated using Eq. 142. With k_{line} = 236.2 W/m-K, $R_{cond,line}$ = 0.00018 K/W.

$$R_{\text{cond,line}} = \ln\left(d_o/d_i\right)/\left(2\pi L k_{\text{line}}\right) \tag{142}$$

The line is assumed to be insulated with cellular glass pipe insulation. The thermal conductivity of the insulation is calculated at the average insulation temperature using the 'k' conductivity function in EES. The thermal resistance due to conduction across the insulation is calculated using Eq. 143. With k_{insul} = 0.05613 W/m-K, $R_{cond,insul}$ = 3.931 K/W.

$$R_{cond,insul} = \ln\left(d_{insul}/d_o\right)/\left(2\pi L k_{insul}\right) \tag{143}$$

3.8.3 Natural Convection and Radiation Heat Transfer

The heat transfer from the surface of the insulation to the ambient occurs in parallel heat transfer modes of natural convection and radiation. To determine the properties of air required for natural convection calculations, the surface film temperature is calculated using Eq. 144. The surface temperature, T_{surf}, needed here is the temperature of the outside surface of the insulation, thus $T_{surf} = T_{insul,o}$. This temperature is dependent on the calculated heat loss or gain across the line length; therefore, it is obtained iteratively. With T_{amb} = 35°F and T_{surf} = 25.21°C, $T_{surf,film}$ = 30.1°C.

$$T_{surf,film} = \left(T_{amb} + T_{surf}\right)/2 \tag{144}$$

From the film temperature and the ambient pressure, the Prandtl number, dynamic viscosity, thermal conductivity, volumetric thermal expansion coefficient, and density of the air surrounding the line are determined. From this information, the kinematic viscosity is calculated according to Eq. 145. With $\mu_{air} = 1.873 \times 10^{-5}$ kg/m-s and ρ_{air} = 1.164 kg/m^3, $\nu_{air} = 1.609 \times 10^{-5}$ m^2/s.

$$\nu_{air} = \mu_{air}/\rho_{air} \tag{145}$$

The Grashof number is calculated using Eq. 146,

$$Gr_{air} = g\beta_{air}\left|T_{amb} - T_{surf}\right| {d_{insul}}^3/\nu_{air}^2 \tag{146}$$

where g is the average acceleration due to gravity. With $\beta_{air} = 0.00330\ K^{-1}$, $Gr_{air} = 20055$. The Rayleigh number is then calculated using Eq. 147. With $Pr_{air} = 0.7268$, $Ra_{air} = 14576$.

$$Ra_{air} = Pr_{air}\, Gr_{air} \tag{147}$$

The Nusselt number for natural convection is calculated using Eq. 148, which is applicable for long horizontal cylinders with $Ra_D \leq 10^{12}$ (Churchill and Chu 1975). $Nu_{nat} = 4.799$.

$$Nu_{nat} = \left(0.60 + \frac{0.387 Ra_{air}^{1/6}}{\left[1 + \left(0.559 / Pr_{air} \right)^{9/16} \right]^{8/27}} \right)^2 \tag{148}$$

The heat transfer coefficient for the natural convection is calculated from this Nusselt number using Eq. 149. With $k_{air} = 0.0259$ W/m-K, $h_{nat} = 4.892$ W/m^2-K.

$$h_{nat} = Nu_{nat} k_{air} / d_{insul} \tag{149}$$

The thermal resistance due to natural convection is calculated using Eq. 150: $R_{nat} = 5.124$ K/W.

$$R_{nat} = 1 / \pi h_{nat} d_{insul} L \tag{150}$$

For the radiation heat transfer calculations, the temperature of the surroundings is assumed to be equal to the ambient air temperature, thus $T_{surr} = 308.15$ K. The heat transfer coefficient for radiation is calculated using Eq. 151,

$$h_{rad} = \varepsilon \sigma \left(T_{surf} + T_{surr} \right) \left(T_{surf}^2 + T_{surr}^2 \right) \tag{151}$$

where the emissivity of the surface of the insulation, ε, is assumed to be 0.8 and the Stefan-Boltzmann constant, $\sigma = 5.67 \times 10^{-8}$ W/m^2-K^4: $h_{rad} = 5.061$ W/m^2-K. The thermal resistance due to radiation is calculated using Eq. 152: $R_{rad} = 4.952$ K/W.

$$R_{rad} = 1 / \pi h_{rad} d_{insul} L \tag{152}$$

3.8.4 Total Thermal Resistance and Heat Gain

The total thermal resistance for the network containing the line and the insulation is calculated using Eq. 153: R_{total} = 6.48 K/W.

$$R_{total} = R_{internal} + R_{cond,line} + R_{cond,insul} + \frac{1}{\left(1/R_{nat} + 1/R_{rad}\right)} \tag{153}$$

The log mean temperature difference for the line is calculated using Eq. 154. Because the refrigerant outlet temperature is dependent on the pressure drop and heat gain/loss, the value of *LMTD* is also obtained iteratively: *LMTD* = 25.2°C.

$$LMTD = \frac{\left(\left(T_{amb} - T_{out}\right) - \left(T_{amb} - T_{in}\right)\right)}{\ln\left(\left(T_{amb} - T_{out}\right)/\left(T_{amb} - T_{in}\right)\right)} \tag{154}$$

The heat gained or lost by the fluid across the line is calculated using Eq. 155: Q = 3.9 W or 0.0039 kW.

$$Q = LMTD/R_{total} \tag{155}$$

The outlet temperature of the fluid is calculated using the sequence given in Eq. 156 for R-134a and the sequence given in Eq. 157 for the coupling liquid. If the refrigerant temperature is lower than the ambient temperature, the sign on the heat transfer term is positive (+); if the refrigerant temperature is higher than the ambient temperature, the sign on the heat transfer term is negative (-). In the example case, the refrigerant temperature (10.06°C) is lower than the ambient temperature (35°C). With h_{in} = 258 kJ/kg and P_{out} = 328.9 kPa, h_{out} = 258.044 kJ/kg and T_{out} = 9.54°C.

$$\begin{aligned} h_{out} &= \pm\left(Q/\dot{m}_{refg}\right) + h_{in} \\ T_{out} &= T\left(h_{out}, P_{out}\right) \end{aligned} \tag{156}$$

$$T_{out} = \pm\left(Q/\left(\dot{m}_{liq} c_{p,liq}\right)\right) + T_{in} \tag{157}$$

The temperature of the inside surface of the line is calculated using Eq. 158, where the sign convention for the heat transfer term is as described above: $T_{line,i}$ = 9.924°C.

$$T_{\text{line,i}} = \pm R_{\text{internal}} Q + T_{\text{fluid, avg}} \tag{158}$$

The temperature of the outside surface of the line, which is also the inside surface of the insulation, is calculated using Eq. 159: $T_{\text{line,o}} = 9.925°\text{C}$.

$$T_{\text{line,o}} = \pm R_{\text{conduction,line}} Q + T_{\text{line,i}} \tag{159}$$

Due to the high thermal conductivity of aluminum, the temperature drop across the tube wall is negligible. The temperature of the outside surface of the insulation, which is exposed to the environment, is calculated using Eq. 160: $T_{\text{insul,o}} = 25.21°\text{C}$.

$$T_{\text{insul,o}} = \pm R_{\text{conduction,insul}} Q + T_{\text{line,o}} \tag{160}$$

As stated above, these tube wall and insulation temperatures are used iteratively both for material thermal conductivity calculations, as well as the natural convection and radiation heat transfer coefficient calculations.

3.9. Two Phase Line

The two-phase line procedure calculates the changes in temperature and pressure, heat loss or gain, and change in phase associated with a line that transports a two-phase fluid between components within a system. The two-phase line procedure is identical to the single-phase line procedure except that the pressure drop is calculated based on the two-phase pressure drop and heat transfer coefficient correlations previously described. If the temperature of the fluid in the line is lower than the ambient temperature, heat is gained by the fluid and a flow boiling heat transfer coefficient correlation is used. If the temperature of the fluid is higher than the ambient temperature, heat is transferred from the fluid to the ambient environment and a convective condensation correlation is employed.

3.10 Heat Exchanger Design and System Modeling Procedures

This section describes the procedures used for the design of the various heat exchangers used in this study, with a focus on how the design calculations are conducted to meet the specific requirements imposed on the heat exchangers by the system. The procedure for incorporating these heat exchanger designs into system models is then described.

3.10.1 Heat Exchanger Design Procedure

Each of the systems modeled in this study has certain specified operating conditions, such as ambient temperature, ambient pressure, and air flow rates. There are also certain design goals for each system, including desired evaporator air outlet temperature, and closest approach temperatures between the various working fluids. The previously described heat exchanger models are used to determine the heat exchanger geometry and heat exchanger configuration that best meets the design goals within the specified operating conditions. Figure 23 depicts a flow chart of this heat exchanger design procedure.

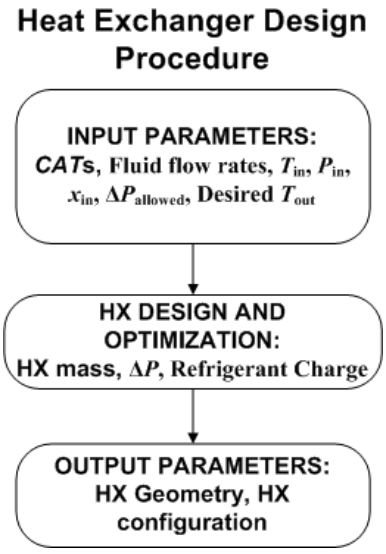

Figure 23: Heat Exchanger Design Procedure

As can be seen in this figure, for the purposes of heat exchanger design, the model input parameters include fluid inlet temperatures and pressures, refrigerant inlet quality, desired fluid flow rates, desired closest approach temperatures, and desired fluid outlet temperatures. The heat exchanger geometry, including tube size, number of tubes, fin size and number of fins, may be optimized with respect to heat exchanger mass, fluid pressure drop or refrigerant charge. As soon as the required geometry is determined, it is fixed and the heat exchanger design is incorporated into the system model.

3.10.2 System Modeling Procedure

A flow chart of the system modeling procedure is shown in Figure 24. Once the geometric designs for each of the required heat exchangers have been fixed, these designs, along with the various fluid flow rates, ambient temperature, condenser refrigerant pressure, and evaporator refrigerant pressure, and component efficiencies serve as the inputs for the system models. With these inputs and the heat exchanger and other component models previously described, the performance of the system is iteratively solved in *EES*. The output parameters of the system models are conditioned space outlet temperatures, condenser-side outlet temperatures, fluid pressure drops, consumed power, heat duties, and the coefficient of performance. It is important to stress that in the system models, the conditioned space air outlet temperature is not specified, but rather it is calculated through the interaction of the working fluids across the heat exchangers of specified geometry.

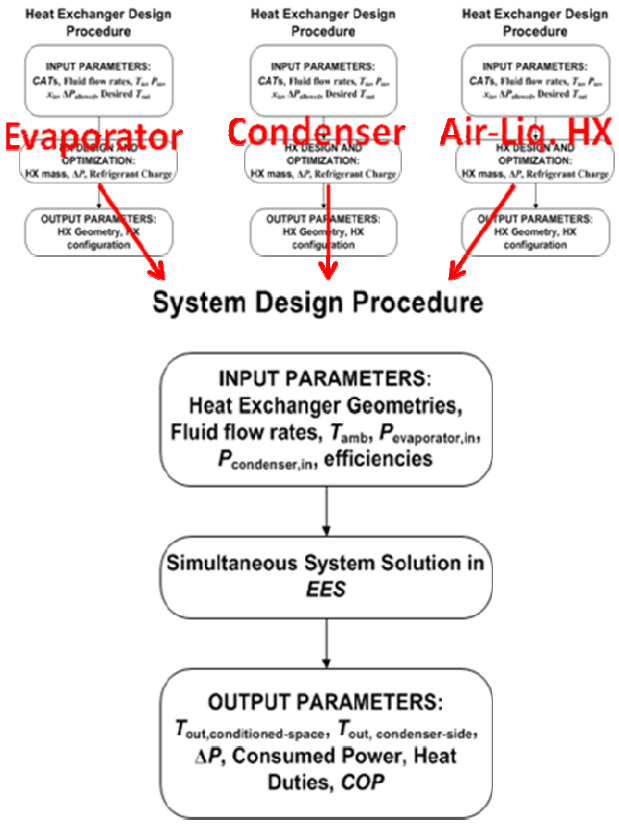

Figure 24: Example System Modeling Procedure

CHAPTER 4

SYSTEM RESULTS

Simulations of four systems are presented here for the purpose of determining the suitability of hydronically coupled cooling systems to automotive use. Systems with and without liquid-coupling are presented. Input parameters, operating conditions, and predicted results are presented for each system. The four systems considered are:

- System 1 consists of an air-coupled evaporator, an air-coupled condenser, a compressor, a condenser-side fan, an evaporator-side blower, a flow control device, and the connecting refrigerant lines. This is the typical automotive air-conditioning system design.
- System 2 consists of a conditioned-space air-to-liquid heat exchanger, a liquid-coupled evaporator, a liquid-coupled condenser, a condenser-side liquid-to-air heat exchanger, a compressor, an evaporator-side liquid pump, a condenser-side liquid pump, a condenser-side fan, an evaporator-side blower, a flow control device, and the connecting refrigerant and liquid lines. This is a completely liquid-coupled system that would provide the ability to isolate the refrigerant containing components and locate them in any desired location.
- System 3 consists of two air-coupled evaporators that are configured in parallel refrigerant flow, an air-coupled condenser, a compressor, two evaporator-side blowers, a condenser-side fan, a flow control device, and the connecting refrigerant lines. The evaporators in this system are assumed to be spatially distributed such that one is located near the compressor and condenser, while the second evaporator is located some distance away from the other major

components. This necessitates the use of long refrigerant containing lines for the second evaporator.

- System 4 seeks to address the thermal management problem addressed by System 3 of multiple spatially distributed heat loads through the use of hydronic fluid coupling. Therefore, System 4 consists of two air-to-liquid heat exchangers that are configured in parallel flow on the same hydronic fluid loop, a liquid-coupled evaporator, an air-coupled condenser, a compressor, two conditioned-space-side blowers, a condenser-side fan, a conditioned-space-side liquid pump, a flow control device, and the required refrigerant and liquid lines. In System 4, the distributed heat loads are served by liquid-carrying lines instead of refrigerant carrying lines.

4.1. System Descriptions and Results

4.1.1 System 1: Air-Coupled Condenser, Air-Coupled Evaporator

System 1 consists of an air-coupled condenser and an air-coupled evaporator. This is the typical automotive air-conditioning system. A schematic of System 1 is shown in Figure 25. Heat is transferred from the conditioned-space air stream to the refrigerant across the air-coupled evaporator and is transferred to the ambient air stream across the air-coupled condenser. The input parameters for System 1 are shown in Table 5. The ambient air temperature is assumed to be 37.78°C (100°F). It is assumed that the conditioned-space air stream volumetric flow rate is 300 ft^3/min (0.1416 m^3/s), driven by the blower motor. The condenser-side air stream volumetric flow rate is chosen to be 1800 ft^3/min (0.849 m^3/s), which would be driven by a combination of ram air and condenser-side fan. The desired conditioned-space air delivery temperature is set at 15.05°C. This temperature is not specified in the models; it is allowed to vary based on

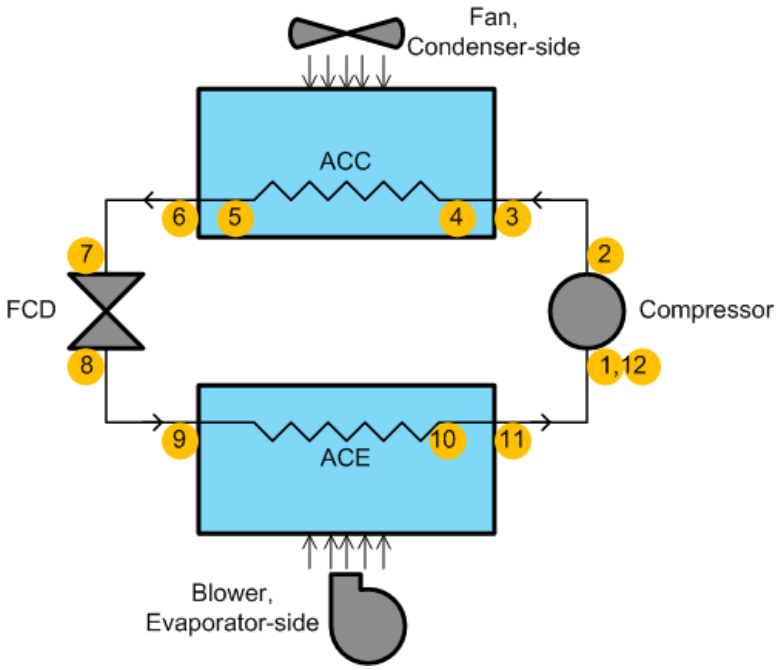

Figure 25: Schematic of System 1: Air-Coupled Condenser and Evaporator

Table 5: System 1 Input Parameters and Design Points

T_{amb}	37.78°C	$\dot{V}_{air,evap}$	300 cfm (0.1416 m^3/s)	$CAT_{evap,desired}$	4°C
t_{wall}	0.81 mm	$\dot{V}_{air,cond}$	1800 cfm (0.8485 m^3/s)	$CAT_{cond,desired}$	4°C
$OD_{line,2-3}$	12.7 mm	$L_{line,2-3}$	0.5 m	$\Delta T_{subcool,\ desired}$	3°C
$OD_{line,6-7}$	7.94 mm	$L_{line,6-7}$	3 m	$\Delta T_{superheat,desired}$	5°C
$OD_{line,8-9}$	12.7 mm	$L_{line,8-9}$	0.5 m	$ID_{air-duct}$	50.8 mm
$OD_{line,11-1}$	12.7 mm	$L_{line,11-1}$	3 m	$L_{air-duct}$	2 m

the individual heat exchanger designs and calculations. It is presented here as a desired outlet temperature that guides fixed values of other system variables. This temperature is arrived at using a basic thermodynamic model of an automobile passenger compartment subject to an ambient environment of 37.78°C (100°F) with 40% relative humidity and a

750 W/m^2 solar irradiance. System 1 is modeled using the previously described segmental heat exchanger models, single-phase and two-phase line loss models, and the compressor and fan/blower models. The heat exchangers for this system are designed to achieve closest approach temperatures between the refrigerant and air-streams of 4°C, a 5°C refrigerant superheating exiting of the evaporator, and a 3°C refrigerant sub-cooling exiting the condenser. The evaporator in System 1 is assumed to be located 3 m distant from the other major components of the vapor-compression system; therefore, the 7.94 mm *OD* line between the condenser and the flow control device and the 12.7 mm *OD* line between the evaporator and the compressor are 3 m long. The value of 3 m is used as this is assumed to be a representative length of refrigerant line that would be required to connect the condenser outlet, which is located at the front of the engine compartment, to the expansion device located near the evaporator, which is directly adjacent to the passenger compartment. This assumed value is used in place of a calculated length of line because no detailed component layout with respect to engine compartment is employed in this study. The other lines, from the compressor to the condenser and form the flow control device to the evaporator are 12.7 mm in outside diameter and 0.5 m long. There is assumed to be an air-delivery network consisting of four parallel air ducts to deliver the conditioned air to the passenger space after it exits the evaporator. Each duct is 2 m long and has a hydraulic diameter of 50.8 mm. A schematic of this air-distribution system is shown in Figure 26.

A summary of the system results is shown in Table 6, and a pressure versus enthalpy diagram for the refrigerant in System 1 is shown in Figure 27. The actual conditioned-space air delivery temperature is 15.0°C with refrigerant superheating and

sub-cooling values of 5.01°C and 3.04°C, respectively. The total evaporator cooling duty is 6.2 kW, with a total compressor and fan/blower power consumption of 1.166 kW, resulting in a *COP* of 3.74. The compressor, with a pressure ratio of 3.35 and refrigerant mass flow rate of 0.0434 kg/s consumed 1.64 kW. With a pressure drop across the evaporator and air-distribution network of 160 Pa, 11.3 W are required by the blower to drive the 0.142 m^3/s evaporator side air flow. On the condenser air side, where there is

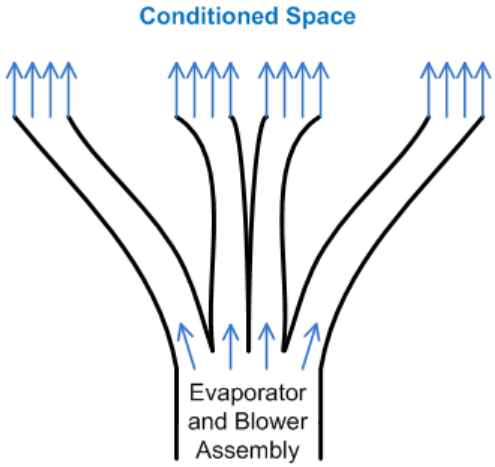

Figure 26: Schematic of Conditioned Air Distribution System

Table 6: System 1 Results Summary

$T_{air,delivered,evap}$	15.0°C	$CAT_{evap,actual}$	3.87°C	$\Delta T_{superheat,actual}$	5.01°C
$T_{air,out,cond}$	45.9°C	$CAT_{cond,actual}$	4.06°C	$\Delta T_{subcool,actual}$	3.04°C
Q_{evap}	6.2 kW	Q_{cond}	7.9 kW	$W_{compressor}$	1.64 kW
$W_{blower,evap}$	11.3 W	$W_{fan,cond}$	5.8 W	*COP*	3.74
$P_{cond,in}$	1313 kPa	$P_{evap,in}$	430 kPa	$P_{comp,in}$	391 kPa
Pressure ratio	3.35				

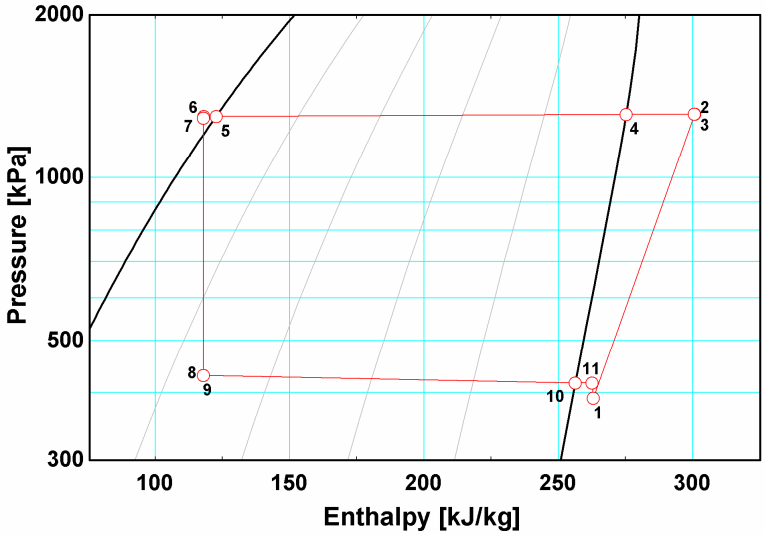

Figure 27: p-h Diagram for System 1, with an Air-Coupled Condenser and an Air-Coupled Evaporator

no ducting network, the condenser fan consumes 5.8 W to overcome a pressure drop of 13.6 Pa. Additional vehicle-specific details will govern actual values of these power consumptions. A summary of the heat exchanger designs required to achieve these results is shown in Table 7. Detailed heat exchanger design data is provided for both the air-coupled condenser and air-coupled evaporator in Table 8. From Table 7 and from Figure 28, a comparison of heat exchanger face areas, it can be seen that the condenser size is larger than the evaporator. Though the refrigerant heat transfer coefficients are comparable for the evaporator and condenser, averaging 2,590 W/m^2-K and 2,790 W/m^2-K, respectively, the air-side heat transfer coefficients are different, averaging 77 W/m^2-K and 180 W/m^2-K for the evaporator and condenser, respectively. The condenser is required to dissipate more heat (7.9 kW) than the evaporator (6.2 kW). This results in a condenser with a larger mass (2.06 kg versus 1.74 kg) that requires a larger refrigerant charge (0.064 kg versus 0.028 kg). The log mean temperature difference (LMTD) for the

Table 7: System 1 Air-Coupled Heat Exchanger Design Summary

	h_{total}	L_{total}	$A_{c,total}$	m_{hx}	UA_{total}
ACC	0.535 m	0.442 m	0.237 m^2	2.06 kg	982 W/K
ACE	0.412 m	0.361 m	0.149 m^2	1.74 kg	453 W/K
	ΔP_{air}	ΔP_{refg}	V_{refg}	Refg. Charge	
ACC	13.1 Pa	10.8 kPa	2.43 x 10^{-4} m^3	0.0643 kg	
ACE	0.6 Pa	13.5 kPa	3.13 x 10^{-4} m^3	0.0284 kg	
$\Delta P_{11\text{-}1}$	26 kPa	Refg. Charge, Lines	0.122 kg	$\dot{m}_{refg}$	0.0434 kg/s

condenser is 7.39°C, while the LMTD for the evaporator is 12.25°C. The additional heat duty requirement and the lower available driving temperature difference in the condenser contribute to the larger thermal conductance requirement in the condenser, leading in turn to the larger condenser face area. The evaporator air side heat transfer coefficient (the dominant resistance) is considerably lower than the condenser air-side heat transfer coefficient, which would indicate a large surface area requirement. However, because of the latent heat load component in the evaporator, the larger thermal capacity rate of the evaporator air stream transfers larger heat duties for a given temperature change, with the combined effects of these different factors leading to an evaporator smaller than the condenser in this case.

Table 8: System 1 Heat Exchanger Design Details

	$t_{refg,h,o}$	$t_{refg,w,o}$	$t_{refg,t}$	$N_{p,refg}$	$w_{p,refg}$
ACC	1 mm	25.4 mm	0.15 mm	28	0.7 mm
ACE	1 mm	50.8 mm	0.15 mm	56	0.7 mm
	$N_{t,pass\ 1}$	$N_{t,pass\ 2}$	c_h	c_w	f_p
ACC	20	20	12.7 mm	25.4 mm	1.27 mm
ACE	15	16	12.7 mm	50.8 mm	2.31 mm
	f_t	θ	l_w	l_i	
ACC	0.127 mm	30°	1.14 mm	22.86 mm	
ACE	0.127 mm	30°	1.14 mm	22.86 mm	

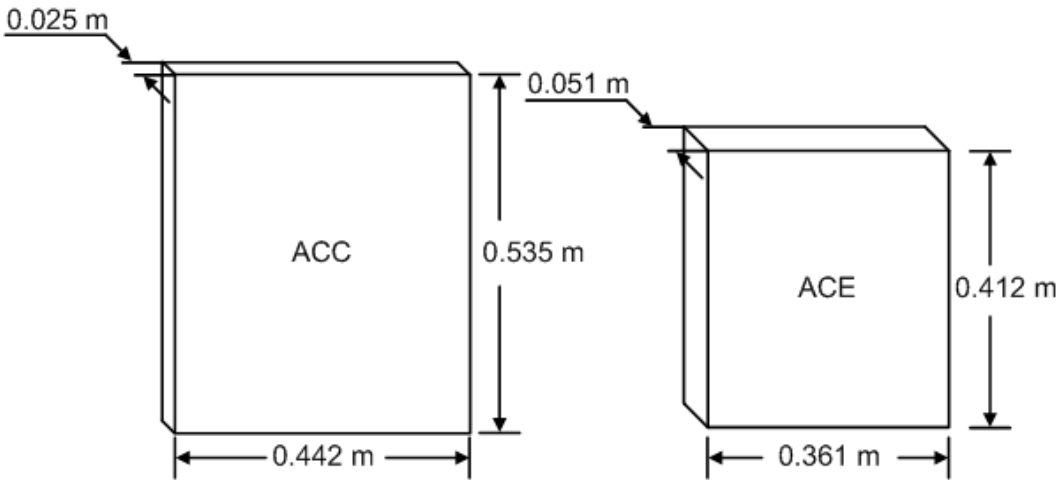

Figure 28: System 1 Heat Exchanger Face Areas

The effect of the distance between the evaporator and the other major system components is to lower the compressor inlet pressure. This is due to the refrigerant pressure drop of 26 kPa across the evaporator discharge line, from point 11 to 1 on the system schematic. This is clearly seen on the pressure versus enthalpy diagram as the vertical distance between points 11 and 1. Increasing the distance between the evaporator and the other major components, especially the compressor inlet, has several effects,

which are summarized in Table 9. The evaporator discharge line pressure drop increases, which in turn lowers the compressor inlet pressure. This raises the required pressure ratio for a given compressor discharge pressure, which requires a greater compressor power, resulting in a diminished coefficient of performance. Increasing the effective line length through other pressure reducing devices such as line bends, changes in diameter, or valves would have a similar effect.

Table 9: System 1 Variation with Changing Line Length

$L_{Line,11-1}$ (m)	ΔP_{11-1} (kPa)	Refg. Charge, Lines (kg)	*COP*	*Pressure ratio*	$W_{compressor}$ (kW)
3	26	0.122	3.74	3.36	1.64
5	48	0.195	3.72	3.95	1.85
7	70	0.268	3.09	4.23	1.96
10	106	0.377	2.81	4.79	2.16

4.1.2 System 2: Liquid-Coupled Condenser, Liquid-Coupled Evaporator

System 2 consists of a liquid-coupled condenser, a liquid-coupled evaporator, and liquid-air heat exchangers on both the condenser side and the evaporator side. This is the system that might be employed if a "sealed vapor compression package" is desired. A schematic of System 2 is shown in Figure 29. Heat is transferred from the conditioned-space air stream to the evaporator-side liquid loop, which transfers heat to the refrigerant across the liquid-coupled evaporator. The high temperature refrigerant transfers heat to the condenser-side liquid loop across the liquid-coupled condenser, and finally the heat is transferred to the ambient air stream across the condenser-side air-liquid heat exchanger. As in System 1, an air-distribution ducting system, as shown in Figure 26, is used to deliver the conditioned air to the passenger space. The input parameters for System 2 are shown in Table 10. The ambient air is again assumed to be at 37.78°C and 40% relative

humidity, and the conditioned-space air volumetric flow rate is again 300 ft^3/min (0.142 m^3/s), while the condenser-side air stream volumetric flow rate is again 1800 ft^3/min (0.549 m^3/s). The liquid flow rate in both the evaporator-side and condenser-side liquid loops is 4.5 gpm (2.84×10^{-4} m^3/s). The desired conditioned-space air delivery temperature is also 15.05°C. System 2 is also modeled using the segmental heat exchanger models, and single-phase refrigerant, two-phase refrigerant, and coolant line loss models. The heat exchangers in this system are designed to achieve liquid-air closest approach temperatures of 3°C; however the presence of the liquid loops requires an additional temperature difference between the liquid and the refrigerant. The desired closest approach temperatures for the counter-flow liquid-coupled condenser and evaporator are 2°C. As in System 1, the desired levels of refrigerant superheating and sub-cooling are 5°C and 3°C, respectively. As in System 1, the conditioned space air delivery point, thus the conditioned space heat exchanger, are assumed to be located 3 m distant from the other major components of the system; however, in System 2, this spatial displacement is achieved through the use of extended coolant lines instead of refrigerant carrying lines. The refrigerant containing components are assumed to all be centrally located, immediately adjacent to one another. The hydronic fluid contained in the liquid loops is a water/ propylene-glycol mixture with 30% propylene-glycol by mass. At this concentration and ambient pressure, the hydronic fluid has a boiling point of 102.2°C and a freezing point of -13.08°C.

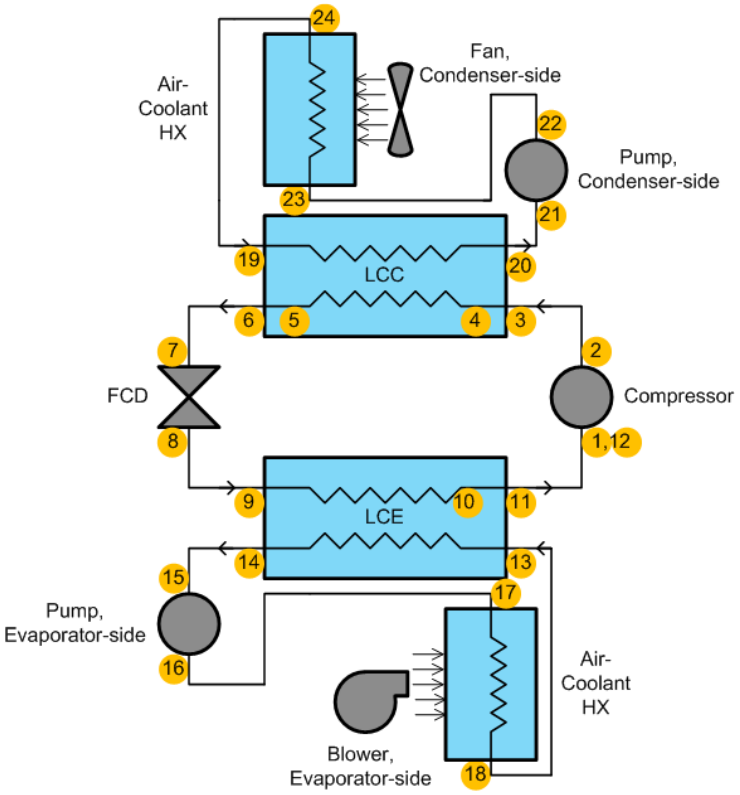

Figure 29: Schematic of System 2: Liquid-Coupled Condenser and Evaporator

A summary of the system results is shown in Table 11, and a pressure versus enthalpy diagram for the refrigerant in System 2 is shown in Figure 30. The actual conditioned-space air delivery temperature is 15.04°C with refrigerant superheating and sub-cooling values of 5.00°C and 2.97°C, respectively. The total conditioned-space cooling duty is 6.15 kW, with a total compressor, pump and fan power consumption of 2.19 kW, resulting in a *COP* of 2.81. The System 2 cooling duty is slightly lower than that for System 1 (6.2 kW); however, the System 2 *COP* is lower than that for System 1 (3.74) due mostly to the increase in consumed power. In System 2, the pressure ratio is 4.27 and the compressor consumes 2.1 kW, which is 28% larger than System 1 (1.64 kW). This difference is due to the lower evaporator pressure (360.8 kPa compared with 430 kPa for System 1) and higher condenser pressure (1492 kPa compared with 1313 kPa

for System 1) required to accommodate the evaporator-side and condenser-side liquid coupling. The addition of the liquid loops also adds two liquid pumps, which consume 55 W and 14 W on the evaporator and condenser side, respectively. The power consumed by the blower (11.3 W) and fan (5.3 W) is comparable to the corresponding values for System 1 (11.3 W for blower and 5.8 W for fan).

Table 10: System 2 Input Parameters and Design Points

T_{amb}	37.78°C	$\dot{V}_{air,evap\text{-}side}$	300 cfm (0.142 m^3/s)	$CAT_{a\text{-}l,\ evap,desired}$	4°C
$\Delta T_{superheat,desired}$	5°C	$\dot{V}_{liq.,evap\text{-}side}$	4.5 gpm (2.84×10^{-4} m^3/s)	$CAT_{l\text{-}r,\ evap,desired}$	2°C
$\Delta T_{subcool,\ desired}$	3°C	$\dot{V}_{liq.,cond\text{-}side}$	4.5 gpm (2.84×10^{-4} m^3/s)	$CAT_{r\text{-}l,\ cond,desired}$	2°C
$x_{liq,evap}$	30%	$\dot{V}_{air,cond\text{-}side}$	1800 cfm (0.549 m^3/s)	$CAT_{l\text{-}a,\ cond,desired}$	5°C
$x_{liq,cond.}$	30%	t_{wall}	0.81 mm	$OD_{liq.}$	19.05 mm
$L_{line,2\text{-}3}$	0.5 m	$OD_{line,2\text{-}3}$	12.7 mm	$L_{line,18\text{-}19}$	3 m
$L_{line,6\text{-}7}$	0.5 m	$OD_{line,6\text{-}7}$	7.94 mm	$L_{line,16\text{-}17}$	3 m
$L_{line,8\text{-}9}$	0.5 m	$OD_{line,8\text{-}9}$	12.7 mm	$L_{line,22\text{-}23}$	0.5 m
$L_{line,11\text{-}1}$	0.5 m	$OD_{line,11\text{-}1}$	12.7 mm	$L_{line,24\text{-}19}$	0.5 m
$ID_{air\text{-}duct}$	50.8 mm	$L_{air\text{-}duct}$	2 m		

Table 11: System 2 Results Summary

$T_{air,delivered,cold}$	15.04°C	$CAT_{a\text{-}l,evap,actual}$	3.03°C	$CAT_{l\text{-}r,evap,actual}$	1.98°C
$T_{air,out,hot}$	45.98°C	$CAT_{r\text{-}l,cond,actual}$	1.99°C	$CAT_{l\text{-}a,cond,actual}$	3.11°C
$\Delta T_{superheat,actual}$	5.00°C	$\Delta T_{subcool,actual}$	2.97°C	*COP*	2.81
$Q_{HX,evap\text{-}side}$	6.15 kW	Q_{evap}	6.21 kW	Q_{cond}	8.31 kW
$Q_{HX,cond\text{-}side}$	8.32 kW	$W_{pump,evap\text{-}side}$	55 W	$W_{pump,cond\text{-}side}$	14 W
$W_{compressor}$	2.1 kW	$W_{blower,evap\text{-}side}$	11.3 W	$W_{fan,cond\text{-}side}$	5.3 W
$P_{cond,in}$	1492 kPa	$P_{evap,in}$	360.8 kPa	$P_{comp,in}$	349.7 kPa
Pressure ratio	4.27				

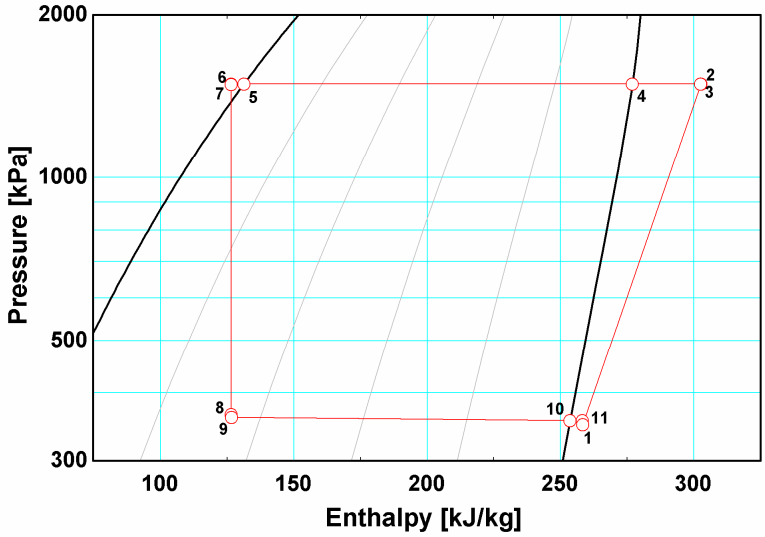

Figure 30: p-h Diagram for System 2, with a Liquid-Coupled Condenser and a Liquid-Coupled Evaporator

A summary of the heat exchanger designs required to achieve these results is shown in Table 12. Design details for the air-coupled heat exchangers are provided in Table 13, while design details for the liquid-coupled evaporator and liquid-coupled condenser are provided in Table 14. Figure 31 presents a comparison of the heat exchanger face areas for System 2. Again, the required size of the condenser-side air-coupled heat exchanger is larger than the evaporator-side air-coupled heat exchanger. The hot-side and cool-side liquid heat transfer coefficients are again comparable at 2,420 W/m^2-K and 2,250 W/m^2-K, respectively, while the air heat transfer coefficients are again different at 160 W/m^2-K and 90 W/m^2-K, respectively. The difference in size is

Table 12: System 2 Heat Exchanger Design Summary

	h_{total}	L_{total}	$A_{c,total}$	m_{HX}	UA_{total}
Air-Liq HX, Evap.-side	0. 467 m	0. 419 m	0.196 m^2	1.46 kg	420 W/K
LCE	0.041 m	0.394 m	-	1.02 kg	1480 W/K
LCC	0.049 m	0.454 m	-	2.11 kg	1560 W/K
Air-Liq HX, Cond.-side	0.549 m	0.554 m	0.304 m^2	2.26 kg	1050 W/K
	$\Delta P_{refg.}$	ΔP_{air}	$\Delta P_{liq.}$	V_{refg}	Charge, refg.
Air-Liq HX, Evap.-side	-	0.49 Pa	70.8 kPa	-	-
LCE	6.70 kPa	-	54.8 kPa	2.16 x 10^{-4} m^3	0.0194 kg
LCC	0.51 kPa	-	12.5 kPa	4.49 x 10^{-4} m^3	0.103 kg
Air-Liq HX, Cond.-side	-	6.25 Pa	27.2 kPa	-	-
$\Delta P_{11\text{-}1}$	5.81 kPa	Refg. Charge, Lines	0.028 kg	$\dot{m}_{refg}$	0.04746 kg/s

due to the higher heat transfer rate required of the condenser-side heat exchanger (8.32 kW) than of the evaporator-side heat exchanger (6.15 kW). The liquid-coupled condenser is also larger than the liquid-coupled evaporator; the liquid-coupled condenser consists of more tubes, has wider tubes, and is longer. In this case, the condenser does have a higher heat duty (8.31 kW compared with 6.21 kW for the evaporator); however, the average refrigerant heat transfer coefficient is lower for the condenser at 1,090 W/m^2-K as compared with 2,960 W/m^2-K for the evaporator, though liquid heat transfer coefficients are comparable at 2,420 W/m^2-K for the condenser and 2,250 W/m^2-K for the evaporator.

Table 13: System 2 Air-to-Liquid Heat Exchanger Design Details

	$t_{liq,h,o}$	$t_{liq,w,o}$	$t_{liq,t}$	$N_{port,liq}$	$w_{p,liq}$
Cond. Side	1 mm	25.4 mm	0.15 mm	28	0.7 mm
Evap. Side	1 mm	25.4 mm	0.15 mm	28	0.7 mm
	N_t	c_h	c_w	f_p	f_t
Cond. Side	20	12.7 mm	25.4 mm	1.27 mm	0.127 mm
Evap. Side	35	12.7 mm	25.4 mm	1.59 mm	0.127 mm
	θ	l_w	l_i		
Cond. Side	30°	1.14 mm	22.86 mm		
Evap. Side	30°	1 mm	22.86 mm		

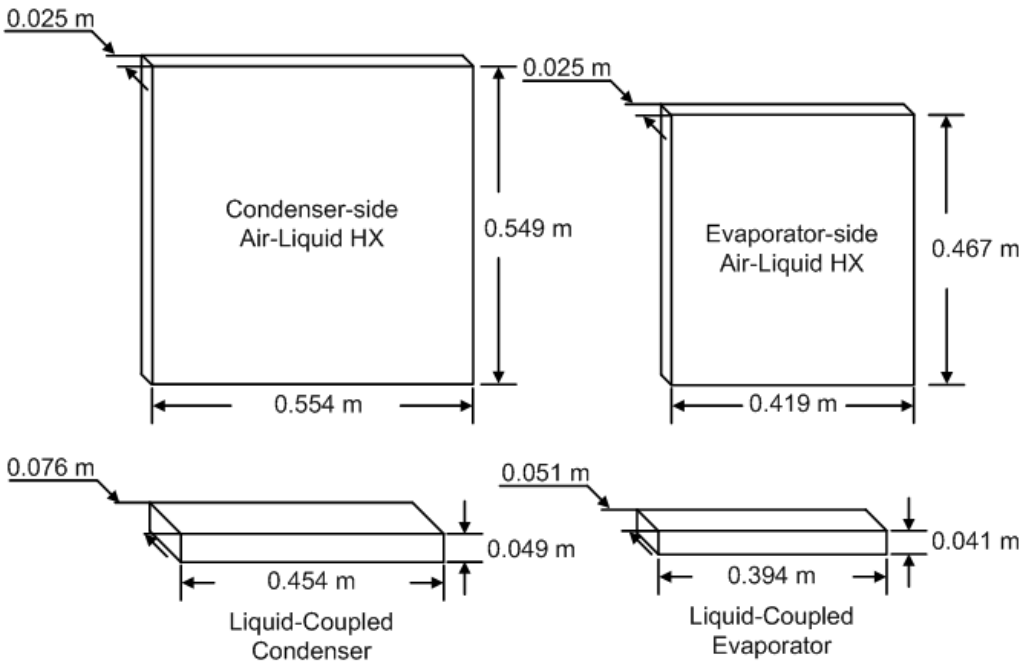

Figure 31: System 2 Heat Exchanger Face Areas

Table 14: System 2 Liquid-to-Refrigerant Heat Exchanger Designs Details

	$t_{liq,h,o}$	$t_{liq,w,o}$	$t_{liq,t}$	$N_{port,liq}$	$w_{p,liq}$	$N_{t,liquid}$
LCC	1 mm	76.2 mm	0.15 mm	84	0.7 mm	25
LCE	1 mm	50.8 mm	0.15 mm	56	0.7 mm	21
	$t_{refg,h,o}$	$t_{refg,w,o}$	$t_{refg,t}$	$N_{port,refg}$	$w_{p,refg}$	$N_{t,refg}$
LCC	1 mm	76.2 mm	0.15 mm	84	0.7	24
LCE	1mm	50.8 mm	0.15 mm	56	0.7	20

The required refrigerant charge for the condenser (0.103 kg) is also larger than that required for the evaporator (0.019 kg). The liquid-coupled evaporator refrigerant charge is lower than the charge in the System 1 air-coupled evaporator (0.0284 kg); the liquid-coupled condenser has fewer tubes (20 compared with 31), which compensates for being slightly longer (0.394 m compared with 0.361 m). the liquid-coupled condenser has a larger refrigerant charge (0.103 kg) than the System 1 air-coupled condenser (0.064

kg). Though the System 2 liquid-coupled condenser has fewer refrigerant tubes (24 compared with 40 for the air-coupled condenser), it is longer at 0.454 m than the air-coupled condenser (0.442 m) and wider (76.2 mm compared with 25.4 mm). Each of these trends is due to the fact that extra heat transfer area in the liquid-coupled condenser can only be added by increasing the tube dimensions, whereas in the air-coupled condenser, heat transfer area can be effectively increased by increasing the heat-transfer-limiting air-side area by increasing the area of the fin structure. The total refrigerant charge required for the System 2 connecting lines is 0.028 kg. This is much lower than the 0.122 kg required of the connecting lines in System 1. This difference is due to the fact that the long length lines in System 2 contain liquid instead of refrigerant. For this same reason the refrigerant pressure drop between the evaporator discharge and the compressor inlet is much smaller at 5.81 kPa. The increase in liquid line length required as the conditioned-space air-to-liquid heat exchanger moves farther from the major system components increases the liquid-loop total pressure drop; this increases the required pumping power; however, this has a relatively minimal effect on the total power requirement, as shown in Table 15.

Table 15: System 2 Variation with Changing Line Length

$L_{\text{Line,16-17}}$ (m)	$\Delta P_{16\text{-}17}$ (kPa)	$\Delta P_{18\text{-}13}$ (m)	$W_{\text{pump, evap-side}}$ (W)	*COP*
3	5	4.8	55.2	2.814
5	8.4	7.8	57.9	2.811
7	11.7	11.0	60	2.807
10	16.7	15.7	64	2.802

4.1.3 System 3: Air-Coupled Condenser, 2 Air-Coupled Evaporators

System 3 consists of an air-coupled condenser and two air-coupled evaporators. This system would be employed when there are two locations that require cooling but are spatially separated. This system is essentially identical to System 1, except that an additional evaporator has been added in parallel to the original. A schematic of System 3 is shown in Figure 32. The input parameters for System 3 are shown in Table 16. These parameters are in most cases identical to those for System 1. It is important to note, though, that both conditioned-space air streams have a volumetric flow rate of 150 ft^3/min (0.071 m^3/s) so that the total evaporator air flow rate is 300 cfm (0.283 m^3/s), and the desired air delivery temperature for both is 15.05°C. This means that each of the two evaporators will transfer approximately one half the amount of heat from air to refrigerant as in System 1; therefore, the total heat duty for System 3 equal that of System 1. Due to this, the condenser-side air volumetric flow rate is the same as in System 1, 1800 cfm (0.549 m^3/s). Additionally, it is important to note that the first evaporator is assumed to be 3 m distant from the compressor and other major components, while the second evaporator is assumed to be 10 m distant. The use of the 3 m length of refrigerant line has been previously described. The length of 10 m is used for the second evaporator because no detailed orientation details for the second, distant conditioned space are employed in this study. Ten meters is assumed to be an approximate length of refrigerant line that would be required to connect the condenser outlet to the expansion device inlet for the evaporator serving a secondary conditioned space that would be much farther from the front of the vehicle, as in a tractor trailer-type configuration or a military vehicle. To ensure that each evaporator has the same refrigerant mass flow rate to achieve similar performance from each, the pressure drops in the two parallel evaporator

paths are managed to ensure they match. This is achieved by two measures, both of which are illustrated in Figure 32: using two independently configured flow control devices to ensure the evaporator inlet pressures are identical and using a second flow control device on the line connecting the closer evaporator to the mixing point to ensure that the total branch pressure drops are equal. This is described in more detail subsequently.

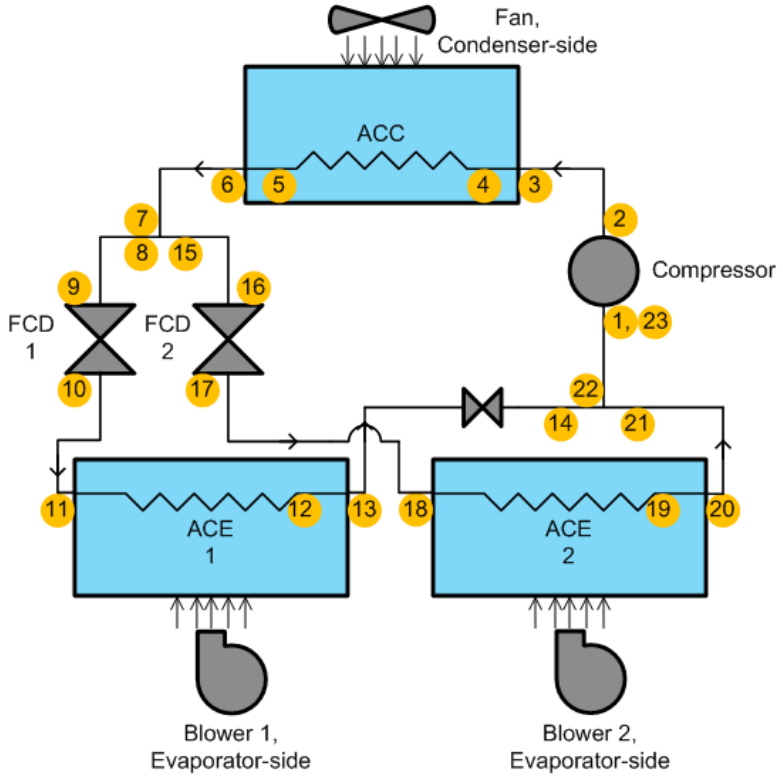

Figure 32: Schematic of System 3: Air-Coupled Condenser with 2 Air-Coupled Evaporators

Table 16: System 3 Input Parameters and Design Points

$\Delta T_{\text{superheat 1}}$	5°C	$\dot{V}_{\text{air,evap 1}}$	150 cfm (0.071 m^3/s)	$CAT_{\text{evap 1, desired}}$	4°C
$\Delta T_{\text{superheat 2}}$	5°C	$\dot{V}_{\text{air,evap 2}}$	150 cfm (0.071 m^3/s)	$CAT_{\text{evap 2, desired}}$	4°C
$\Delta T_{\text{subcool, desired}}$	3°C	$\dot{V}_{\text{air,cond-side}}$	1800 cfm (0.549 m^3/s)	$CAT_{\text{cond,desired}}$	4°C
$L_{\text{line,2-3}}$	0.5 m	$OD_{\text{line,2-3}}$	12.7 mm	t_{wall}	0.81 mm
$L_{\text{line,6-7}}$	0.5 m	$OD_{\text{line,6-7}}$	7.94 mm	T_{amb}	37.78°C
$L_{\text{line,8-9}}$	3 m	$OD_{\text{line,8-9}}$	7.94 mm	$ID_{\text{air-duct}}$	50.8 mm
$L_{\text{line,10-11}}$	0.5 m	$OD_{\text{line,10-11}}$	12.7 mm	$L_{\text{air-duct}}$	2 m
$L_{\text{line,13-14}}$	3 m	$OD_{\text{line,13-14}}$	12.7 mm		
$L_{\text{line,15-16}}$	10 m	$OD_{\text{line,15-16}}$	7.94 mm		
$L_{\text{line,17-18}}$	0.5 m	$OD_{\text{line,17-18}}$	12.7 mm		
$L_{\text{line,20-21}}$	10 m	$OD_{\text{line,20-21}}$	12.7 mm		

A summary of the system results is shown in Table 17, and a pressure versus enthalpy diagram for the refrigerant in System 3 is shown in Figure 33. The actual conditioned-space air delivery temperature for the closer evaporator is 15.04°C and 15.00°C for the farther evaporator. The cooling duties of evaporators 1 and 2 are 3.15 kW and 3.16 kW, respectively, for a total system cooling duty of 6.3 kW. The total compressor and fan power consumption of 1.67 kW results in a *COP* of 3.79. Blower 1 consumes 3.22 W, while blower 2 consumes 3.21 W, and the condenser side fan consumes 10.7 W. Because the total cooling duty is comparable to that of System 1 (6.2 kW), the refrigerant mass flow rates are similar (0.04402 kg/s for System 3 and 0.0434 kg/s for System 1). With identical pressure ratios of 3.35, the compressor power consumed in System 2 (1.65 kW) is very similar to that in System 1 (1.64 kW).

Table 17: System 3 Results Summary

$T_{\text{air,actual , evap 1}}$	15.04°C	$T_{\text{air,actual , evap 2}}$	15.00°C	$T_{\text{air,out,cond.}}$	45.8°C
$CAT_{\text{actual, evap 1}}$	3.6°C	$CAT_{\text{actual, evap 2}}$	3.7°C	$CAT_{\text{actual, cond}}$	3.67°C
$\Delta T_{\text{superheat, actual 1}}$	5.00°C	$\Delta T_{\text{superheat, actual 2}}$	5.00°C	$\Delta T_{\text{subcool, actual}}$	3.00°C
$Q_{\text{evap 1}}$	3.146 kW	$Q_{\text{evap 2}}$	3.158 kW	Q_{cond}	8.00 kW
$W_{\text{blower, evap1}}$	3.22 W	$W_{\text{blower, evap2}}$	3.21 W	$W_{\text{compressor}}$	1.65 kW
$W_{\text{fan,cond}}$	10.7 W	*COP*	3.79	*Pressure ratio*	3.35
$P_{\text{cond,in}}$	1313 kPa	$P_{\text{evap,in}}$	430 kPa	$P_{\text{comp,in}}$	392 kPa

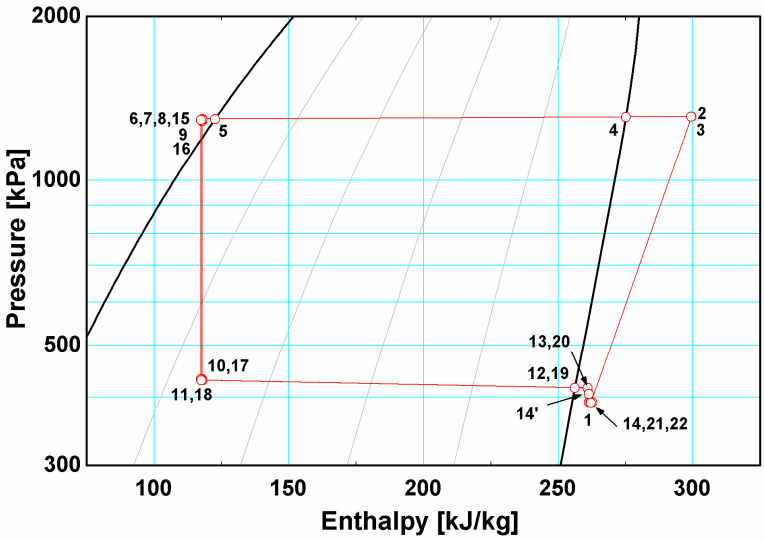

Figure 33: p-h Diagram for System 3, with an Air-Coupled Condenser and 2 Air-Coupled Evaporators

Table 18: Effect of Two Evaporators

P (kPa)	8/15	9/16	10/17	11/18	13/20	14 (14')/21
Refg. Loop 1	1298	1289	433	430	417	392 (407)
Refg. Loop 2	1298	1268	433	430	416	392
h (kJ/kg)	8/15	9/16	10/17	11/18	13/20	14 (14')/21
Refg. Loop 1	117.9	117.8	117.8	117.9	260.9	261.4 (261.4)
Refg. Loop 2	117.9	117.3	117.3	117.4	260.9	262.7

The effect of having two evaporators located at different distances from the major components is examined in Table 18. This table gives the refrigerant pressure and enthalpy at each significant location on the evaporator branches. (Identical positions on each branch are shown in the same column, such that 11/18 corresponds to the evaporator inlets for the closer branch/farther branch.) To have identical refrigerant mass flow rates through each branch, the refrigerant pressure drop across each branch must be identical. This would not normally be the case with branches that have different total lengths; therefore, certain steps are taken to minimize the difference in pressure drop between the two branches and to ensure that they meet at the same pressure. Firstly, the flow control devices are located near the evaporator inlets as opposed to near the other major components. This means that $L_{\text{line,8-9}} = 3$ m, while $L_{\text{line,15-16}} = 10$ m, but the length between each flow control device and evaporator inlet is the same, $L_{\text{line,10-11}} = L_{\text{line,17-18}} = 0.5$ m. The pressure drops from 8-9 and 15-16 yield different flow control device inlet pressures (1289 kPa for branch 1 and 1268 kPa for branch 2), but each flow control device is assumed to be configured independently to yield identical flow control device outlet pressures (433 kPa). Because the line lengths between the flow control devices

and evaporator inlets are the same, the pressure drop across them is the same for identical mass flow rates such that the evaporator inlet pressure is 430 kPa in each case. The different line lengths do lead to different line-heat losses, and these lead to slightly different refrigerant enthalpies at the evaporator inlets, and these are reflected in the slight difference in cooling duty for each evaporator. Secondly, there is a second flow control device on the closer evaporator branch towards the end of the evaporator discharge line before the mixing point. This compensates for the difference in pressure drops across the evaporator discharge lines of varying length. For evaporator 1 with an exit pressure of 417 kPa, the pressure at the mixing point would normally be 407 kPa, but it is further reduced to be equal to the pressure for branch 2 at this same location (392 kPa).

Table 19: System 3 Heat Exchanger Design Summary

	h_{total}	L_{total}	$A_{c,total}$	m_{HX}	UA_{total}
ACC	0.535 m	0.454 m	0.243 m^2	2.11 kg	1030 W/K
ACE 1	0.398 m	0.305 m	0.122 m^2	0.91 kg	235 W/K
ACE 2	0.398 m	0.31 m	0.123 m^2	0.92 kg	237 W/K
	$\Delta P_{refg.}$	ΔP_{air}	V_{refg}	Charge, refg.	
ACC	13.05 kPa	13 Pa	2.49 x 10^{-4} m^3	0.06 kg	
ACE 1	13.9 kPa	0.4 Pa	1.26 x 10^{-4} m^3	0.011 kg	
ACE 2	14.1 kPa	0.4 Pa	1.28 x 10^{-4} m^3	0.011 kg	
$\Delta P_{13\text{-}14}$	9.55 kPa	$\Delta P_{20\text{-}21}$	24.3 kPa	Refg. Charge, Lines	1.26 kg
$\dot{m}_{refg}$	0.04402 kg/s				

A summary of the heat exchanger designs required to achieve these results is shown in Table 19. Detailed design information for the three heat exchangers is provided in Table 20, while a visual comparison of the face areas is given in Figure 34. The slight difference in evaporator inlet conditions is reflected in the slight difference in the evaporator designs; the evaporator for branch 2 is slightly longer at 0.31 m compared with 0.305 m for the first evaporator. The System 3 air-coupled condenser is comparable in design to the System 1 air-coupled condenser, although in practice, due to ease of fabrication, the same size evaporator would be installed at both locations. Even though they transfer half as much heat, the two System 3 air-coupled evaporators have similar dimensions to the System 1 evaporator, except that the System 3 evaporators are each half the depth at 25.4 mm. The total mass of the two System 3 evaporators (1.84 kg) is comparable to the System 1 evaporator mass (1.74 kg). The refrigerant charges in the evaporators and condenser for System 3 are also similar to those in System 1: 0.022 kg and 0.06 kg for the System 3 evaporators and condenser, compared with 0.028 kg and 0.064 kg for the System 1 evaporator and condenser.

Table 20: System 3 Heat Exchanger Design Details

	$t_{refg,h,o}$	$t_{refg,w,o}$	$t_{refg,t}$	$N_{p,refg}$	$w_{p,refg}$
ACC	1 mm	25.4 mm	0.15 mm	28	0.7 mm
ACE 1 & 2	1 mm	25.4 mm	0.15 mm	28	0.7 mm
	$N_{t,pass\ 1}$	$N_{t,pass\ 2}$	c_h	c_w	f_p
ACC	20	20	12.7 mm	25.4 mm	1.27 mm
ACE 1 & 2	15	15	12.7 mm	25.4 mm	1.59 mm
	f_t	θ	l_w	l_i	
ACC	0.127 mm	30°	1.14 mm	22.86 mm	
ACE 1 & 2	0.127 mm	30°	1.14 mm	22.86 mm	

Because only half the total refrigerant mass flow rate passes through the long line lengths to the farther evaporator, the total pressure drop on the evaporator side of the system is very similar to the pressure drop in System 1. This is illustrated through the comparable compressor inlet pressures of 392 kPa for System 3 and 391 kPa for System 1. This leads to comparable pressure ratios and compressor power, resulting in similar coefficients of performance for System 1 (3.74) and System 3 (3.79).

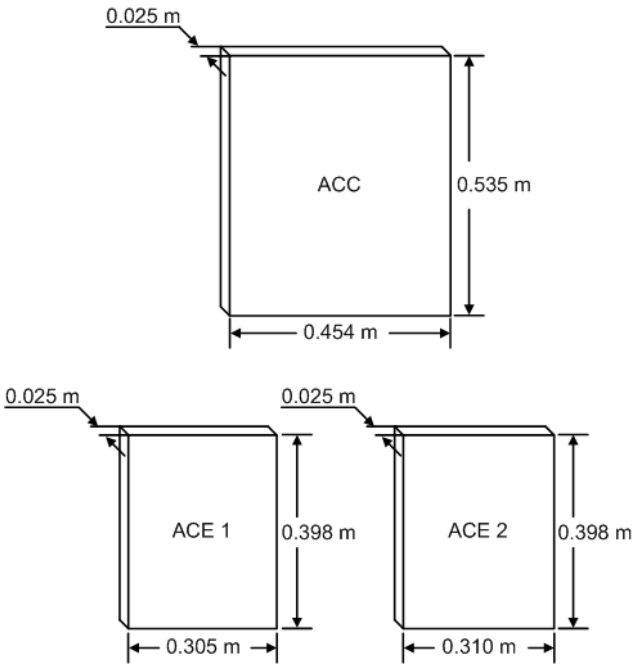

Figure 34: System 3 Heat Exchanger Face Areas

4.1.4 System 4: Air-Coupled Condenser, Liquid-Coupled Evaporator, and 2 Air-Liquid Heat Exchangers

System 4 consists of an air-coupled condenser, a liquid-coupled evaporator, and two evaporator-side air-liquid heat exchangers. This system seeks to apply the liquid-coupling concept to the multiple, spatially distributed heat source situation. Like System 2, System 4 utilizes a liquid-coupled evaporator, but there are two heat exchangers on the liquid loop instead of one. Unlike System 2, System 4 has an air-coupled condenser instead of a liquid-coupled condenser. This design is used to take advantage of possible benefits of evaporator-side liquid coupling and lower condenser-inlet pressures offered by an air-coupled condenser. This also allows for consideration of the use of liquid-coupling on one side only, which is not considered in any of the other systems discussed above. A schematic of System 4 is shown in Figure 35. The input parameters for System 4 are shown in Table 21. Like System 3, both conditioned-space air streams have a volumetric flow rate of 150 ft^3/min (0.071 m^3/s) and desired air delivery temperatures of

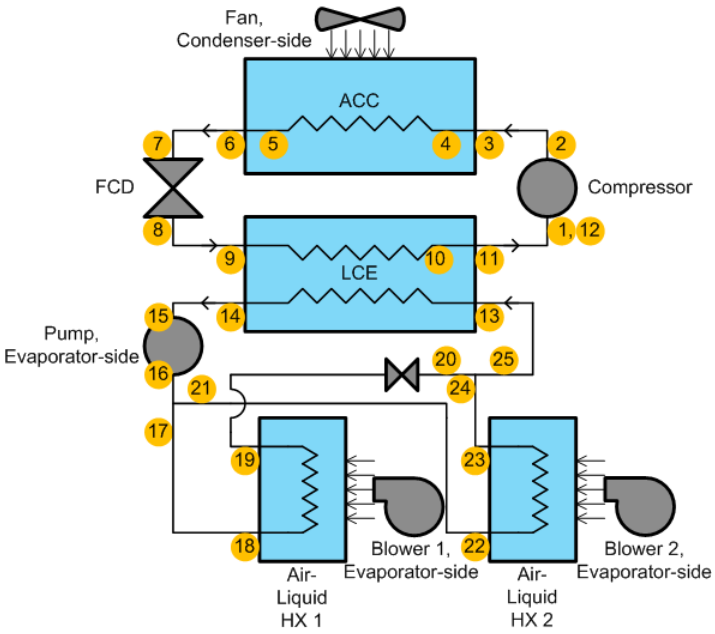

Figure 35: Schematic of System 4: Air-Coupled Condenser, Liquid-Coupled Evaporator, and 2 Air-Liquid Heat Exchangers

Table 21: System 4 Input Parameters and Design Points

T_{amb}	37.78°C	$L_{line,2-3}$	0.5 m	$OD_{line,2-3}$	12.7 mm
$\Delta T_{superheat,\ desired}$	5°C	$L_{line,6-7}$	0.5 m	$OD_{line,6-7}$	7.94 mm
$\Delta T_{subcool,\ desired}$	3°C	$L_{line,8-9}$	0.5 m	$OD_{line,8-9}$	12.7 mm
$CAT_{a-l,\ evap,\ desired\ (1\ and\ 2)}$	3°C	$L_{line,11-1}$	0.5 m	$OD_{line,11-1}$	12.7 mm
$CAT_{l-r,\ evap,desired}$	2°C	$L_{line,14-15}$	0.5 m	$OD_{liq.}$	19.05 mm
$CAT_{r-a,\ cond,desired}$	4°C	$L_{line,17-18}$	3 m	t_{wall}	0.81 mm
$\dot{V}_{air,evap-side\ 1}$	150 cfm (0.071 m^3/s)	$L_{line,19-20}$	3 m	$ID_{air-duct}$	50.8 mm
$\dot{V}_{air,evap-side\ 2}$	150 cfm (0.071 m^3/s)	$L_{line,21-22}$	10 m	$L_{air-duct}$	2 m
$\dot{V}_{liq.,evap-side}$	4.5 gpm (2.84×10^{-4} m^3/s)	$L_{line,23-24}$	10 m	$x_{liq,evap}$	30%
$\dot{V}_{air,cond-side}$	1800 cfm (0.549 m^3/s)	$L_{line,25-13}$	0.5 m		

15.05°C. Like System 3, the first air-liquid heat exchanger is assumed to be 3 m distant from the vapor-compression core, while the second air-liquid heat exchanger is assumed to be 10 m distant. The total liquid flow rate is 4.5 gpm (2.84×10^{-4} m^3/s), with the flow being split evenly between each air-to-liquid heat exchanger. As in System 3, an additional flow control device is present in the near air-to-liquid heat exchanger branch to ensure that the pressure drops between the two branches are the same to allow the same liquid flow rate in each branch.

A summary of the system results is shown in Table 22, and a pressure versus enthalpy diagram for the refrigerant in System 4 is shown in Figure 36. The actual conditioned-space air delivery temperature for both air-liquid heat exchangers is 15.05°C. The cooling duties of the heat exchangers are 3.0 kW and 3.0 kW, respectively, for a total system cooling duty of 6.0 kW. The liquid-loop pumping power is 60.5 W, and the power consumed by each blower is 3.23 W. The compressor consumes 1.92 kW, and the condenser-side fan consumes 10.7 W. These power inputs and cooling outputs result in a coefficient of performance of 3.0. A summary of the heat exchanger designs required to achieve the reported results is shown in Table 23. Detailed design information for the liquid-coupled evaporator is given in Table 24, while design details for the air-coupled heat exchangers and the air-coupled condenser are given in Table 25. A comparison of the heat exchanger face areas is presented in Figure 37. As in System 2, sending the cooling to the distant locations in System 4 does not require an additional refrigerant carrying line, only an additional liquid carrying line due to the use of the liquid-coupled evaporator. The liquid pressure drop from the evaporator to the closer heat exchanger is 0.94 kPa while the pressure drop to the farther heat exchanger is 3.1 kPa. Because the

change in pressure of a single-phase liquid does not affect its temperature, the longer lengths do not appreciably affect cooling capacity for each of the two conditioned-space heat exchangers as long as the lines are well insulated.

Table 22: System 4 Results Summary

$T_{air,actual,HX\ 1}$	15.05°C	$T_{air,actual,HX\ 2}$	15.05°C	$T_{air,out,cond}$	46.2°C
$CAT_{a\text{-}l,\ evap,actual\ 1}$	3.05°C	$CAT_{a\text{-}l,\ evap,actual\ 2}$	2.86°C	$CAT_{l\text{-}r,\ evap,actual}$	2.4°C
$CAT_{r\text{-}a,\ cond,actual}$	3.83°C	$\Delta T_{subcool,actual}$	3.01°C	$\Delta T_{superheat,actual}$	5.03°C
COP	3.0	$Q_{HX,evap\text{-}side\ 1}$	3.0 kW	$Q_{HX,evap\text{-}side\ 2}$	3.0 kW
Q_{evap}	6.04 kW	Q_{cond}	8.44 kW	$W_{blower,evap\text{-}side\ 1}$	3.23 W
$W_{fan,evap\text{-}side\ 2}$	3.23 W	$W_{pump,\ evap\text{-}side}$	60.5 W	$W_{compressor}$	1.92 kW
$W_{fan,cond\text{-}side}$	10.7 W	$P_{cond,in}$	1333 kPa	$P_{evap,in}$	360 kPa
$P_{comp,in}$	348 kPa	*Pressure ratio*	3.83		

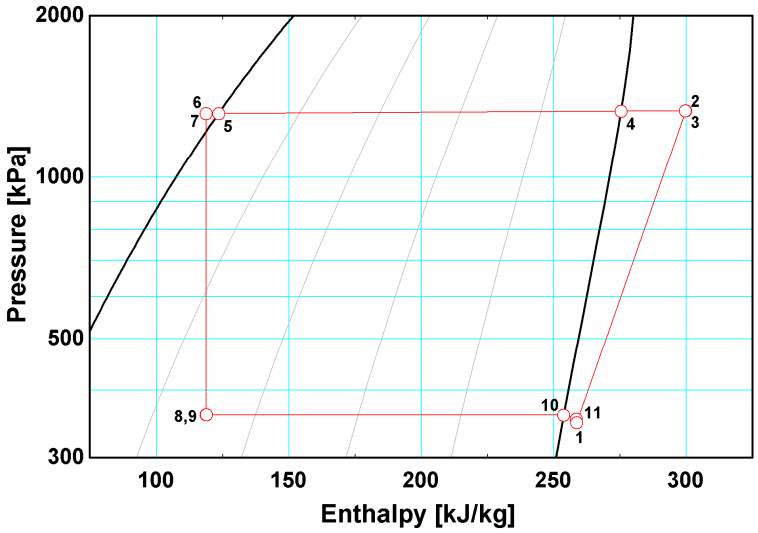

Figure 36: p-h Diagram for System 4, with an Air-Coupled Condenser and a Liquid-Coupled Evaporator, and 2 Air-Liquid Heat Exchangers

Table 23: System 4 Heat Exchanger Design Summary

	h_{total}	L_{total}	$A_{c,total}$	m_{HX}	UA_{total}
ACC	0.535 m	0.456 m	0.244 m^2	2.12 kg	1050 W/K
LCE	0.041 m	0.401 m	-	1.04 kg	1500 W/K
Air-Liq. HX, Evap.-side 1	0.302 m	0.315 m	0.096 m^2	0.71 kg	210 W/K
Air-Liq. HX, Evap.-side 2	0.302 m	0.326 m	0.098 m^2	0.74 kg	215 W/K
	$\Delta P_{refg.}$	ΔP_{air}	$\Delta P_{liq.}$	V_{refg}	Charge, refg.
ACC	14.2 kPa	13 Pa	-	2.5 x 10^{-4} m^3	0.061 kg
LCE	6.4 kPa	-	55.6 kPa	2.2 x 10^{-4} m^3	0.021 kg
Air-Liq. HX, Evap.-side 1	-	0.5 Pa	40.5 kPa	-	-
Air-Liq. HX, Evap.-side 2	-	0.5 Pa	42 kPa	-	-
$\Delta P_{11\text{-}1}$	5.7 kPa	Refg. Charge, Lines	0.029 kg	$\dot{m}_{refg}$	0.0466 kg/s

Table 24: System 4 Liquid-Coupled Evaporator Design Details

	$t_{liq,h,o}$	$t_{liq,w,o}$	$t_{liq,t}$	$N_{p,liq}$	$w_{p,liq}$	$N_{t,liquid}$
LCE	1 mm	50.8 mm	0.15 mm	56	0.7 mm	21
	$t_{refg,h,o}$	$t_{refg,w,o}$	$t_{refg,t}$	$N_{p,refg}$	$w_{p,refg}$	$N_{t,refg}$
LCE	1mm	50.8 mm	0.15 mm	56	0.7	20

As in System 2, the required refrigerant temperature in the evaporator is lower for the liquid-coupled system than for the strictly air-coupled system. This is because of the necessity of a temperature difference to drive heat transfer. To obtain a liquid-refrigerant counter-flow closest approach temperature of 2°C, the evaporator inlet temperature and pressure for System 4 are 5.85°C and 360 kPa, respectively. Accounting for the refrigerant pressure loss across the evaporator and the evaporator discharge line, the

Table 25: System 4 Air-Coupled Heat Exchanger Design Details

	$t_{refg,h,o}$	$t_{refg,w,o}$	$t_{refg,t}$	$N_{p,refg}$	$w_{p,refg}$
ACC	1 mm	25.4 mm	0.15 mm	28	0.7 mm
Air-Liq. HX 1 & 2	1 mm	25.4 mm	0.15 mm	28	0.7 mm
	$N_{t,pass\ 1}$	$N_{t,pass\ 2}$	c_h	c_w	f_p
ACC	20	20	12.7 mm	25.4 mm	1.27 mm
ACE 1 & 2	23	-	12.7 mm	25.4 mm	1.59 mm
	f_t	θ	l_w	l_i	
ACC	0.127 mm	30°	1.14 mm	22.86 mm	
ACE 1 & 2	0.127 mm	30°	1 mm	22.86 mm	

compressor inlet pressure for System 4 is 348 kPa. This is lower than the compressor inlet pressure for System 3 (392 kPa). System 4 has a condenser inlet pressure of 1333 kPa, yielding a pressure ratio of 3.83, while System 3 has a slightly lower condenser inlet

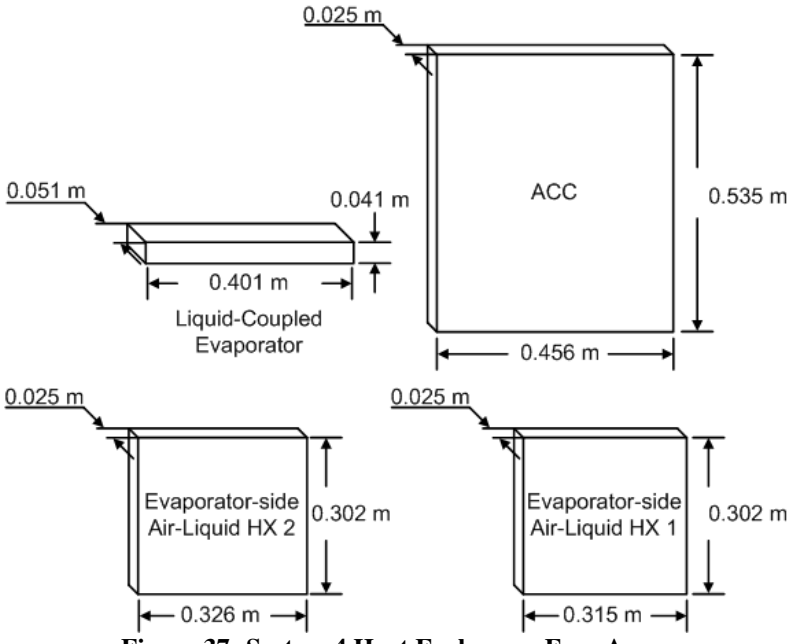

Figure 37: System 4 Heat Exchanger Face Areas

pressure of 1313 kPa, yielding a pressure ratio of 3.35. Since the refrigerant mass flow rates are similar between the two systems (0.04402 kg/s for System 3 and 0.0466 kg/s for System 4), the compressor power is higher for System 4 (1.92 kW) than for System 3 (1.65), which with the addition of liquid-pumping power, leads to a lower COP for System 4 (3.0) than for System 3 (3.35).

4.2. System Comparison

All of the vapor-compression based systems described above are designed for a total heat load of approximately 6 kW. As previously mentioned, total volumetric flow rates of air are the same for each system: 300 ft^3/min (0.142 m^3/s) total for each conditioned-space-side and 1800 ft^3/min (0.549 m^3/s) for each ambient-side heat exchanger. In the systems where there are two conditioned-space-side heat exchangers, each heat exchanger processes half the air flow rate. Refrigerant mass flow rate for each system is determined independently to ensure that the design matches desired closest approach temperatures as closely as possible. Additionally, the compressor (0.7), pump (0.7), and fan/blower (0.5) efficiencies were assumed to be the same for all systems to enable comparison based primarily on the key differentiating features, such as the fluid coupling scheme.

The systems are compared based on three essential characteristics: required power, heat exchanger areas and masses, and the required refrigerant charge.

- Figure 38 shows a p-h diagram with the state points for all four basic systems overlaid.

- Table 26 presents the refrigerant pressure at the condenser inlet, evaporator inlet, and compressor inlet for each system, as well as the pressure ratio and coefficient of performance.
- Figure 39 shows a bar graph with the power consumed by each component within each system as well as the total power consumption for each system.
- Figure 40 shows a bar graph with the total effective heat transfer surface areas required to achieve the reported performance. Figure 41 is a companion to Figure 40; it shows representative heat transfer coefficients for the different fluids in the various components.
- Figure 42 shows the mass of each heat exchanger within each system, as well as the total mass of each system.
- Figure 43 shows the refrigerant charge of each refrigerant-containing component within each system as well as the total refrigerant charge for each system.

Figure 38 clearly shows the thermodynamic differences between the four systems. The systems with liquid-coupled evaporators (LCEs), Systems 2 and 4, require much lower evaporator pressures, 361 kPa and 360 kPa, respectively. The air-coupled evaporators (ACEs) require more moderate evaporator inlet pressures: 430 kPa for System 1 and 430 kPa for System 3. As has been mentioned before, these inlet pressures for liquid-coupled evaporators are so much lower because the presence of the intermediate liquid between the air and the refrigerant necessitates a second heat transfer process, which requires a second temperature difference between the coupling fluid and the refrigerant. With a specified goal for conditioned-space air delivery temperature, the

only way to create this temperature difference is to decrease the evaporator refrigerant saturation temperature by lowering the evaporator refrigerant pressure. A second method of regulating this temperature difference, though perhaps less effective overall, is to change the flow rate of the coupling fluid. Though it is not directly considered in this investigation, varying the flow rate of the coupling liquid alters the change in temperature experienced by the liquid. For the same cooling duty and all other factors being equal, an increase in liquid flow rate would decrease the change in temperature.

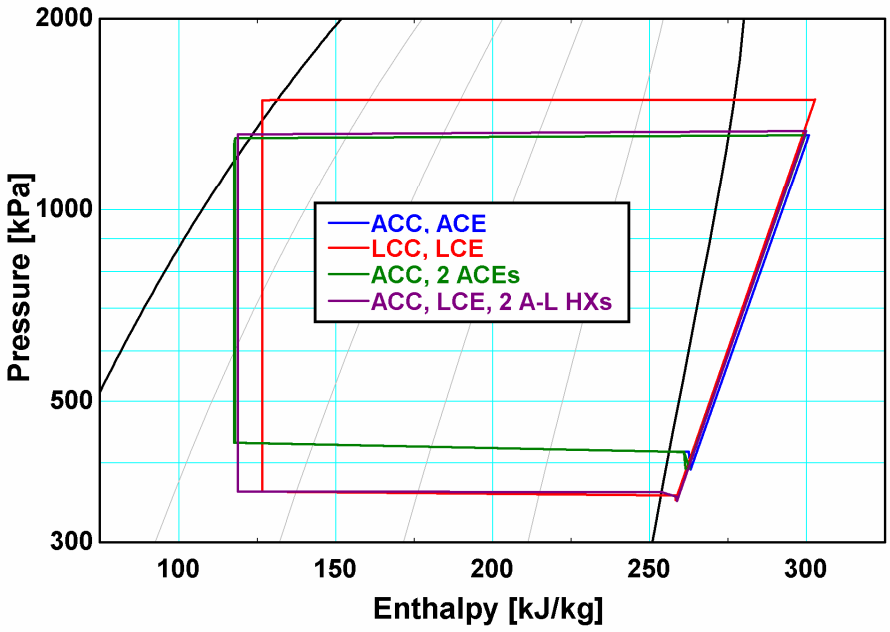

Figure 38: p-h Diagram for all Systems

Table 26: Comparison of Pressures for all Systems

	$P_{cond.,in}$	$P_{evap.,in}$	$P_{comp.,\ in}$	r_p	*COP*
ACC, ACE	1313	430	391	3.35	3.74
LCC, LCE	1492	361	350	4.27	2.81
ACC, 2 ACEs	1313	430	392	3.35	3.79
ACC, LCE, 2 Air-Liq. HXs	1333	360	348	3.83	3.0

Figure 38 also clearly indicates the differences in condenser-inlet refrigerant pressure between the systems. Systems 1 and 3, each with air-coupled condensers and air-coupled evaporators, require the lowest condenser inlet pressure of 1313 kPa. System 4, with evaporator-side liquid coupling and condenser-side air coupling, requires a slightly increased condenser inlet pressure of 1333 kPa. System 2, with liquid coupling on both the evaporator and condenser side, required the highest condenser inlet pressure of 1492 kPa. All of the systems have condenser-side air outlet temperature of approximately 46°C, and the designated closest approach temperatures would require that the fluid directly rejecting heat to the air have a temperature of approximately 49-50°C. This accounts for the similar condenser inlet pressures between systems 1, 3, and 4. The inlet pressure is so much different for System 2 because of the higher refrigerant temperature (53°C) required to reject heat to the condenser-side coupling liquid. The differences in compressor inlet pressures and condenser inlet pressures leads to differences in refrigerant pressure ratio, which accounts for differing compressor power given the similar refrigerant mass flow rates. System 1 has the lowest pressure ratio of 3.35 with a compressor power of 1.64 kW. System 2 has the highest pressure ratio of

4.27 and the highest compressor power of 2.1 kW. The pressure ratio and compressor power of System 3 are very similar to those of System 1 at 3.35 and 1.65 kW. System 4 has an intermediate pressure ratio and compressor power of 3.83 and 1.92 kW.

Figure 39 shows what may be an obvious result: more complex systems require more power. System 1 requires the least power. It is clear that System 2 requires additional compressor power as well as the new pumping power for the coupling liquid loops. The total System 2 power consumption is 32% larger than for System 1: 2.19 kW compared with 1.66 kW. Considering the distributed heat load systems, it can be seen that System 3 requires less power at 1.67 kW than System 4 at 2.0 kW, a difference of 20%. Lastly, it should be noted that the power consumed by the evaporator-side blowers and condenser-side fans is similar in each of the systems since the condenser-side air flow rates and pressure drops are similar among all the systems as are the total flow rates and pressure drops for the evaporator-side heat exchangers.

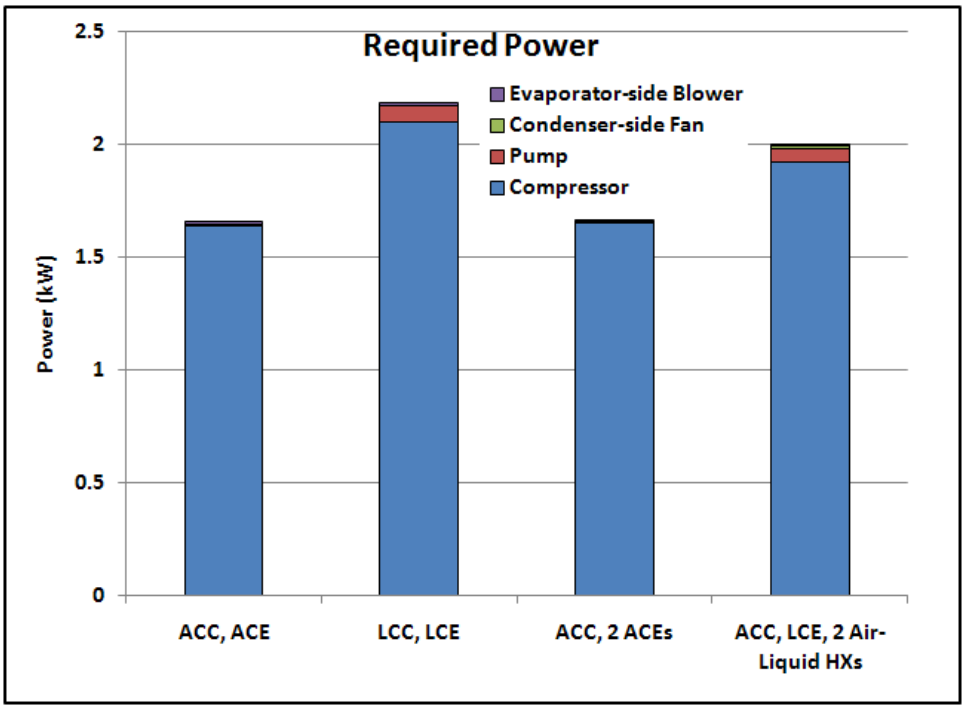

Figure 39: Required Power Comparison

Figure 40 illustrates another result that is as expected: increasing system complexity pertaining to fluid routing increases the number of components and required heat transfer areas. The surface areas that are considered in Figure 40 represent the combination of the direct heat transfer surface area and the indirect heat transfer surface area through the use of fin efficiencies; therefore, what is compared in Figure 40 is effective heat transfer surface area. Between the two systems with one conditioned-space-side air-coupled heat exchanger, the required air-side surface areas are similar for both the evaporator side and the condenser side. The evaporator and condenser air-side areas for System 1 are 6.7 m^2 and 8.1 m^2, respectively. The air-side surface areas for the evaporator- and condenser-side air-liquid heat exchangers for System 2 are 6.1 m^2 and 8.9 m^2, respectively. This similarity is because the air-side heat transfer coefficients, which lead to the dominant resistance, are quite similar between the two systems. For the evaporator side, the average air heat transfer coefficients are 77 W/m^2-K and 86 W/m^2-K

for Systems 1 and 2, respectively. For the condenser side, the average air heat transfer coefficients are 191 W/m^2-K and 170 W/m^2-K, for Systems 1 and 2, respectively. It can be seen that the condenser refrigerant-side surface area is smaller for the liquid-coupled condenser in System 2 (0.85 m^2) than the air-coupled condenser in System 1 (1.4 m^2). This trend is also seen between the System 2 liquid-coupled evaporator refrigerant-side area (1.2 m^2) and the System 1 air-coupled evaporator refrigerant-side area (1.8 m^2).

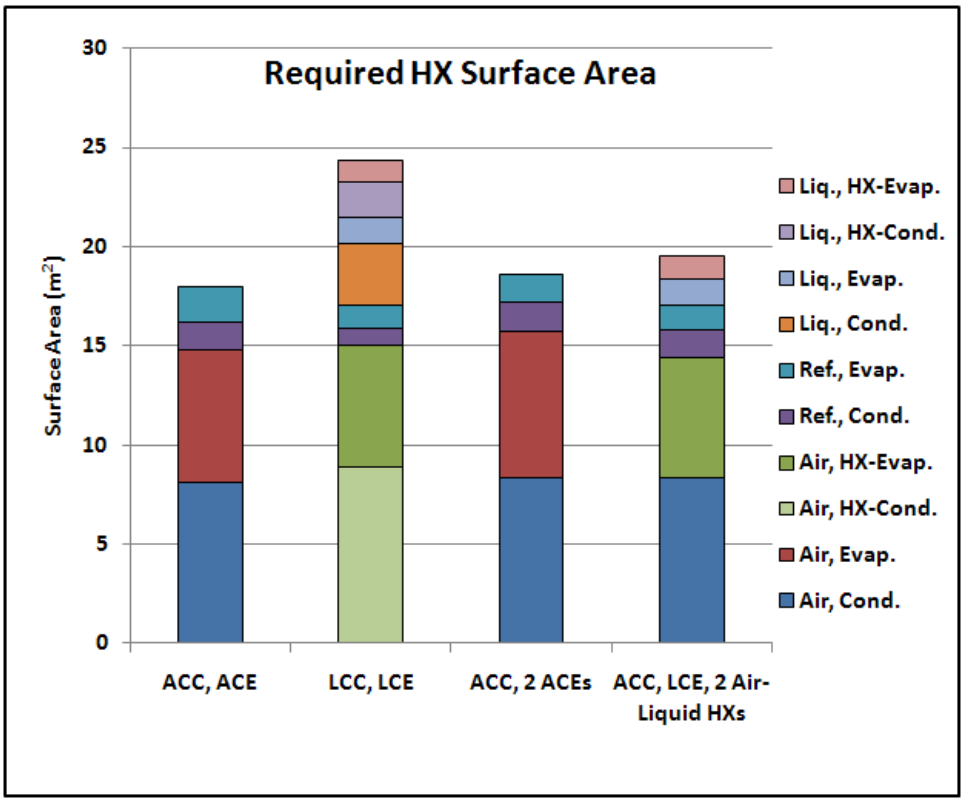

Figure 40: Required Heat Exchanger Surface Comparison

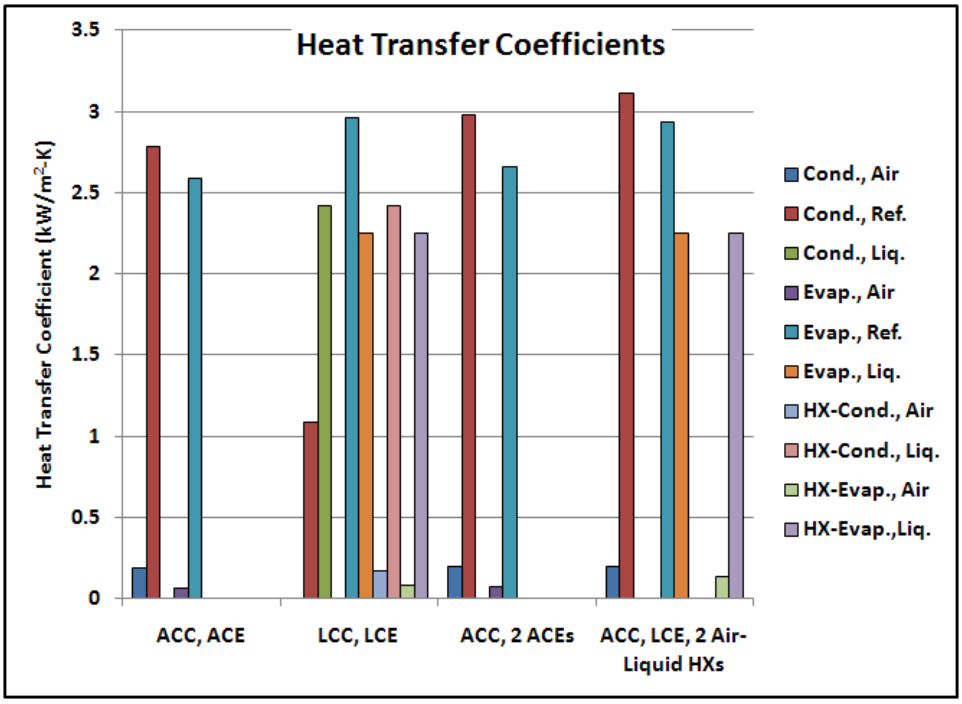

Figure 41: Heat Transfer Coefficient Comparison

Though the total surface areas required by the distributed cooling systems are slightly larger than that for the other systems, the observed trends in refrigerant areas are the same: the required evaporator refrigerant–side area (1.5 m^2) is larger than that required of the System 4 liquid-coupled evaporator (1.2 m^2). The total surface area required by System 3 (18.6 m^2) is 3.5% larger than the total for System 1 (17.9 m^2). The System 4 total area (19.5 m^2) is 20% less than the System 2 total (24.4 m^2), since one entire heat exchanger is eliminated by having an air-coupled condenser instead of a liquid-coupled condenser. The increase in surface area required for liquid coupling (4.9%) is less significant for the distributed cooling configuration than for the standard configuration (36%).

The larger surface areas required by the more complex systems is also reflected in the larger total system masses, as seen in Figure 42. Considering the standard configuration systems, the total mass of System 1 (3.8 kg) is 66% of the total mass (5.79 kg) of System 2. The mass of the liquid-coupled condenser in System 2 (1.05 kg) is 51% of the air-coupled condenser mass in System 1 (2.06 kg). The mass of the liquid-coupled evaporator in System 2 (1.02 kg) is 59% of the air-coupled evaporator mass in System 1 (1.74 kg). The addition of the condenser-side and evaporator-side air-liquid heat exchangers in System 2, 2.26 kg and 1.46 kg, respectively, increases the total mass of heat exchangers in System 2.

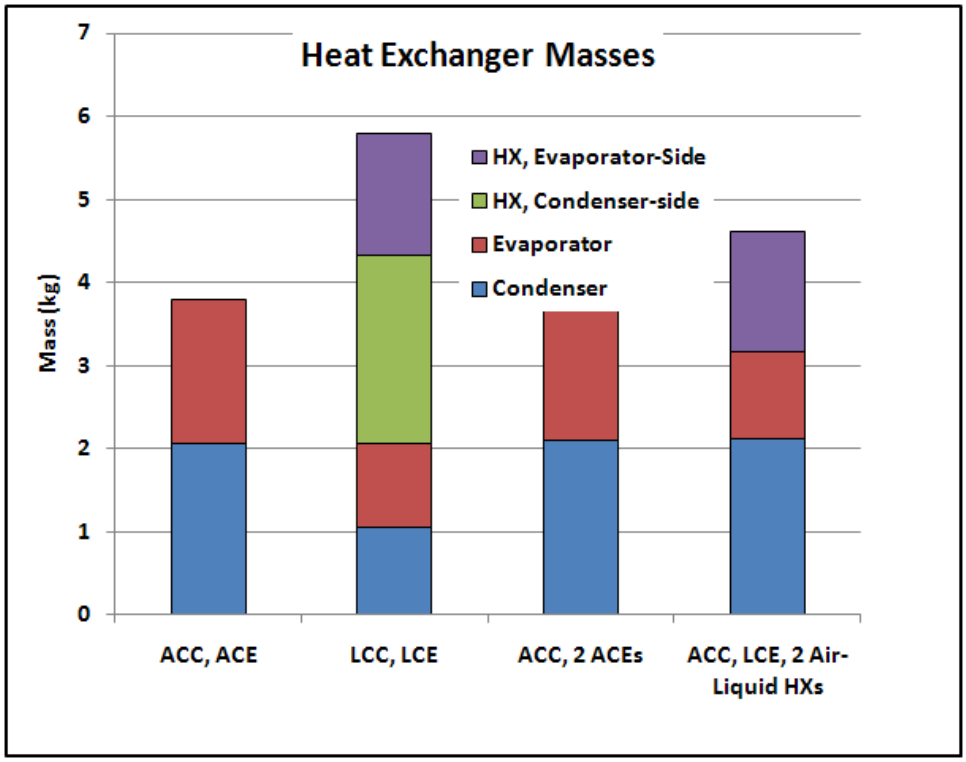

Figure 42: Heat Exchanger and System Mass Comparison

The mass of the heat exchangers in the distributed cooling configuration systems is slightly larger than for the standard configuration systems. The masses of the air-coupled condensers in Systems 3 and 4 are 2.11 kg and 2.12 kg, respectively. The

masses of the evaporators in Systems 3 and 4 are 1.83 kg and 1.04 kg, respectively The total mass of the heat exchangers in System 3 (3.94 kg) is only slightly larger than the total mass of System 1 heat exchangers (3.8 kg). The total heat exchanger mass of System 4 (4.61 kg) is larger than the total mass of System 3 but less than the total mass of System 2.

Refrigerant charge in each system, depicted in Figure 43, is the measure of the mass of refrigerant contained in each system. The charge in the liquid-coupled condenser of System 2 (0.051 kg) is 80% of the charge the air-coupled condenser of System 1(0.064 kg). This stands to reason, as the required LCC surface area is also less than the required ACC surface area. The liquid-coupled evaporator of System 2 has a lower refrigerant charge (0.0194 kg) than the air-coupled evaporator in System 1 (0.0284 kg). The longer refrigerant containing lines found in System 1 lead to a much higher line charge for System 1 (0.0122 kg) than for System 2 (0.028 kg). Among the standard configuration systems, System 2 has the smallest total charge at 0.098 kg as compared with 0.215 kg for System 1. The condenser refrigerant charges for the distributed heat load systems are all comparable: 0.06 kg for System 3 and 0.061 kg for System 4. The charge in the liquid-coupled evaporator in System 4 (0.021 kg) is also slightly less than the air-coupled evaporators in System 3 (0.022 kg). The refrigerant charge required in System 3 to reach the distant evaporator (assuming actual line lengths of 10 m) is larger than any other contribution at 1.26 kg. The line charge in System 4 is minuscule by comparison at 0.029 kg. The total charge in System 3 (1.34 kg) is 1200% of the total in System 4 (0.111 kg).

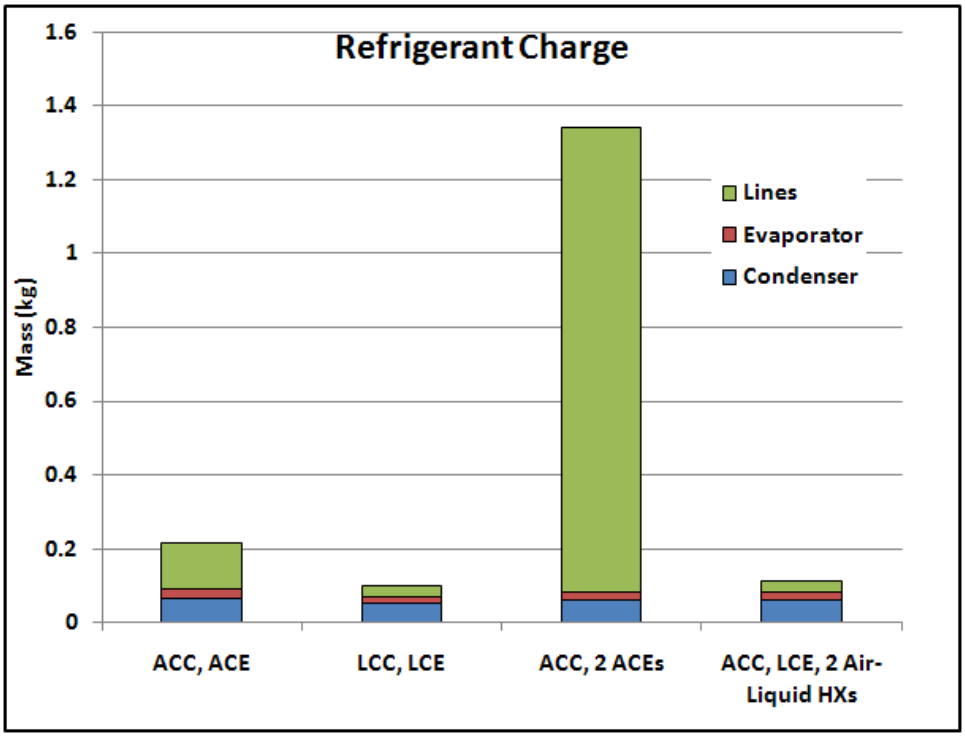

Figure 43: Heat Exchanger and System Refrigerant Charge Comparison

CHAPTER 5

CONCLUSIONS AND RECOMMENDATIONS

5.1. Conclusions

Hydronically coupled vapor-compression systems offer capabilities that are not normally present in standard air-coupled systems; however, these come at a price. A liquid-coupled system allows for more flexible placement of the air-coupled components since extended refrigerant lines and associated pressure drops are not a factor. However, this capability requires a greater temperature difference between the heat source and heat sink to accommodate heat transfer to and from the coupling liquid. On the evaporator side, this leads to lower evaporator inlet pressures, and on the condenser side, this leads to higher condenser inlet pressures. Both of these factors contribute to a larger refrigerant pressure ratio across the compressor, necessitating more compressor power.

The price of flexible component placement also includes additional heat exchangers and their associated masses. The total mass of a liquid-coupled system will be larger than a comparable strictly air-coupled system. Additionally, having both sides of a core system liquid coupled will add another heat exchanger and its mass when compared with having only one side liquid coupled. Liquid coupled systems do show conclusive improvement over air-coupled systems when considering total system refrigerant charge. By eliminating longer refrigerant lines, liquid-coupled systems can offer significantly diminished total refrigerant charges. Concerning the charges in individual components, the heat exchangers in this investigation were designed with the goal of minimizing the mass of a given component. This may have resulted in designs

that were sub-optimal when considering total component refrigerant charge. If minimizing refrigerant charge were the primary goal of a system, this likely could be accomplished even on the component level with liquid-coupled systems, as evidenced by the liquid-coupled condensers presented earlier.

Lastly, it should be noted that the negative differences between air-coupled systems and liquid-coupled systems, including total required power, total system surface area and mass appear to diminish in relative magnitude as the complexity of the comparable air-coupled system increases. Only two heat loads were considered in this investigation, but when even more are present, it appears that a liquid-coupled system would require less fundamental alteration to accommodate new requirements than a strictly air-coupled solution. Hydronically coupled vapor-compression systems do offer advantages over air-coupled solutions, though these come at a price. This price will vary with every situation; therefore, the applicability of a liquid-coupled solution depends upon the importance design goals including refrigerant charge, refrigerant containment, total power, number of heat exchangers, and total system mass.

5.2. Recommendations

While this study has provided insight into the benefits and tradeoffs of using liquid-coupling for distributed cooling, specifically, additional work can be performed to further investigate the available options.

- This study considered at most two heat loads; however, there is the possibility of more heat loads than this, especially if a distributed cooling system were to be used to cool various electronic components. Additional modeling of systems with

more and different types of heat loads would help better determine the applicability.

- In addition to the number of heat loads, the magnitude of the heat fluxes and total heat loads considered in this study were not very diverse. If electronics cooling were the goal of a hydronically coupled, distributed cooling system, higher heat fluxes would likely be encountered. Additional system modeling would address the applicability of hydronically coupled, distributed cooling systems for such use.
- The system modeling in this study only considered the highest system loading condition in the hottest environment. Additional system modeling would determine the effect of various ambient conditions and desired conditioned-space air delivery temperatures on the performance of a given system design. Similarly, dynamic system modeling would indicate the possible benefits and tradeoffs of a hydronically coupled, distributed cooling system with changing ambient conditions, such as ambient temperature, desired load, or vehicle velocity.
- The compressor model used in this study was very simplistic to allow for focus on the effects of system configuration. Integration of a more detailed and realistic compressor model would allow for accurate compressor sizing and selection. A more realistic compressor model would also contribute to a better part load/dynamic system model. This would also allow for the investigation of the effect of various types of compressors.
- Lastly, experimental validation of a hydronically coupled, distributed cooling system should also be performed.

REFERENCES

Achaichia, A. and Cowell, T. A. (1988), "Heat transfer and pressure drop characteristics of flat tube and louvered plate fin surfaces," *Experimental Thermal and Fluid Science*, **1** (2): 147-157.

Agarwal, A., Bandhauer, T. M. and Garimella, S. (2010), "Measurement and modeling of condensation heat transfer in non-circular microchannels," *International Journal of Refrigeration*.

Agarwal, A. and Garimella, S. (2009), "Modeling of pressure drop during condensation in circular and noncircular microchannels," *Journal of Fluids Engineering*, **131** (1): 011302 (8 pp.).

Bandhauer, T. M., Agarwal, A. and Garimella, S. (2006), "Measurement and modeling of condensation heat transfer coefficients in circular microchannels," *Journal of Heat Transfer*, **128** (10): 1050-1059.

Birch, T. (1995). Automotive Heating and Air Conditioning. Englewood Cliffs, New Jersey, Prentice Hall.

Butterworth, D. (1975), "A comparison of some void-fraction relationships for co-current gas-liquid flow," *International Journal of Multiphase Flow*, **1** (6): 845-850.

Carey, V. P. (2008). Liquid-Vapor Phase-Change Phenomena: An Introduction to the Thermophysics of Vaporization and Condensation Processes in Heat Transfer Equipment. New York, Taylor & Francis Group.

Carlyle, C. C. (2010). Carlyle Solutions. Syracuse, NY, Carlyle Compressor Company.

Carlyle Compressor Company (2009). 06D Tabular Data. http://www.carlylecompressor.com/Files/Carlyle_Compressor/Local/US-en/pdf_files/06D.pdf.

Castaing-Lasvignottes, J. and Gibout, S. (2010), "Dynamic simulation of reciprocating refrigeration compressors and experimental validation," *International Journal of Refrigeration*, **33** (2): 381-389.

Chang, Y.-J., Chang, W.-J., Li, M.-C. and Wang, C.-C. (2006), "An amendment of the generalized friction correlation for louver fin geometry," *International Journal of Heat and Mass Transfer*, **49** (21-22): 4250-4253.

Chang, Y.-J., Hsu, K.-C., Lin, Y.-T. and Wang, C.-C. (2000), "A generalized friction correlation for louver fin geometry," *International Journal of Heat and Mass Transfer*, **43** (12): 2237-2243.

Chang, Y.-J. and Wang, C.-C. (1997), "A generalized heat transfer correlation for louver fin geometry," *International Journal of Heat and Mass Transfer*, **40** (3): 533-544.

Chen, J. C. (1966), "Correlation for Boiling Heat Transfer to Saturated Fluids in Convective Flow," *Industrial & Engineering Chemistry Process Design and Development*, **5** (3): 322-329.

Chen, Y., Peterson, G. P. and Li, J. (2006). Influence of hydraulic diameter on flow condensation in silicon microchannels. 13th International Heat Transfer Conference. Sydney, Australia**:** pp. CSN-01.

Chisholm, D. and Laird, A. D. K. (1957), "Two-phase flow in rough tubes, New York, NY, United States, American Society of Mechanical Engineers (ASME), p. 9.

Chisholm, D. and Laird, A. D. K. (1963), "Two-phase flow in rough tubes, New York, NY, United States, American Society of Mechanical Engineers (ASME), p. 9.

Churchill, S. W. (1977a), "Comprehensive Correlating Equations for Heat, Mass and Momentum Transfer in Fully Developed Flow in Smooth Tubes," *Industrial & Engineering Chemistry, Fundamentals*, **16** (1): 109-116.

Churchill, S. W. (1977b), "Friction-Factor Equation Spans All Fluid-Flow Regimes," *Chemical Engineering (New York)*, **84** (24): 91-92.

Churchill, S. W. and Chu, H. H. S. (1975), "Correlating equations for laminar and turbulent free convection from a horizontal cylinder," *International Journal of Heat and Mass Transfer*, **18** (9): 1049-1053.

Cullimore, B. A. and Hendricks, T. J. (2001), "Design and Transient Simulation of Vechile Air Conditioning Systems," *Vehicle Thermal Management Systems Conference*, Nashville, Tennessee, Society of Automotive Engineers

Davenport, C. J. (1983), "Correlations for Heat Transfer and Flow Friction Characteristics of Louvered Fin, Seattle, WA, USA, AIChE, pp. 19-27.

Duprez, M.-E., Dumont, E. and Frere, M. (2007), "Modeling of reciprocating and scroll compressors," *International Journal of Refrigeration*, **30** (5): 873-886.

Eilemann, A. and Kampf, H. (2001), "Comfort-Management," *Vehicle Thermal Management Systems Conference*, Nashville, Tennessee, Society of Automotive Engineers

El Bakkali, A., Oliver, G., Rhote-Vaney, R., Meillier, R. and Roman, C. (2003). Design of component libraries for the transient simulation of an automotive refrigerant loop. Vehicle Thermal Management Systems Conference. Brighton, United Kingdom, Professional Engineering Publishing, Limited.

Forster, H. K. and Zuber, N. (1955), "Dynamics of vapor bubbles and boiling heat transfer," *Chemical Engineering Progress*, **1** (4): 531-535.

Garimella, S. and Wicht, A. (1995), "Air-cooled condensation of ammonia in flat-tube, multi-louver fin heat exchangers, San Francisco, CA, USA, ASME, pp. 47-58.

Gnielinski, V. (1976), "New equations for heat and mass transfer in turbulent pipe and channel flow," *International Chemical Engineer*, **16**: 359-368.

Goodman, C. L. (2008). "Modeling, Validation, and Design of Integrated Carbon Dioxide Heat Pumps and Water Heaters," Mechanical Engineering, Georgia Institute of Technology, Atlanta, Georgia.

Grosse, G., Robidou, H. and Chevallier, C. (2006). Heat Transfer in Minichannel Tubes for Automotive Evaporator. SAE 2006 World Congress. Detroit, Michigan, Society of Automotive Engineers, Inc.

Hansen, E. G. (1985). Hydronic System Design and Operation: A Guide to Heating and Cooling with Water. New York, McGraw-Hill Book Company.

Hendricks, T. J. (2003). Multi-variable optimization of electrically-driven vehicle air-conditioning systems using transient performance analysis. Vehicle Thermal Management Systems Conference. Brighton, United Kingdom, Processional Engineering Publishing, Limited.

Hyland, R. W. and Wexler, A. (1983), "Formulations for the Thermodynamic Properties of the saturated Phases of H2O from 173.15K to 473.15K," *ASHRAE Transactions*, **89** (2A): 500-519.

Incropera, F. P., DeWitt, D. P., Bergman, T. L. and Lavine, A. S. (2007). Fundamental of Heat and Mass Transfer. Hoboken, New Jersey, John Wiley & Sons, Inc.

Janna, W. S. (1998). Design of Fluid Thermal Systems. Boston, MA, PWS Publishing Company.

Jiang, Y. (2001). "Comparison of low refrigerant charge, air-coupled and hydronically coupled microchannel heat pumps with conventional systems," Mechanical Engineering, Iowa State University, Ames, Iowa.

Kakac, S., Shah, R. K. and Anng, W., Eds. (1987). Handbook of Single-Phase Convective Heat Transfer. New York, John Wiley & Sons.

Kampf, H. and Schmadl, D. (2001). Parking Cooling Systems for Truck Cabine. Vehicle Thermal Management Systems Conference. Nashville, Tennessee, Society of Automotive Engineers.

Kandlikar, S. G. (1990), "A General Correlation for Saturated Two-Phase Flow Boiling Heat Transfer Inside Horizontal and Vertical Tubes," *Journal of Heat Transfer*, **112** (1): 219-228.

Kandlikar, S. G. (1991), "Development of a Flow Boiling Map for Subcooled and Saturated Flow Boiling of Different Fluids Inside Circular Tubes," *Journal of Heat Transfer*, **113** (1): 190-200.

Kandlikar, S. G. and Balasubramanian, P. (2004), "An Extension of the Flow Boiling Correlation to Transition, Laminar, and Deep Laminar Flows and Microchannels, Taylor and Francis Ltd., pp. 86-93.

Kandlikar, S. G., Garimella, S., Li, D., Colin, S. and King, M. R. (2006). Heat Transfer and Fluid Flow in Minichannels and Microchannels. Kidlington, Oxford, United Kingdom, Elsevier.

Kandlikar, S. G. and Grande, W. J. (2003), "Evolution of microchannel flow passages-thermohydraulic performance and fabrication technology," *Heat Transfer Engineering*, **24** (1): 3-17.

Kays, W., Crawford, M. and Weigand, B. (2005). Convective Heat and Mass Transfer. New York, McGraw-Hill.

Kim, M.-H. and Bullard, C. W. (2002), "Thermal performance analysis of small hermetic refrigeration and air-conditioning compressors," *JSME International Journal, Series B: Fluids and Thermal Engineering*, **45** (4): 857-864.

Klein, S. A. (2009). Engineering Equation Solver, F-Chart Software.

Laboe, K. J. and Gondusky, J. M. (1995), "Variable Orifice Tube Performance in Automotive Refrigerant Systems," *Vehicle Thermal Management Systems Conference*, London, United Kingdom, Mechanical Engineering Publications Limited

Lee, J. and Mudawar, I. (2005), "Two-phase flow in high-heat-flux micro-channel heat sink for refrigeration cooling applications: Part II--heat transfer characteristics," *International Journal of Heat and Mass Transfer*, **48** (5): 941-955.

Lockhart, R. W. and Martinelli, R. C. (1949), "Proposed correlation of data for isothermal two-phase, two-component flow in pipes," *Chemical Engineering Progress*, **45** (1): 39-45.

Lou, Z. D. (2005), "A Dynamic Model of Automotive Air Conditioning Systems," *Thermal Management Systems, Modeling, and Components*, Society of Automotive Engineers, pp. 129-135.

Mann, M. and Nies, J. (2003). From a single component to a complete system- an integrated simulation and validation concept. Vehicle Thermal Management Systems Conference. Brighton, United Kingdom, Professional Engineering Publishing, Limited.

Melinder, A., Ed. (1997). Thermophysical Properties of Liquid Secondary Refrigerants. International Institute of Refrigeration. Paris.

Munson, B. R., Young, D. F. and Okiishi, T. H. (2006). Fundamentals of Fluid Mechanics. Hoboken, New Jersey, John Wiley & Sons, Inc.

Navarro, E., Granryd, E., Urchueguia, J. F. and Corberan, J. M. (2007), "A phenomenological model for analyzing reciprocating compressors," *International Journal of Refrigeration*, **30** (7): 1254-1265.

Ohtake, H., Ohtaki, H. and Koizumi, Y. (2006), "Frictional pressure drop and two-phase flow pattern of gas-liquid flow in circular and rectangular minichannels," *Fourth International Conference on Nanochannels, Microchannels, and Minichannels*, Limerick, Ireland

Perez-Segarra, C. D., Rigola, J., Soria, M. and Oliva, A. (2005), "Detailed thermodynamic characterization of hermetic reciprocating compressors," *International Journal of Refrigeration*, **28** (4): 579-593.

Petukhov, B. S. and Popov, V. N. (1963), "Theoretical calculation of heat exchange and frictional resistance in turbulent flow in tubes of an incompressible fluid with variable physical properties," *Teplofizika Vysokikh Temperatur*, **1** (1).

Preissner, M., Radermacher, R., Zhang, C. and Dickson, T. (2001). R134A Suction Line Heat Exchanger in Different Configurations of Automotive Air-Conditioning Systems. Vehicle Thermal Management Systems Conference. Nashvillee, Tennessee, Society of Automotive Engineers.

Rahman, S., Ragazzi, F., Sun, R. and Bathla, P. (2003). Modeling of an Automotive Air Conditioning System and Validation with Experimental Data. SAE World Conference, Society of Automotive Engineers. **SP-1733:** pp. 35-40.

Rogstam, J. and Mingrino, F. (2003). A coolant-based automotive heat pump system. Vehicle Thermal Management Systems Conference. Brighton, United Kingdom, Professional Engineering Publishing, Limited.

Schwentker, R. A., Winkler, J. M., Aute, V. C. and Radermacher, R. (2006). A Simulation and Design Tool for Flat Tube, Louvered-Fin Heat Exchangers. SAE World Congress. Detroit, Michigan, Society of Automotive Engineers**:** pp. 01-1451.

Shah, M. M. (1976), "New Correlation for Heat Transfer During Boiling Flow Through Pipes," *ASHRAE Transactions*, **82 pat 2**: 66-86.

Shah, M. M. (1979), "A general correlation for heat transfer during film condensation inside pipes," *International Journal of Heat and Mass Transfer*, **22** (4): 547-556.

Soliman, M., Schuster, J. R. and Berenson, P. J. (1967), "General heat transfer correlation for annular flow condensation, New York, NY, United States, American Society of Mechanical Engineers (ASME), p. 8.

Sunden, B. and Svantesson, J. (1992), "Correlations of j - and f - factors for multilouvered heat transfer surfaces, Birmingham, Engl, Publ by Inst of Chemical Engineers, pp. 805-811.

Thelen, W. A. and Zoz, S. (2003). An approach for modeling an automotive vapour cycle refrigeration system and passenger cabin. Vehicle Thermal Management Systems Conference. Brighton, United Kingdom, Professional Engineering Publishing, Limited.

Tillner-Roth, R. and Baehr, H. D. (1994), "An International Standard Formulation for the Thermodynamic Properties of 1,1,1,2-Tetrafluoroethane (HFC-134a) for Temperatures from 170 K to 455 K and Pressures up to 70 MPa," *Journal of Physical and Chemical Reference Data*, **23** (5): 657-729.

Traviss, D. P., Rohsenow, W. M. and Baron, A. B. (1973), "Forced-Convection Condensation Inside Tubes: A Heat Transfer Equation for Condenser Design," *ASHRAE Transactions*, **79** (Part 1): 157-165.

Wang, H. S. and Rose, J. W. (2005), "A Theory of Film Condensation in Horizontal Noncircular Section Microchannels," *Journal of Heat Transfer*, **127** (10): 1096-1105.

Wang, W.-W. W., Radcliff, T. D. and Christensen, R. N. (2002), "A condensation heat transfer correlation for millimeter-scale tubing with flow regime transition," *Experimental Thermal and Fluid Science*, **26** (5): 473-485.

Wu, H. Y. and Cheng, P. (2005), "Condensation flow patterns in silicon microchannels," *International Journal of Heat and Mass Transfer*, **48** (11): 2186-2197.

Yen, T.-H., Kasagi, N. and Suzuki, Y. (2003), "Forced convective boiling heat transfer in microtubes at low mass and heat fluxes," *International Journal of Multiphase Flow*, **29** (12): 1771-1792.